

CMOS SYSTEMS AND CIRCUITS FOR SUB-DEGREE PER HOUR MEMS GYROSCOPES

A Thesis
Presented to
The Academic Faculty

by

Ajit Sharma

In Partial Fulfillment
of the Requirements for the Degree
Doctor of Philosophy in the
School of Electrical and Computer Engineering

Georgia Institute of Technology
December 2007

CMOS SYSTEMS AND CIRCUITS FOR SUB-DEGREE PER HOUR MEMS GYROSCOPES

Approved by:

Professor Farrokh Ayazi, Advisor
School of Electrical and Computer
Engineering
Georgia Institute of Technology

Professor Paul Hasler
School of Electrical and Computer
Engineering
Georgia Institute of Technology

Professor W. Marshall Leach
School of Electrical and Computer
Engineering
Georgia Institute of Technology

Professor Jennifer Michaels
School of Electrical and Computer
Engineering
Georgia Institute of Technology

Professor Levent Degertekin
School of Mechanical Engineering
Georgia Institute of Technology

Date Approved: 18 October 2007

To,
My Parents,
and Chaitanya.

ACKNOWLEDGEMENTS

Let me start by thanking my PhD advisor Dr.Farrokh Ayazi. His incisive observations and questions kept me constantly questioning my premises and thus honing my knowledge. He has given me advice and allowed me independence in well-balanced proportions - both equally crucial in the course of graduate research. I am also grateful to him for the excellent infrastructure and academic opportunities he has provided over the course of my PhD work.

I would like to thank Dr.Paul Hasler, Dr.W. Marshall Leach, Dr.Jennifer Michaels and Dr.Levent Degertekin for taking an interest in my work and serving on my PhD defense committee.

This work was sponsored by the DARPA HERMIT program under contract # W31P4Q-0-1-R001 and the Georgia Tech - Texas Instruments Analog Fellowship program. IC fabrication support was provided by the MOSIS Educational Partnership.

Many thanks are due to Janet Myrick, Amber Leshner, Margret Boehme and Wanda Wilson for all their administrative help and co-operation.

I would like to thank Dr.Jeanne Pitz and Eric Blackall from the Mixed Signal Automotive Group at Texas Instruments for their support and encouragement during my co-op term there.

I would like to thank the members of the entire IMEMS group, both past and present, for all their help and cooperation. Mohammad Faisal Zaman fabricated the MEMS devices used for this work and has been a reliable team-mate. Dr.Babak Vakili Amini provided invaluable guidance and direction during my initial years at Tech. Special thanks to Dr.Krishnakumar Sundaresan for all his help over the years - friends like him are hard to come by. Thanks also to Milap, Jalpa, Hourii, Tony and

Aditi for lightening the long hours spent in the lab.

Looking back over the years spent in school, I realize the importance of many subtle lessons taught by my parents and the stimulating environment they provided for me. I would also like to acknowledge my wife's family for supporting my every step and for taking such a keen interest in my work.

Finally, I must admit that this work would have been impossible without the understanding and support from my wife - Chaitanya. She has many a time selflessly allowed her graduate research to take a back-seat so as to accommodate mine. I am grateful to her for all her love and support over the years.

TABLE OF CONTENTS

DEDICATION	iii
ACKNOWLEDGEMENTS	iv
LIST OF TABLES	x
LIST OF FIGURES	xi
SUMMARY	xvi
I MICROMACHINED VIBRATING SILICON GYROSCOPES	1
1.1 Applications and Market Demands	1
1.2 Principle of Operation	4
1.3 Performance Specifications	6
1.3.1 Resolution	6
1.3.2 Scale Factor	7
1.3.3 Zero Rate Output and Bias Stability	8
1.3.4 Bandwidth and Dynamic Range	9
1.4 Motivation	10
1.5 Thesis Organization	13
II SYSTEM LEVEL CONSIDERATIONS FOR MEMS GYROSCOPES . .	15
2.1 Mode-Matched Tuning Fork Gyroscope - Device Operation	15
2.2 Electronic System Description	18
2.2.1 Drive Loop	18
2.2.2 Quadrature Nulling and Mode-matching	20
2.2.3 Sense Channel	21
2.3 Gyroscope System Modeling	22
III TRANSIMPEDANCE CAPACITIVE FRONT-ENDS	26
3.1 Challenges in MEMS Interfacing	26
3.2 Overview of analog capacitive-MEMS front ends	29

3.3	Why Transimpedance?	30
3.4	T-TIA's for capacitive detection	35
3.4.1	Design considerations	35
3.4.2	Low-noise CMOS Op-amp	40
3.5	Measured Results of CMOS T-TIA	41
IV	DRIVE AND SENSE ELECTRONICS	48
4.1	Drive Resonant Oscillator	48
4.2	PLL-based drive oscillator	50
4.3	Measurement of drive amplitude	53
4.4	Analog Sense Channel	55
4.4.1	Rotation Response	57
4.5	Summary	58
V	QUADRATURE ERROR AND MODE-MATCHING IN MICROGYRO- SCOPES	60
5.1	Origins and Impact of Quadrature Error	60
5.2	Quadrature Nulling	63
5.3	Electrostatic Frequency Tuning	66
5.4	Importance of Mode-matching	69
5.5	Automatic Mode-Matching - Prior Art	71
5.6	Automatic Mode-Matching - Proposed Concept	74
VI	CMOS AUTOMATIC MODE-MATCHING SYSTEM	78
6.1	Circuits and System design	78
6.2	ZRO Level Detector	78
6.2.1	Design Considerations	78
6.2.2	Measured Performance	80
6.3	Sigma-Delta Modulator	82
6.3.1	Design Considerations	82
6.3.2	Measured Performance	82

6.4	Timing Considerations	84
6.5	V_P -Stepper	86
6.5.1	Design Considerations	86
6.5.2	Measured Performance	88
6.6	Experimental Results	89
6.6.1	Mode-matching in Time and Frequency Domains	89
6.6.2	Mode-matching stability over temperature	91
6.6.3	Mode-matching stability over time	93
6.6.4	Scale factor	94
6.7	Electronic Bandwidth Control	96
6.8	Summary	99
VII	BIAS DRIFT IN MICROMACHINED GYROSCOPES	101
7.1	What is Drift?	101
7.2	The Allan Variance Technique for Drift Characterization	102
7.2.1	Computing the Allan Variance	103
7.2.2	Noise components in a gyroscope	105
7.2.3	Quantization Noise	106
7.2.4	Angle Random Walk	107
7.2.5	Bias Instability	108
7.2.6	Rate Random Walk	108
7.3	Relationships between noise sources, drift and Allan variance	109
7.4	Drift in the $M^2 - TFG$	111
7.4.1	$40\mu m$ thick SOI TFG	112
7.4.2	$60\mu m$ thick SOI TFG	112
7.4.3	Drift vs. Temperature	113
7.4.4	Drift vs. Bandwidth	115
7.5	Guidelines to reduce drift in micromachined gyroscopes	115
7.6	Comparison of drift from inertial grade gyroscopes	118

VIII CONCLUSIONS AND FUTURE WORK	124
8.1 Technical Contributions	124
8.2 Future Work	127
8.2.1 Automatic quadrature trimming	127
8.2.2 Closed-loop operation using force-feedback	128
8.2.3 Flash ADC for Coarse tuning	131
8.2.4 Bandwidth increase by Q-loading	132
8.2.5 A 1.8V $0.01^\circ/hr$ silicon vibratory microgyro	134
APPENDIX A BIAS DRIFT MEASUREMENT	135
APPENDIX B ELECTROMECHANICAL MICROSYSTEM MODELING AND SIMULATION	140
APPENDIX C DISCRETE ELECTRONICS FOR LOW-FREQUENCY GY- ROSCOPES	148
APPENDIX D FILTERING BIAS DRIFT DATA AND EFFECTS ON GYRO DRIFT PERFORMANCE	151
REFERENCES	156

LIST OF TABLES

1.1	Performance requirements for rate-grade and navigation grade gyroscopes.	3
2.1	Mechanical parameters of the sensor used in this work.	18
2.2	Expressions and approximate values for equivalent RLC parameters of the sensor used in this work.	24
3.1	Summary of measured op-amp parameters.	42
4.1	Summary of key Sensor and drive/ sense ASIC parameters	59
6.1	Summary of key Sensor and mode-matching ASIC parameters	100

LIST OF FIGURES

1.1	Demonstration of Coriolis Force.	5
1.2	Types of gyroscopes.	5
1.3	Summary of FOG, HRG and MEMS gyroscopes.	10
1.4	Performance scaling of micromachined gyroscopes.	11
2.1	SEM view of the $M^2 - TFG$	16
2.2	ANSYS simulations showing the drive and sense resonant modes of the $M^2 - TFG$	17
2.3	System block diagram of the control loops of the $M^2 - TFG$	19
2.4	Equivalent RLC circuit representation of a micromechanical resonator.	24
3.1	Schematic representation of a TIA (with noise sources) interfaced with the microgyroscope.	28
3.2	Series resonant oscillator showing impedances that load the quality factor.	31
3.3	Schematic of the T-network TIA interfaced for capacitive detection.	36
3.4	Summary of amplifier configurations with expressions for signal gain and noise gain.	38
3.5	Schematic of (a) simple TIA and (b) T-network TIA with the relevant components for noise gain calculations.	39
3.6	Simulation results showing transimpedance gain of the T-network TIA (top) and comparison of noise gain for simple and T-TIA configurations (bottom).	40
3.7	Schematic of the low noise op-amp used for in the T-TIA.	41
3.8	Transimpedance gain characterization of the T-TIA.	42
3.9	Measured input-referred current noise for the front-end T-TIA as a function of R_F	43
3.10	Measured transimpedance gain and phase relationship for the T-TIA with a transimpedance gain of $1.6M\Omega$	45
3.11	Measured output voltage noise of the core amplifier and the T-network TIA for $R_F = 1.6M\Omega$	46
3.12	Measured SNR plot of the T-TIA for $R_F = 1.6M\Omega$ at 10kHz.	47

4.1	Schematic of the drive loop oscillator loop with the automatic level control circuit.	49
4.2	Drive oscillator spectrum and buffered output waveform.	50
4.3	Block diagram of the PLL-based drive loop.	52
4.4	Voltage waveforms showing the input drive signal from the PLL and the output signal from the gyroscope.	52
4.5	Schematic view of the x-axis drive combs with relevant dimensions. .	53
4.6	Measured variation of drive amplitude as a function of input drive signal.	54
4.7	Circuit schematic of the Gilbert Cell used for synchronous demodulation.	56
4.8	Input and output waveforms showing modulation and demodulation.	56
4.9	Rate response and scale factor of gyroscope.	57
4.10	0.5 μ m CMOS ASIC for gyroscope drive and sense channels.	58
4.11	0.5 μ m CMOS ASIC and MEMS die on custom PCB.	58
5.1	Sources of quadrature error in TFG (a) and a shell structure (b). . .	61
5.2	Conceptualization of quadrature nulling in the $M^2 - TFG$ by use of rotating torques.	64
5.3	Dedicated quadrature nulling electrodes in the $M^2 - TFG$	65
5.4	Tuning characteristics of the sense and drive resonant frequencies. . .	67
5.5	Measured frequency response function of the TFG showing mode-matching, as observed at one of the sense electrodes.	68
5.6	Characteristics of the TFG at mode-matched condition.	75
5.7	Close up of ZRO values as mode-matching is achieved, showing linear and parabolic regions.	75
5.8	Flow-chart showing the proposed automatic mode-matching scheme. .	76
6.1	Schematic of the automatic mode-matching system.	79
6.2	Schematic of the envelope detector.	80
6.3	Measured input-output characteristics of the envelope detector and waveforms showing amplitude stepped 20kHz input signal and corresponding output (Inset) Response of the envelope detector to 1mV change in input amplitude.	81
6.4	Schematic of the sigma-delta modulator.	83
6.5	Measured response of the $\Sigma\Delta$ to sinusoidal and ramp input signals. .	83

6.6	Measured noise spectrum of the $\Sigma\Delta$ modulator showing the first order noise shaping with maximum SNR of 88dB/Hz. Plot of SNR vs. relative input signal level.	84
6.7	Timing Diagram showing relationship between control signals and sensor outputs.	85
6.8	Schematic of the V_P stepper.	87
6.9	Schematic of the current cell used in the DAC of the V_P stepper. . . .	87
6.10	Measured output of the DAC and the measured INL and DNL.	88
6.11	Results of the V_P stepper.	89
6.12	Initial separation between the modes and minimum achievable separation without quadrature nulling.	90
6.13	Time domain plot showing increase of the ZRO with VP.	90
6.14	Mode-matched operation showing Q_{EFF} of 36,000.	91
6.15	Microgyroscope waveforms at mode-matched condition showing the 90° phase difference between drive output and ZRO.	92
6.16	Mode-matching as a function of temperature.	92
6.17	Long-term stability of the mode-matched gyroscope.	94
6.18	Scale factor measurement and output of gyroscope sinusoidal rates. .	95
6.19	Concept of electronic bandwidth controlled using controlled split up or resonant modes.	96
6.20	System implementation of programmable bandwidth control.	97
6.21	Scale factor measurement for V_P settings.	98
6.22	Scale factor vs. measured effective quality factor for different bandwidths.	98
6.23	Scale factor vs. frequency for different V_P settings.	99
6.24	CMOS ASIC for gyroscope drive and sense channels.	100
7.1	Typical Allan variance plot for a gyroscope showing the portions corresponding to the different noise sources.	105
7.2	SIMULINK model for noise sources that contribute to the drift in a gyroscope system.	109
7.3	Power spectral density plots for the flicker, thermal and total noise generated by the SIMULINK model.	110

7.4	Root Allan variance of total system noise for different flicker noise corner frequencies.	111
7.5	Allan Variance plot of the $40\mu m$ TFG.	113
7.6	Allan Variance plot of the $60\mu m$ TFG.	114
7.7	Root Allan Variance plot of the $M^2 - TFG$ for different temperatures.	115
7.8	Root Allan Variance plot of the $M^2 - TFG$ for different sensor bandwidths.	116
7.9	Comparison of drift from bulk macromachined and MEMS gyroscopes of different configuration.	119
7.10	Bias drift plot from VSG series of rate sensors from Silicon-Sensing.	119
7.11	Bias drift plot from ADXRS series of rate sensors from Analog Devices.	120
7.12	Bias drift plot from the SAR-10 gyroscope Imego/ Sensor-Nor.	121
7.13	Bias drift plot from the DRS-MM3 gyroscope Bosch.	121
7.14	Bias drift plot from the VG700 series of gyroscopes Cross-Bow.	122
7.15	Bias drift plot from the FOG's developed by Andrew Corporation.	123
7.16	Bias drift plot from the FOG developed by Fibersense Technology.	123
8.1	Block-diagram of closed-loop operation of the $M^2 - TFG$	128
8.2	Schematic of the 2^{nd} order $\Sigma\Delta$ modulator.	130
8.3	Noise shaping advantage of the 2^{nd} order $\Sigma\Delta$ modulator.	130
8.4	Measured waveforms and frequency spectrum of the 2^{nd} order $\Sigma\Delta$ modulator.	131
8.5	Schematic and die micro-graph of the 4-bit flash ADC.	132
8.6	Measured waveforms of input and output of 4-bit flash ADC. Measured Input-output characteristics and INL	133
8.7	Conceptual representation of Q-loading to increase open-loop bandwidth.	133
B.1	SIMULINK model of the gyroscope.	140
B.2	Frequency domain behaviour showing ω_{SNS} decreasing with increasing V_P , while ω_{DRV} stays relatively constant.	141
B.3	Time domain behaviour showing phase relationships between signals at mode-matched condition.	142

B.4	Time domain behaviour showing ZRO amplitude increasing as VP nears the value required for mode-matching. The mode also captures the 90° phase shift that occurs at mode-matched condition.	143
B.5	Frequency domain behaviour showing that sensor sensitivity is maxi- mum when the frequency of sense mode is equal to that of drive mode.	144
B.6	Modeling of the automatic mode-matching scheme showing how ZRO level increases as the frequency separation between drive and sense modes are decreased. Note that the VP does not increment once the maximum in ZRO level has been reached.	145
B.7	Simulation waveforms from Cadence showing the increase and then decrease in ZRO amplitude as the DAC is stepped past the optimum value required for mode-matched operation.	147
C.1	Schematic of the discrete implementation of the gyro control electronics.	148
C.2	Schematic diagram of the discrete PLL drive loop electronics.	149
C.3	Schematic diagram of the discrete multiplier (AD835).	150
C.4	Schematic of the discrete implementation of the 2 nd order Sallen-Key filter.	150
D.1	Effects of V_P variation on long-term stability.	152
D.2	System incorporating a gyro and accelerometer, where gyro output is high-pass filtered.	153
D.3	Root Allan Variance without applying any filtering.	154
D.4	Filter characteristics of the high-pass filter used for bias drift estimation.	154
D.5	Root Allan Variance after filtering with the HPF.	155

SUMMARY

Micromachined gyroscopes constitute one of the fastest growing segments of the microsensor market. The application domain of these devices is quickly expanding from automotive to consumer and personal navigation systems. Examples include anti-skid and safety systems in cars and image stabilization in digital cameras. However, MEMS angular rate sensors today do not meet the sub-degree-per-hour resolution and bias drift requirements needed in high precision applications such as inertial measurement units (IMU) for GPS augmented navigation, robotics, unmanned surveillance vehicles, aircraft and personal heading references.

The objective of our research is to develop system architectures and CMOS circuits that interface with high-Q silicon micromachined vibratory gyroscopes to implement navigation-grade angular rate sensors. The MEMS sensor used in this work is an in-plane bulk-micromachined mode-matched tuning fork gyroscope ($M^2 - TFG$), fabricated on silicon-on-insulator substrate. The use of CMOS transimpedance amplifiers (TIA) as front-ends in high-Q MEMS resonant sensors is explored. A T-network TIA is proposed as the front-end for resonant capacitive detection. The implemented T-network TIA provides on-chip transimpedance gains of up to $25M\Omega$, has a measured capacitive resolution of $0.02aF/\sqrt{Hz}$ at 15kHz, a wide dynamic range of 104dB in a bandwidth of 10Hz and consumes $400\mu W$ of power.

Another important contribution of this work was developing a scheme to substantially improve the noise and drift of micromachined gyroscopes by adaptively biasing the mechanical structure, such that the sensor is operated in so-called mode-matched condition. Mode-matching leverages the inherently high quality factors of the microgyroscope and results in significant improvement in the Brownian noise floor,

electronic noise, sensitivity and bias drift of a microgyroscope. We developed a novel architecture that utilizes the often ignored residual quadrature error in a gyroscope to achieve and maintain perfect mode-matching (i.e. $\approx 0Hz$ split between the drive and sense mode frequencies), as well as electronically control the sensor bandwidth. A CMOS implementation was developed that allowed mode-matching of the drive and sense frequencies of a gyroscope at a fraction of the time taken by current state-of-the-art techniques. Further, this mode-matching technique allows for maintaining a controlled separation between the drive and sense resonant frequencies, providing a means to increasing sensor bandwidth as well as dynamic range. The mode-matching CMOS IC, implemented in a $0.5\mu m$ 2P3M process, and control algorithm have been interfaced with a $60\mu m$ thick mode-matched tuning fork gyroscope ($M^2 - TFG$) to implement an angular rate sensor with bias drift as low as $0.3^\circ/hr$ - two orders of magnitude lower than commercially available gyroscopes and the lowest recorded to date for a silicon MEMS gyro.

CHAPTER I

MICROMACHINED VIBRATING SILICON GYROSCOPES

The aim of this dissertation is the research and development of CMOS circuits and systems that interface with micro-electromechanical (MEM) gyroscopes to implement compact, high performance angular rate sensing microsystems. A gyroscope (Gk. *gyros* circle, *skopien* to watch) is a sensor used to measure angle or velocity of rotation. Spinning wheel gyroscopes that rely on conservation of angular momentum were used for the most part of the previous century. In recent years, the advent of micromachining technology has made MEMS-based angular rate sensors increasingly common.

The system architecture and electronic control circuitry of a gyroscopic sensor depends on the technology used to implement the sensor element itself. Micromachined gyroscopes use vibrating elements to sense rotation and are devoid of any rotating parts or bearings. This makes them ideally suited for inexpensive batch fabrication using planar processes and for potential integration with CMOS circuitry [1]. This work will therefore focus on systems and control circuits for these micromachined gyroscopes, or microgyros for short.

1.1 Applications and Market Demands

Despite the ubiquitous digitization that we see around us, the world we live in is an inherently analog realm. Hence the rapid growth in sensors and sensing technologies to allow for interfacing of these two domains. MEMS gyroscopes provide the ability to sense rotation inexpensively for a number of conventional as well as emerging

applications and therefore form one of the largest growing market segments within the microsensor industry.

Micromachined gyroscopes were traditionally used in the automotive industry for anti-skid traction control systems, roll-over detection, next generation airbag systems and anti-lock brake systems (ABS). There has been an increased focus among major automobile manufacturers in North America, Europe and Japan to implement electronic stability control (ESP) systems in cars [2]. It is expected that by 2009, most cars will have an ESP system for additional driver safety, and this application is one of the major factors contributing to the growth of the microgyroscope market. In addition, there are numerous emerging applications for MEMS gyroscopes in the consumer electronics sector. These include image stabilization in digital cameras, smart user interfaces in handhelds, visual graphics, gaming, and inertial pointing devices. Some of the major players in the commercial microgyroscope market include Analog Devices, ST Microelectronics, and Robert Bosch GmbH.

Since its invention in 1910, the gyroscope has been integral part of all inertial measurements units (IMU) and inertial navigation systems (INS). Inertial navigation is the process of determining the position of a body in space by using the measurements provided by accelerometers and gyroscopes installed on the body. The components of acceleration and rotation rate can consequently be combined to yield the object's accurate position in space. An IMU is a self-contained system that can perform accurate short-term navigation of a craft/object in the absence of global positioning system (GPS) assisted inertial navigation [3]. IMU's typically use three accelerometers and three gyroscopes placed along their respective sensitive axes to gather information about an object's direction and heading. They are vital components in aircraft, unmanned aerial/ undersea vehicles, GPS augmented navigation and personal heading references. Guidance systems and platform stabilization of missiles are but a few of the military applications that require

accurate angular measurements. High precision IMU's are of considerable interest to the petroleum industry and are used in down-hole electronics for real-time monitoring and correction of drilling in offshore rigs.

The applications space of microgyroscopes can be divided, based upon performance requirements, into two categories. Table 1.1 summarizes the requirements for rate-grade and navigation-grade gyroscopes. The various performance metrics for micromachined gyroscopes are explained in Section 1.3. The majority of automotive and consumer electronics applications require rate-grade performance, while higher precision navigation-grade devices are suitable for IMUs and high-end applications in aerospace and petroleum industry.

Table 1.1: Performance requirements for rate-grade and navigation grade gyroscopes.

Parameter	Rate Grade	Navigation Grade
Angle Random Walk	$> 0.5^\circ/\sqrt{hr}$	$0.001 - 0.1^\circ/\sqrt{hr}$
Bias Drift	$10 - 1000^\circ/hr$	$0.1 - 1^\circ/hr$
Scale Factor Accuracy	$1 - 10\%$	$0.1 - 1\%$
Full Scale Range	$100 - 1000^\circ/s$	$75 - 300^\circ/s$
Bandwidth	$> 100Hz$	$1 - 10Hz$

Currently, the most commonly used navigation-grade gyroscopes are fiber-optic gyroscopes (FOG's)[4], Ring-Laser Gyroscopes (RLG's)[5] and the hemispherical resonator gyroscope (HRG)[6]. Since FOG's and RLG's rely on optical means to detect rotation, they cannot be micromachined or integrated on-chip with CMOS circuitry and are therefore not suitable candidates for small form-factor IMU's. The HRG consists of a quartz shell and relies on mechanical means to sense rotation. Being a bulk-mechanical structure implemented using quartz, it is not amenable for incorporation into applications that demand high precision yet ultra low-power angular rate detection.

Thus far, research in micromachined gyroscopes has been focused toward implementing low-cost sensors targeting rate-grade performance. A navigation-grade

MEMS gyroscope will significantly lower the cost and form-factor, without sacrificing performance, of those systems that currently use FOG's and RLG's. It is envisioned that in the next 5 - 10 years, avionics, petroleum and military applications will become the driving force for the development of MEMS gyroscopes and inertial sensors.

1.2 *Principle of Operation*

Micromachined gyroscopes are based on the *Coriolis effect*, where rotation about an axis causes a transfer of energy between two vibratory modes that are orthogonal to the axis of rotation and to each other. For this reason, MEMS gyroscopes are categorized as Coriolis Vibratory Gyroscopes (CVGs)[7]. The Coriolis effect can be best understood by taking the example of a simple tuning fork, as shown in Fig 1.1. The tines of the tuning fork are excited into resonance along the x-axis. This mode is referred to as the primary mode or drive mode. When the tuning fork is rotated about the z-axis as shown, there is an apparent force that acts orthogonally on the tines. This apparent force is referred to as the Coriolis force and causes the tines of the tuning fork to deflect along the y-axis with an acceleration equal to $2\vec{v} \times \Omega_Z$. The deflection of the tines along the y-axis - referred to as the sense mode - is proportional to the input rotation rate, Ω_Z ; this effect is the basis of all vibratory gyroscopes.

Vibratory gyroscopes can operate either in a matched-mode or in split-mode condition [8]. Under matched-mode condition, the sense mode is designed to have the same (or nearly the same) resonant frequency as the drive mode. Hence, the rotation-induced Coriolis signal is amplified by the quality factor, Q of the sense mode (which can be high in vacuum). In split-mode condition, the drive and sense modes are separated in frequency and the effective mechanical amplification of the Coriolis signal at the drive frequency is low (~ 1). Due to Q amplification, gyroscopes operated under matched-mode configuration offer higher sensitivity and better resolution, and is the class of gyroscopes that are examined in this work.

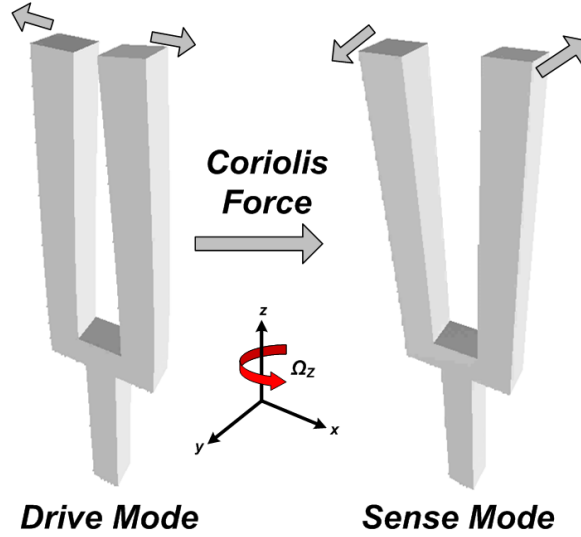


Figure 1.1: Demonstration of Coriolis Force.

Resonant matched devices are themselves further classified into two types depending upon the nature of their operating modes [8]. The first class of devices relies on non-degenerate vibration modes for driving and sensing, causing significant challenges in matching of the resonant modes. A tuning fork gyroscope [9] is an example of such a gyroscope. The second class of devices functions with inherently degenerate vibration modes which are therefore easier to match and operate under the matched condition. A shell-type gyroscope such as the resonating star gyroscope(RSG) [10] is an example of the second class of resonant matched gyroscope.

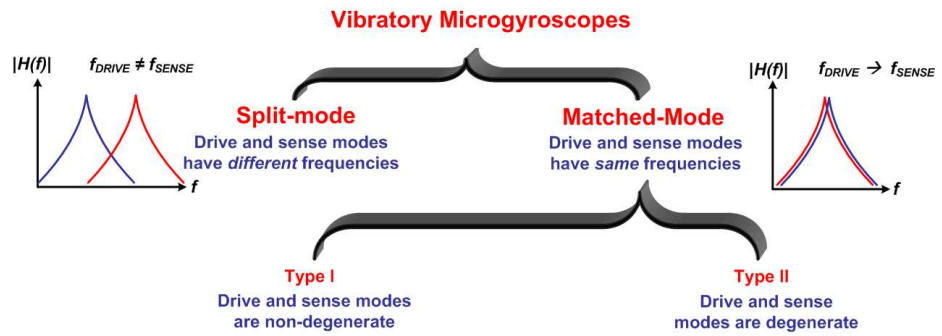


Figure 1.2: Types of gyroscopes.

1.3 Performance Specifications

Different parameters are used to specify a high performance vibratory gyroscope system. These performance metrics are briefly discussed below.

1.3.1 Resolution

The resolution of a gyroscope is the minimum rotation rate that can be distinguished from the noise floor of the system per square root of bandwidth of detection and is expressed in units of ($^{\circ}/s/\sqrt{Hz}$) or ($^{\circ}/hr/\sqrt{Hz}$). The overall resolution of the microgyroscope (total noise equivalent rotation ($TNE\Omega$)) is determined by two uncorrelated components: the mechanical (or Brownian) noise equivalent rotation ($MNE\Omega$) and the electronic noise equivalent rotation ($ENE\Omega$).

$$TNE\Omega = \sqrt{MNE\Omega^2 + ENE\Omega^2} \quad (1.1)$$

The Brownian motion of the structure caused by molecular collisions from the surrounding medium represents the mechanical noise component of any vibratory gyroscope [1]. By equating the displacement caused by Brownian motion to the displacement induced by Coriolis acceleration, one may derive the mechanical resolution of a vibratory microgyroscope as given by Eq.(1.2):

$$MNE\Omega \propto \frac{1}{q_{Drive}} \sqrt{\frac{4k_B T}{\omega M Q_{EFF}}} \sqrt{BW} \quad (1.2)$$

The quantities k_B , T , and BW represent the Boltzmann's constant ($1.38 \times 10^{-23} \text{ Joules/K}$), operating temperature (K) and measurement bandwidth (Hz) respectively. In the expression ω_0 is the resonant frequency of the sensor and M its mass. q_{drive} is the amplitude of vibration along the reference axis and Q_{EFF} is the effective quality factor of the system. For a given mechanical structure, Q_{EFF} can be maximized by matching the frequencies of the drive and sense modes, as will be explained in a subsequent section.

The electronic noise floor is dependent upon the input referred noise of the front-end electronic interface. Assuming the circuit noise V_n has a white spectrum near the operating frequency, and is the only factor that limits rotation resolution, the minimum detectable rotation rate equivalent to the electronic noise floor is given by Eq.(1.3).

$$ENE\Omega \propto \frac{g_0^2 \omega_0 C_{Parasitics} V_n}{V_P Q_{Drive} Q_{EFF}} \sqrt{BW} \quad (1.3)$$

where g_0 and V_P represent the rest sense gap and the DC polarization voltage applied to the substrate, respectively. $C_{Parasitics}$ is the total parasitic capacitance between the sensor and the electronic front-end and has contributions due to pads, bond-wires and circuit gate capacitances. It is evident from both equations that drive amplitude, device mass, sense gap, and effective quality factor, all play a key role in determining the overall noise floor.

The noise floor of a gyroscope is often expressed in terms of angle random walk (ARW). This is a measure of the angular error buildup with time that is due to white noise in angular rate. This error is typically expressed in degrees per square root of hour ($^\circ/\sqrt{hr}$). The relation between the noise floor per unit bandwidth and the ARW is given by:

$$Noise\ floor(^{\circ}/hr/\sqrt{Hz}) \equiv ARW(^{\circ}/\sqrt{hr}) \times 60 \quad (1.4)$$

1.3.2 Scale Factor

Coriolis-induced sense mode deflections of the proof-masses are detected through capacitive, piezoresistive, piezoelectric or optical means. The scale factor of a microgyroscope is the ratio of a change in output to a change in the input intended to be measured (i.e., rotation). Scale factor is generally evaluated as the slope of the straight line that can be fit by the method of least squares to input-output data [7],

and is most commonly expressed in units of $Volts/^{\circ}/sec$.

In a vibratory gyroscope, the sense mode deflections are proportional to the effective quality factor (Q_{EFF}) and the proof-mass displacement along the driven axis, q_{Drive} . Q_{EFF} in turn is significantly dependent on the separation between the drive and sense resonant mode frequencies and is addressed in detail in Chapter 6. Increasing sense mode deflections, while maintaining a high aspect ratio for the capacitive gaps for sensing, allows for large changes in the sense capacitance (ΔC), thereby generating a larger electrical pick-off signal for a given input rotation rate. Therefore, high effective quality factors, large drive amplitudes, low parasitics, and a high sense capacitance (C_{S0}) aspect ratio, all contribute to a high gyro scale factor, as shown in Eq.(1.5):

$$Scale\ Factor \propto \frac{2V_P C_{S0} Q_{EFF} q_{Drive}}{(C_{S0} + C_{Parasitics}) g_0 \omega_0} \quad (1.5)$$

1.3.3 Zero Rate Output and Bias Stability

Zero rate output (ZRO) is the output signal from the gyroscope in the absence of input rotation. The drift of this ZRO bias (referred to as Bias drift and expressed in $^{\circ}/hr$) is an important metric that ultimately determines the long-term stability of a microgyroscope. In inertial navigation systems, gyroscopes are used along with accelerometers to obtain heading information, i.e., position and orientation. The rate information from the gyroscope is integrated to obtain the angle. Any long term variations in the rate - of which the bias drift is an accurate indicator - add up, and can cause a large error in angle information. Modern gyroscope systems periodically calibrate themselves with GPS to ensure that the heading information is accurate. However, a long interval between calibration sequences is crucial for applications such as deep sea navigation and oil exploration, where it is not possible to resurface very easily to calibrate with GPS. In such cases, the longer a system can function

accurately without the need for calibration, the better and more accurate heading and orientation information it can deliver.

While the noise floor of an amplifier is the analogue of microgyro resolution, DC offset drift in the amplifier can be considered the equivalent of gyro bias drift. The bias drift of a gyro is comprised of systematic and random components. The systematic components arise due to temperature variations, linear accelerations, vibrations and other environmental factors [7]. The random component has been found to have a $1/f$ characteristic, which depends significantly on the noise floor of the gyroscope - hence techniques that improve the gyro resolution, also result in very low bias drift. Empirical studies have formulated an expression that can predict drift in gyroscopes [11], but considerable research remains to be done.

$$Bias\ Drift \propto \frac{\omega_0^2}{Q_{DRIVE}Q_{SENSE}Area_{Electrodes}} \quad (1.6)$$

Due to the relation between the bias drift and the noise floor of a gyro, a measure of the gyro power spectral density (PSD) was used to measure drift. However, the Allan Variance technique has recently been used to specify the drift of a microgyroscope [7]. A detailed analysis of the bias drift is presented in Chapter 7 and Appendix A.

1.3.4 Bandwidth and Dynamic Range

The bandwidth of the microgyroscope determines the response time of the system. Response or settling time of the microsystem is the time required for the output to settle to within a certain range of the expected value for an input step function. The sensor bandwidth (BW) is related to the resonance frequency (ω_0) and quality factor (Q) by:

$$BW = \frac{\omega_0}{2Q} \quad (1.7)$$

The bandwidth requirements for a gyroscope depend on its application. Applications

which demand very low rate resolutions typically require small bandwidths ($\sim 1\text{Hz}$); e.g., for use in gyrocompass navigation, where settling times of 1 minute are tolerable. However, other applications such as automotive roll-over detection require a larger bandwidth to detect the high yaw rates associated with vehicular skidding.

Dynamic range refers to the range of input values over which the output is detectable. It is typically computed as the ratio between the maximum input rotation rate (full scale rate) that the sensor can tolerate and the system noise floor.

1.4 Motivation

Figure 1.3 below compares the performance of a FOG [12], the HRG [6], the Systron Donner Quartz Tuning Fork sensor [13], the ADXRS401 iMEMS gyroscope from Analog Devices [14] and the Honeywell GG1178 sensor [15]. While the MEMS sensors have a far smaller form-factor and are much more cost-effective, their bias drifts and noise floors must be lowered by at least two orders of magnitude if they are to compete with, and eventually replace, the FOG or the HRG.

Parameter	FOG	HRG	Systron/ BEI	Honeywell	ADI
Technology	Fiber-optic	Quartz shell	Quartz tuning fork	Dual axis MEMS gyro	Dual-accelerometer
Noise density	$3 \times 10^{-4} \text{ }^\circ/\text{s}/\sqrt{\text{Hz}}$	$1 \times 10^{-4} \text{ }^\circ/\text{s}/\sqrt{\text{Hz}}$	$5 \times 10^{-2} \text{ }^\circ/\text{s}/\sqrt{\text{Hz}}$	$3 \times 10^{-3} \text{ }^\circ/\text{s}/\sqrt{\text{Hz}}$	$5 \times 10^{-2} \text{ }^\circ/\text{s}/\sqrt{\text{Hz}}$
Bias Drift	$2^\circ/\text{hr}$	$1^\circ/\text{hr}$	$180^\circ/\text{hr}$	$90^\circ/\text{hr}$	$50^\circ/\text{hr}$
Full Scale Range	$\pm 200^\circ/\text{s}$	$\pm 500^\circ/\text{s}$	$\pm 100^\circ/\text{s}$	$\pm 360^\circ/\text{s}$	$\pm 150^\circ/\text{s}$
Sensitivity			$17.5 \text{ mV}/^\circ/\text{s}$	$25 \text{ mV}/^\circ/\text{s}$	$12.5 \text{ mV}/^\circ/\text{s}$
Size	450cm^3	4 inch^3	2.5 inch^3	50cm^3	0.14cm^3
Power	$\sim 6.3\text{W}$	$\sim 8\text{W}$	250mW	500mW	30mW
Cost	$\sim 5000\$$	$> 10,000\$$	$\sim 100\$$	$> 100\$$	$\$30$
Model No.			QRS14	G5200	ADXRS401

Figure 1.3: Summary of FOG, HRG and MEMS gyroscopes.

Since 1991, the performance of micromachined gyroscopes, indicated by the ARW, has improved by a factor of $10\times$ every two years as shown in Fig 1.4. It is anticipated that a continuing improvement in the performance of micromachined gyroscopes

(resolution, bias stability, dynamic range, etc.) will be seen over the next decade.

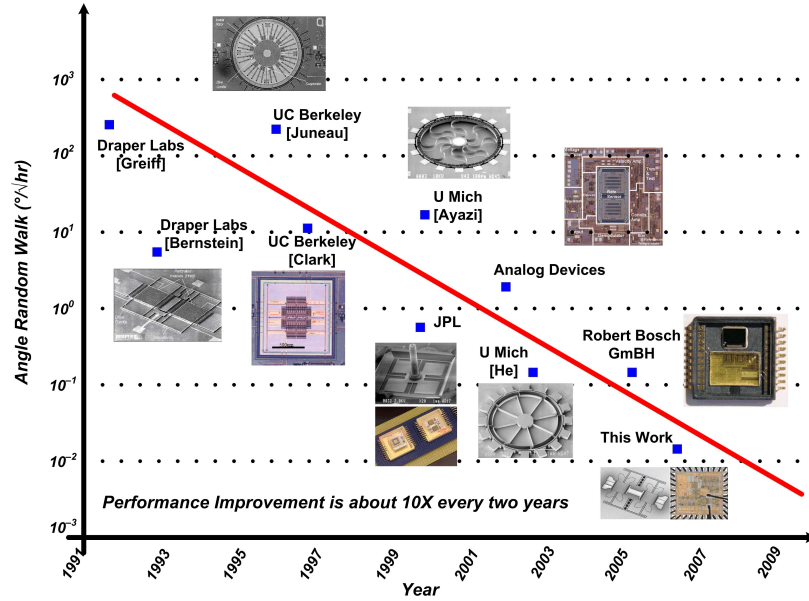


Figure 1.4: Performance scaling of micromachined gyroscopes.

As silicon vibratory gyroscopes attain navigation grade performance, the interface electronics that actuate, sense, and control these micromechanical structures are key elements in determining the overall performance of the micro-gyro system. The objective of this research is to develop low noise and low power CMOS electronic systems for navigation-grade MEMS gyroscopes. As seen from Table 1.1, while navigation grade gyroscopes have similar full-scale ranges as rate-grade devices, their noise floors are on the order of $0.1^\circ/hr$. Since vibratory microgyroscopes, like micromachined accelerometers, are capacitive sensors, there is a need for ultra-low-noise front-ends which must be able to detect sub-atto Farad capacitance changes in navigation-grade sensors. In addition, while mechanical structures can typically attain dynamic ranges in excess of 120 dB, designing front-end electronics with such a large dynamic range is challenging. The dynamic range is limited by the supply voltage on the one hand and the noise floor on the other.

Significant progress has been made in developing MEMS process flows that are

fully CMOS compatible [14]. However, as explained in Chapter 3, current state-of-the-art high aspect ratio processes are not yet CMOS compatible. This calls for a two-chip solution to retain the inherent cost-effectiveness of MEMS batch fabrication. Hence it is necessary to develop interface circuit architectures that do not place emphasis on MEMS-CMOS single-chip integration.

Matched-mode operation of gyroscopes leverages the mechanical quality factor and provides a means to lower the bias drift and noise to navigation-grade levels. This research aims to develop novel control strategies and demonstrate low power CMOS implementations for the matched-mode operation of Coriolis vibratory gyroscopes. Post-fabrication mechanical trimming has been used in the past to match the resonant modes in both type I [16] and type II [13] gyroscopes. This is not feasible for navigation applications where it is impossible to predict or recreate the actual operating environment of the sensor at the time of manufacture. Recently, evolvable hardware solutions have been proposed [17] that use genetic algorithms to find and iteratively null the frequency separation between the resonant modes in a gyroscope. The best possible mode-matching achieved with the clover-leaf gyroscope by the teams from JPL and Boeing took about 1 hour, and required extensive external instrumentation. This is impractical for use in smart applications where it is necessary to calibrate gyroscopes in situ. The methods proposed and implemented in this work demonstrate a simple, low-power, cost-effective, and rapid means of automatic mode-matching to take advantage of the inherently high quality factor of micromachined gyroscopes.

The circuits, systems, and control algorithms developed during the course of this work were designed for and interfaced with a bulk micromachined silicon-on-insulator (SOI) tuning fork gyroscope. With an angle random walk of $0.003^\circ/\sqrt{hr}$ and a bias drift as low as $0.16^\circ/hr$, the Mode-Matched Tuning Fork Gyroscope ($M^2 - TFG$) is the most accurate MEMS silicon gyro system to date (Fig 1.4).

1.5 Thesis Organization

The remainder of this dissertation is organized as follows.

Chapter 2 provides a system level overview of microgyroscope interfacing. Most of the discussion on microgyro interfaces found in this dissertation can be applied to a wide range of micromachined angular rate sensors. However, for sake of brevity and clarity, most of the work and results are discussed in the context of a bulk-micromachined high-Q SOI tuning fork gyroscope (TFG), also referred to as mode-matched tuning fork gyroscope ($M^2 - TFG$).

Chapter 3 discusses the use of CMOS transimpedance amplifiers (TIA) as front-ends for motional current detection in MEMS gyroscopes. A low-noise T-network based CMOS TIA is proposed as the front-end for the low-noise motional current detection. The challenges involved with the design and interface for these ultra-low noise front-ends are discussed in the context of microgyroscope interfacing.

Chapter 4 deals with CMOS implementation of the drive and sense electronics for the $M^2 - TFG$. Two drive oscillator topologies are presented: the first is based on a series resonant electromechanical oscillator approach and the second is based on a PLL-oscillator. CMOS implementations of the synchronous demodulator for rotation rate sensing are then presented.

Quadrature error and mode-matching of gyroscopes is the subject of Chapter 5. A detailed explanation of the origins and impact of quadrature error lays the foundation for the development of mode-matched gyroscopes. The chapter also reviews the state of the art in the development of automatic mode-matching schemes for microgyros. A novel scheme to achieve real-time mode-matching of microgyros has been developed and is presented.

Chapter 6 discusses the CMOS implementation of the proposed mode-matching scheme. The various circuit blocks are discussed and their impact on overall system performance is analyzed. Interfacing results of the CMOS system with the control

algorithm and the MEMS sensor are presented.

Bias drift in microgyroscopes has received significant attention over recent years in MEMS based inertial measurement units (IMUs). Chapter 7 presents a detailed analysis of bias drift in micromachined gyroscopes. The bias drift of the microsystem implemented here is compared with commercial MEMS solutions.

Finally, Chapter 8 provides an overview of the contributions of this work and identifies possible future directions of research in the field of integrated circuits for MEMS gyroscopes.

CHAPTER II

SYSTEM LEVEL CONSIDERATIONS FOR MEMS GYROSCOPES

The basic operating principles and electronic system architectures remain the same for any Coriolis vibratory Gyroscope (CVG). As previously mentioned, this work primarily discusses design of circuits and systems for a Type I tuning fork gyroscope (TFG) operated with the drive and sense resonant modes matched in frequency. While most of the discussions and analyses of the systems and circuits presented in this work specifically apply to the TFG, they can, with very slight modifications, be applied to other vibratory gyroscopes, such as the resonating star gyroscope (RSG) that operates at frequencies typically less than 100kHz.

2.1 Mode-Matched Tuning Fork Gyroscope - Device Operation

Figure 2.1 shows the SEM view of the in-plane tuning fork gyroscope fabricated on $50\mu\text{m}$ thick silicon-on-insulator (SOI) substrate using a simple two-mask process similar to the one used for micro-gravity accelerometers reported in [18]. The gyroscope is comprised of two proof-masses, supported by flexural springs, and anchored at a central post. Actuation, sensing and tuning electrodes are distributed around the proof-masses and flexures.

The two proof-masses are analogous to tines of a tuning fork (Fig 1.1) and are driven at resonance along the x -axis using interdigitated comb-drive electrodes. When the sensor undergoes a rotation about the z -axis, the resultant Coriolis acceleration causes the proof masses to move along the y -axis. The magnitude of the Coriolis acceleration is given by the vector cross product of the input rotation

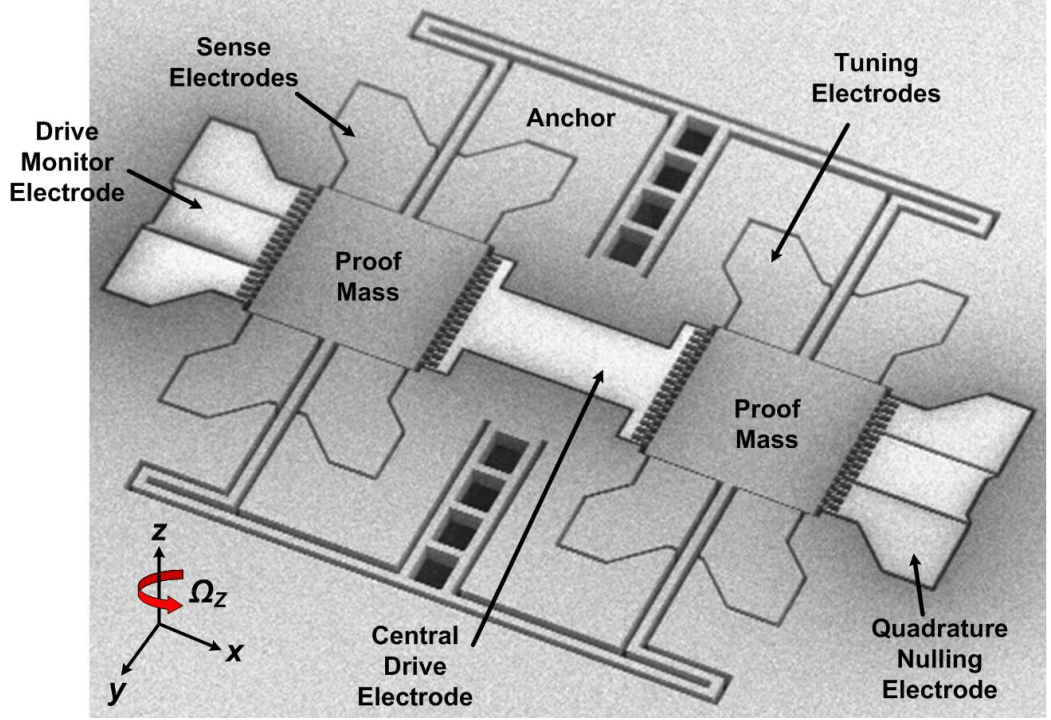


Figure 2.1: SEM view of the $M^2 - TFG$.

rate vector and the velocity of the proof mass as measured in the rotating reference frame. Considering that the proof-masses are oscillating sinusoidally when driven to resonance along the drive mode, the expression for the Coriolis acceleration (\vec{a}_y) is given by:

$$\vec{a}_y = 2\Omega_Z(t)v_{Drive}(t) = 2\Omega_Z(t)q_{Drive}\omega_x\cos(\omega_x t) \quad (2.1)$$

where Ω_Z is the input rotation rate, v_{Drive} is the velocity in the driven mode, q_{Drive} is the amplitude of oscillation in the driven mode and ω_x is the driven mode resonant frequency. This expression shows that the Coriolis acceleration generated in the CVG is an amplitude modulated (AM) sinusoid, which, in the frequency domain, appears as a dual sideband signal centered at the resonant frequency. The drive and sense resonant mode shapes are shown in Fig 2.2. The rotation induced proof-mass movement along the y -axis causes the gap between the parallel plate sense

electrode and the proof-mass to change. The change in capacitive gap is proportional to the input rotation rate $\vec{\Omega}_Z$, and is detected electronically. The structure is fully differential and symmetric. Therefore, any linear vibration or linear acceleration is rejected as common mode in the mechanical domain, which significantly alleviates the requirements on the electronic circuitry.

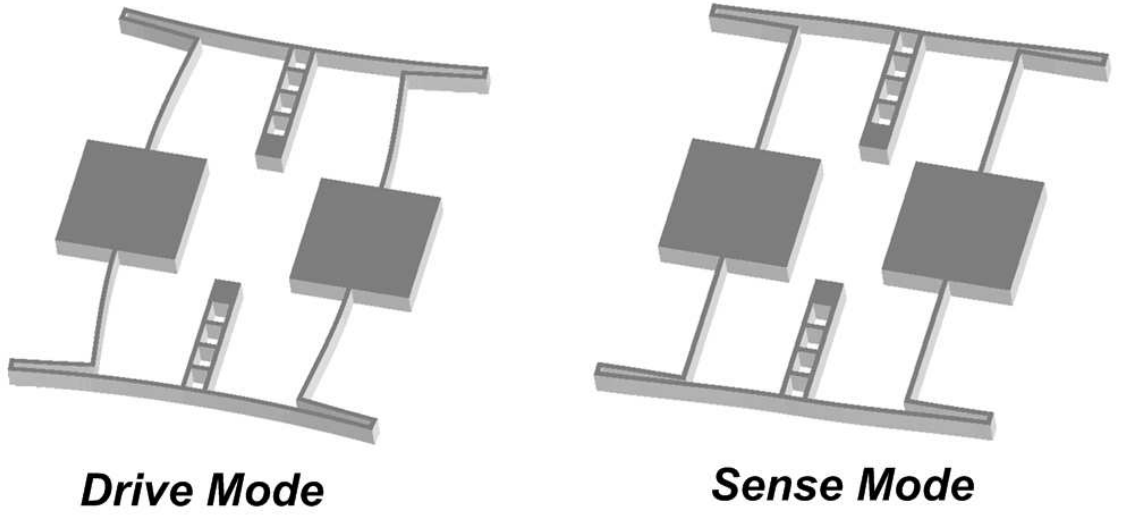


Figure 2.2: ANSYS simulations showing the drive and sense resonant modes of the $M^2 - TFG$.

The gyroscope is a resonant sensor, and the flexural springs have been designed to ensure that the mechanical drive and sense mode quality factors are in excess of 50,000 [19]. The flexures have also been designed to minimize any coupling between the two modes, while allowing for drive amplitudes in excess of $4\mu m$. In addition to improving sensor performance, such large quality factors significantly ease the design of the interface electronics. The resonant frequencies are in the range of $10 - 20 kHz$. The sensor structure is maintained at a DC polarization voltage (V_P) to provide the bias for capacitive transduction and to prevent frequency doubling of the drive force [20].

Table 2.1 summarizes the key mechanical parameters of the sensor used in this work.

Table 2.1: Mechanical parameters of the sensor used in this work.

Parameter	Value	Unit
Sensor resonant frequency (ω_O)	15	kHz
Sensor Dimensions	1.5×1	mm^2
Proof-mass dimensions	400×400	μm^2
Thickness of the structure (h)	40	μm
Sense capacitor gap (d_{SO})	≈ 5	μm
Comb over-lap (w)	2	μm
Number of drive combs (N)	32	—
Drive comb gap (g)	7	μm
Drive displacement(q_{DRIVE})	≈ 2.5	μm
Drive Quality factor (Q_{DRV})	78,000	—
Sense Quality factor (Q_{SNS})	44,000	—
Matched-mode effective Quality Factor (Q_{EFF})	30,000	—
DC Polarization Voltage (V_P)	80	V

2.2 *Electronic System Description*

High performance electronics for the actuation, sensing and control of the CVG are essential to realize navigation-grade performance. A CVG has a number of control loops, such as for automatic gain control of the drive amplitude, vibration frequency control at the resonant natural frequency and quadrature vibration nulling. Fig 2.3 below shows a schematic overview of the constituent system blocks in a typical microgyroscope system that has been implemented in this work.

Based on functionality, the electronics for any vibratory microgyroscope can be divided into the following subsystems:

2.2.1 Drive Loop

The drive loop electronics are responsible for starting and sustaining oscillations along the reference axis at constant amplitude. It is essential that a constant drive amplitude be maintained, as any variation in the drive amplitude manifests itself as a change in velocity of the mechanical structure (along the driven axis). Velocity fluctuations modulate the sensor output and can result in false or inaccurate rate

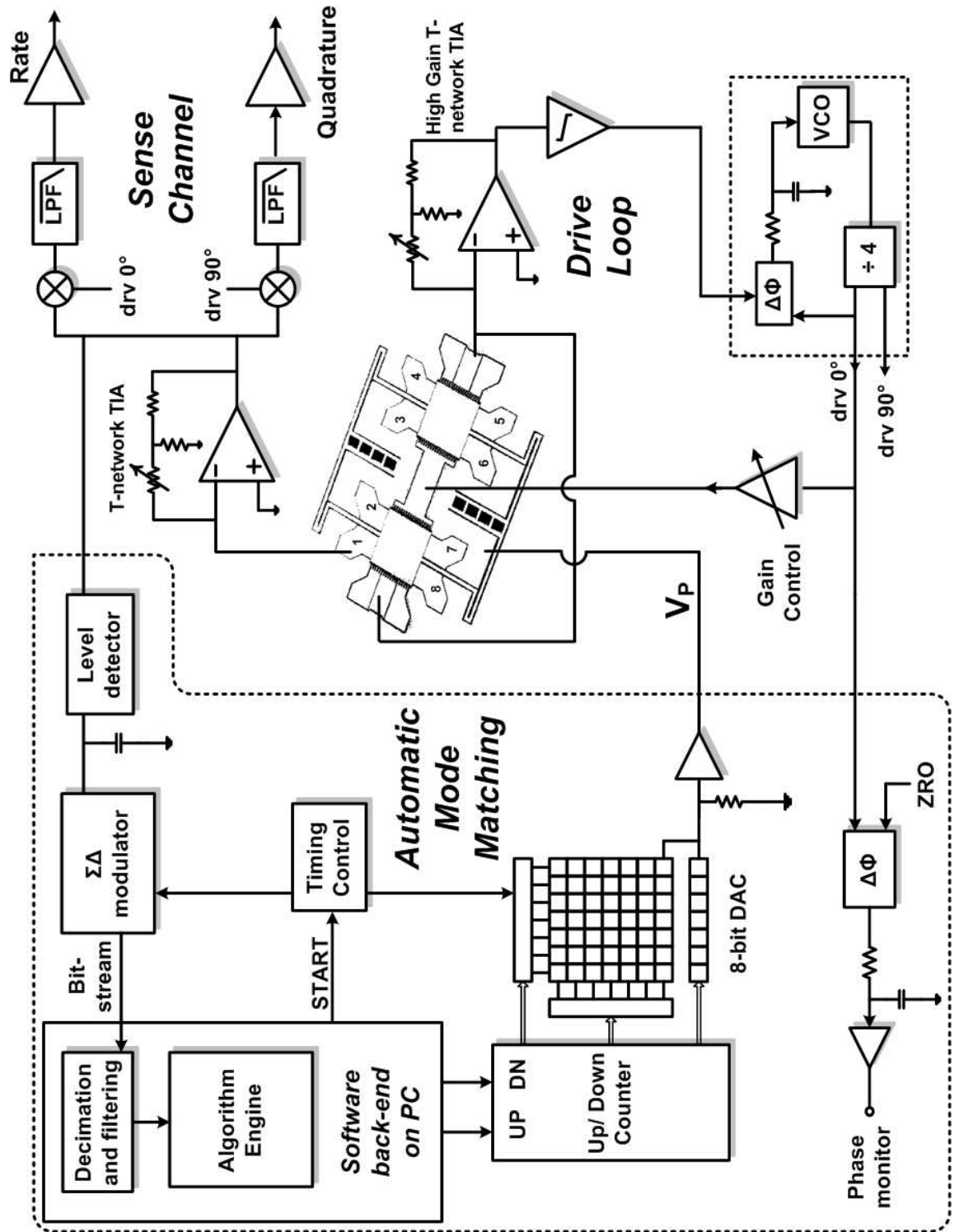


Figure 2.3: System block diagram of the control loops of the $M^2 - TFG$.

output. The drive loop uses an automatic level control (ALC) circuit to achieve and maintain constant drive amplitude. There are two approaches to implement the drive loop, both of which have been implemented in this work:

- An electromechanical oscillator: Here the drive mode oscillations are started and sustained by using a positive feed-back loop that satisfies the Barkhausen's criteria (Loop gain = 1, Loop Phase shift = 0°). The gyroscope forms the frequency determining element of the electromechanical oscillator. A high mechanical quality factor for the drive resonant mode (Q_{DRV}) can significantly ease the design of the drive oscillator. A large drive-Q enables the oscillations to be built up and sustained using much smaller voltage levels.
- A Phase-Locked Loop(PLL) based approach: Here the reference drive vibrations are set-up using a phase locked loop (PLL) as shown in Fig 2.3. The PLL center frequency and capture range are set close to the drive resonant frequency of the gyroscope. On power up, the PLL locks on to the output of the front-end I-V converter. The PLL output is amplified or attenuated to achieve the desired voltage amplitude and used to drive the microgyroscope. A variable gain amplifier is used to implement ALC.

2.2.2 Quadrature Nulling and Mode-matching

Fabrication imperfections of the mechanical structure result in off-axis movement of the proof-mass, causing a residual displacement along the sense axis even in the absence of rotation [21] and is referred to as quadrature error. The quadrature error is minimized by varying the mechanical bias voltages on the dedicated quadrature nulling electrodes shown in the SEM image. A detailed explanation of the origins of quadrature error and methods to null the same are presented in Chapter 5.

As explained earlier, gyroscope performance is enhanced when the mechanical sense frequency is matched to the drive resonant frequency due to the mechanical

amplification provided by the effective quality factor (Q_{EFF}). However, due to the limits imposed by fabrication tolerances, the drive and sense frequencies are seldom equal. Even in structures that have inherently degenerate mechanical frequencies, there always exists a finite separation after fabrication. Therefore it is necessary to use some other means - either electronic or mechanical - to decrease the separation between the two resonant frequencies until they are the same. This mode-matching is usually achieved by varying the mechanical bias voltages on the MEMS structure until the frequencies are equalized. Mechanical trimming is also commonly used post-manufacture to null the frequency separation. A detailed review of current mode-matching techniques and the benefits of mode-matching are presented in Chapter 5.

2.2.3 Sense Channel

The primary function of the sense channel is to extract the input rotation information from the gyroscope output. The AM Coriolis output is demodulated using the drive oscillator signal. This phase sensitive demodulation allows for the rejection of the interfering mechanically generated quadrature error, due to the inherent 90° phase difference between the quadrature and Coriolis signals. The low-pass filtered base-band signal is proportional to input rotation rate, and may be amplified if necessary at a later stage. Since synchronous demodulation allows for phase sensitive detection and rejection of quadrature error, it is preferred over other techniques such as envelope detection.

The CVG is termed *open-loop* if the sense axis motion is monitored but not controlled, and *force-rebalance* if the Coriolis induced displacements are nulled. The bandwidth of CVGs mechanized in the open-loop mode is directly related either to the time it takes the readout-mode vibration to take on its new steady-state value after a step change in input rate or to the separation of the two natural frequencies.

The required bandwidths are achieved in practice either by increasing the damping, or by separating the driven-mode and readout-mode natural frequencies. In open-loop mechanizations, there is therefore a trade-off between bandwidth and sensitivity, since increasing either the modes' frequency separation or damping results in a smaller steady-state response to a given inertial input rate.

2.3 Gyroscope System Modeling

The TFG can be conceptualized as a coupled resonator system, with the rotation-induced Coriolis force being the coupling element between the two resonant modes [22]. The dynamics of the microgyroscope are governed by Newton's Second Law of Motion. The ordinary differential equation (ODE) that relates proof-mass displacement along the drive axis (x) to applied forcing voltage v_{ac} (at the drive resonant frequency ω_x) for the $M^2 - TFG$ is given by:

$$\ddot{x} + \frac{D_x}{M}\dot{x} + \frac{K_x}{M}x = -\frac{V_P v_{ac}}{M} \frac{\delta C_{comb}}{\delta x} \quad (2.2)$$

where M is the effective mass of the gyroscope, V_P is the DC polarization voltage applied to the structure and $\frac{\delta C_{comb}}{\delta x}$ is the rate of change of comb-drive capacitance with displacement. For the comb-drive electrodes used in this work, $\frac{\delta C_{comb}}{\delta x}$, is given by Eq.(2.3),

$$\frac{\delta C_{comb}}{\delta x} = \frac{\epsilon_0 N h}{g} \quad (2.3)$$

where N is the number of inter-digitated combs, h is the thickness of the structure and g is the gap between adjacent combs. In Eq.(2.2), D_x and K_x represent the damping and mechanical stiffness terms, and are related to sensor parameters as follows:

$$D_x = \frac{\omega_x M}{Q} \quad (2.4)$$

$$K_x = \omega_x^2 M \quad (2.5)$$

Similarly, the ODE for the sense mode displacements (y) of the gyroscope operated open-loop, in response to an input rotation Ω_Z can be expressed as:

$$\ddot{y} + \frac{D_y}{M}\dot{y} + \frac{K_y}{M}y = 2\dot{x}\Omega_Z = 2q_{drive}\omega_x\Omega_Z \quad (2.6)$$

The stiffness term K_y along the sense axis incorporates the effects of electrostatic spring-softening via the term $-K_{elec}$ as shown in Eq.(2.8):

$$D_y = \frac{\omega_y M}{Q} \quad (2.7)$$

$$K_y = K_{mech} - K_{elec} = \omega_y^2 M - K_{elec} \quad (2.8)$$

This dependence of the stiffness on the applied DC potential is the basis of electronic tuning in the $M^2 - TFG$ and is revisited in Chapter 5.

The techniques used to model micromechanical resonators can also be used to model microgyroscopes. For system simulation using circuit simulators such as SPICE, the above ODE's can be modeled in the electrical domain as equivalent series-RLC circuits [23]. Fig 2.4 shows the RLC equivalent circuit used to model a resonant mode of the device. Since the microgyro is a capacitive sensor, the parallel feed-through capacitance C_{FT} , models the AC coupling path between the proof-mass and electrodes. The series RLC path models the sensor motional current, i.e., the current due to proof-mass motion.

The R , L and C are referred to as the *motional* resistance, inductance and capacitance, respectively. The $M^2 - TFG$ uses comb-drive electrodes for actuating the drive mode, while parallel plate electrodes are used for sensing proof-mass motion along the y -axis. Hence, expressions for the equivalent motional elements along these axes differ slightly. Table 2.2 summarizes the expressions for the drive and sense motional elements.

For behavioural modeling of the entire system, a SIMULINK model of the

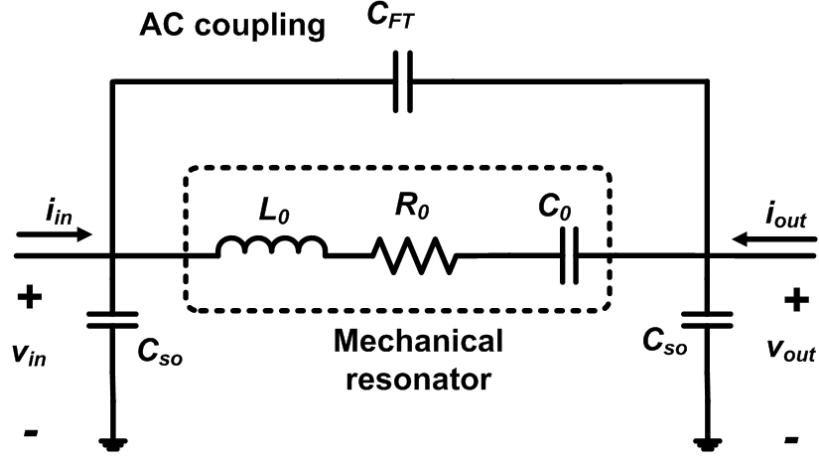


Figure 2.4: Equivalent RLC circuit representation of a micromechanical resonator.

Table 2.2: Expressions and approximate values for equivalent RLC parameters of the sensor used in this work.

Parameter	Comb Drive	Parallel Plate Sense
R	$\frac{\omega_o M g^2}{Q(\epsilon_o N h V_P)^2}$	$\frac{\omega_o M d_{so}^4}{Q(\epsilon_o l_e h V_P)^2}$
L	$\frac{M g^2}{(\epsilon_o N h V_P)^2}$	$\frac{M d_{so}^4}{(\epsilon_o l_e h V_P)^2}$
C	$\frac{(\epsilon_o N h V_P)^2}{g^2 \omega^2 M}$	$\frac{(\epsilon_o l_e h V_P)^2 d_{so}^2}{\omega_o^2 M d_{so}^3 - 2 \epsilon_o l_e h V_P^2}$

microgyrocope was developed, which allows both, frequency domain (s-domain) analysis as well as time domain analysis. The complete SIMULINK model is discussed in Appendix B.

However, for purposes of circuit simulations, the above equivalent RLC models are more suitable. Recently, significant progress has been made in modeling micromechanical structures using hardware description languages (HDL) such as AHDL and Verilog-A. In such models, it is possible to use the ODE's of Eq.(2.2) and Eq.(2.6) directly and perform circuit simulation. The Verilog-A code used to model a time varying capacitance and the effects of electrostatic tuning are provided in Appendix B.

CHAPTER III

TRANSIMPEDANCE CAPACITIVE FRONT-ENDS

The first step in developing a MEMS based microsystem is to choose an appropriate front-end interface to convert the mechanical signals such as displacement and velocity into electrical quantities, i.e., voltages and currents. The choice of the interface topology depends significantly on the nature of the mechanical system at hand. This chapter addresses the challenges and trade-offs in choosing a suitable interface for inertial-grade microgyroscopes. Further, design guidelines for low-noise sensor front-ends are discussed and experimental verification provided.

3.1 Challenges in MEMS Interfacing

The minimum detectable rotation rate in the gyroscope depends on the noise floor of the system (sensor plus electronics) and is given by the $TNE\Omega$, Eq.(1.1). The objective of designing interface electronics for navigation grade gyroscopes is to ensure that the $ENE\Omega$ is less than the $MNE\Omega$, i.e., the circuit noise is not the limiting factor in system performance. Since a fixed DC potential (V_P) has been maintained across the sense gap (d_{so}), Coriolis-induced y -axis displacement of the proof-mass in response to input rotation Ω_Z changes the sense rest capacitance (C_{S0}), generating a motional current I_{SENSOR} , given by:

$$I_{SENSOR} = \frac{2V_P C_{S0} Q_{EFF} q_{drive}}{d_{so}} \Omega_Z \quad (3.1)$$

The $ENE\Omega$ of the microgyroscope depends on the minimum detectable capacitance (ΔC_{MIN}) of the sense channel interface electronics and the mechanical scale factor ($F/^\circ/hr$).

$$ENE\Omega = \frac{\Delta C_{MIN}}{\text{capacitive sensitivity}} \quad (3.2)$$

For a parallel plate capacitive transducer, ΔC_{MIN} is proportional to the input referred current noise of the interface electronics integrated over the bandwidth of interest, as:

$$\Delta C_{MIN} = \frac{I_{noise}\sqrt{BW}}{\omega_0 V_P} \quad (3.3)$$

While the use of high aspect ratio micromachining techniques such as HARPSS [24], lower the $ENE\Omega$, the focus of this chapter is on circuit techniques to reduce the total input referred current noise of the sensor electronics. The theoretical $MNE\Omega$ of the sensor used in this work is $0.5^\circ/hr/\sqrt{Hz}$, which means the electronic front-end must be able to detect a proof-mass displacement as small as 0.1\AA , or resolve a capacitance change of $0.02aF/\sqrt{Hz}$ at the sensor operating frequency ($\sim 15\text{kHz}$).

The drive resonant mode of the TFG can be modeled as a two-port series RLC circuit [25], [26]. As described in Chapter 2, the motional resistance ($R_{MOT-DRV}$) represents the transmission loss and is obtained by equating the mechanical energy dissipated per cycle to the electrical energy supplied by the sustaining sources. To achieve drive amplitudes of about $4 - 5\mu m$, the gap between adjacent combs must be at least $7\mu m$. This implies that the microgyroscope has a drive motional impedance of about $16M\Omega$ in vacuum.

High motional impedances require a large gain to be provided by the sustaining circuitry in an electromechanical oscillator loop. High motional impedance also implies that a higher AC drive voltage needs to be applied to the comb-drive electrodes to achieve a required displacement, thereby dissipating more power. Therefore, there is a need for circuits that can achieve large on-chip gains for capacitive detection with low power and area over-heads.

The TFG implemented in this work is fabricated using a bulk-micromachining

technology, which allows for the fabrication of MEMS structures with narrow capacitive gaps and large inertial mass [18]. The sensor is fabricated on a different substrate and is connected directly to the IC via wire-bonds, as shown in Fig 3.1.

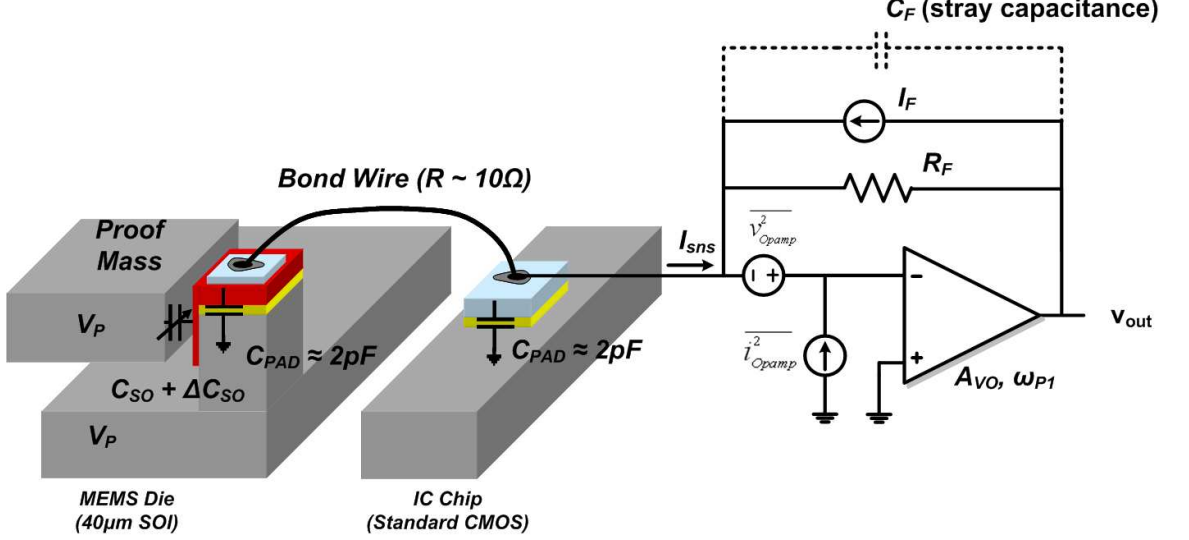


Figure 3.1: Schematic representation of a TIA (with noise sources) interfaced with the microgyroscope.

A two-chip implementation allows for the decoupling of the MEMS design and fabrication from the design of the interface electronics. Sensor performance can be improved considerably, unlike [14], by leveraging the benefits of high aspect-ratio mixed-mode processes [24]. In [14], it was necessary to surface micromachine the sensor element in order to make it compatible with the $3\mu m$ BiCMOS foundry used for the manufacture. Bulk-micromachining offers greater mass per unit area and is hence preferred to surface micromachining in gyroscope applications. In addition, standard CMOS processes can be used which significantly lowers cost and allows the electronics to be optimized for low power dissipation, speed, and reliability. However, the front-end analog interface must be strategically chosen to ensure that the sub-pico-ampere motional currents can be detected even in the presence of increased parasitics.

3.2 Overview of analog capacitive-MEMS front ends

Several techniques have been used in electronic front-ends to sense the small capacitive displacements in MEMS gyroscopes. Charge integration using switched capacitor front-ends with correlated double sampling were initially used for static MEMS accelerometers [27],[18], but have recently been used for microgyroscopes [28], [29]. Owing to the power budget associated with the switching and clock generation [30], these schemes are best suited for microgyroscopes with low operating frequency ($< 5kHz$). Further, the effects of the capacitive loading of these front-ends on the microgyroscope quality factor have not been studied. The use of such a front end necessitates that a switching voltage be applied to the mechanical structure, which results in significant feed-through and parasitic electrical coupling.

Ayazi et. al. used a unity gain, CMOS source follower amplifier as the front-end to detect capacitance changes in a vibrating polysilicon ring gyroscope [31]. The DC bias at the pick-off electrode was set using a minimum geometry diode. The noise injected by the diode at the input can significantly degrade performance [16]. Special techniques such as internal bootstrapping and feedback need to be applied to minimize the capacitance of the input transistor. The use of a unity gain buffer also does not allow independent control of the signal-to-noise ratio (SNR) of the electronic front-end.

Continuous time (CT) charge integrator front-ends are an attractive solution for sensing capacitive displacements in microgyroscopes ([14, 21]), because at typical operating frequencies, much larger AC impedances can be generated in a standard CMOS process using capacitors rather than resistors. Additionally, since these capacitors are not switched, there is no kT/C noise associated with them. However, the CT charge integrator requires the use of a large resistor to bias the input node. Various techniques, such as the use of controlled impedance FETs [14] and sub-threshold MOSFETS [21], have been proposed to implement these feed-back resistors.

The thermal noise of the feed-back resistor forms the dominant noise contributor of the front-end and determines overall performance.

Transimpedance amplifiers (TIAs) that use a resistor for CT sensing of the motional current are described in [14] and [21]. While the TIA is the interface architecture of choice for micromechanical resonator-based oscillators [26], its use as a low-noise front-end for capacitive Coriolis detection has not been fully explored.

3.3 *Why Transimpedance?*

In this work, a continuous time, programmable T-network TIA that provides state-of-the-art capacitive resolution is proposed as the interface for the MEMS microgyroscope. This section presents analyses and measurement results which validate that sub-atto-Farad capacitance changes, and hence degree-per-hour rate resolutions can be detected using a CMOS TIA front-end.

Figure 3.1 shows a schematic of a CT-TIA interfaced with a microgyroscope. Unlike previous studies ([14, 21]), in this work, the TIA has been optimized for noise and is used as the front-end in both the drive loop as well as for sub-atto Farad capacitive detection in the sense channel. Further, the gain of the TIA is variable, and the proof-mass is maintained at a constant DC potential unlike [21], [28] and [29]. In Figure 3.1, R_F is the feed-back resistance, C_F is the associated stray capacitance, and C_{TOT} is the lumped parasitic capacitance at the inverting terminal of the op-amp. C_{TOT} is composed of the electrode-to-substrate capacitance on the MEMS die ($C_{PAD-MEMS} = 1.5pF$), the interface IC pad capacitance ($C_{PAD-ASIC} = 1.5pF$), and the gate capacitance of the input differential pair transistors ($C_{GS-IN} = 0.5pF$) in the op-amp.

The high open loop DC gain of the op-amp ensures that the inverting terminal is a good virtual ground, while the shunt-shunt feedback presents low input impedance to the high-impedance sensor pick-off node. As a result, the signal path is relatively

insensitive to the total parasitic capacitance ($C_{TOT} = C_{PAD-MEMS} + C_{PAD-ASIC} + C_{GS-IN}$), preventing significant signal loss.

The low input impedance provided by the shunt-shunt feed-back helps reduce the loading that the sustaining electronics will have on the quality factor of the gyroscope drive mode. When locked into electromechanical oscillations, the loaded drive mode quality factor (Q_L) [26] is lower than its unloaded value (Q_{UL}):

$$Q_L = \frac{R_{MOT-DRV}}{R_{MOT-DRV} + R_{I-AMP} + R_{O-AMP}} Q_{UL} \quad (3.4)$$

where R_{I-AMP} and R_{O-AMP} are the input and output impedances seen by the sensor from the sustaining electronics. By applying the appropriate loading conditions at the input and the output for the TIA front-end, R_{I-AMP} can be approximated as:

$$R_{I-AMP} \approx \frac{R_F}{A_{VO}} \quad (3.5)$$

where A_{VO} is the open-loop DC gain of the core op-amp. Typical values for R_F in this case are in the $M\Omega$ range, and the DC gain is typically between 80 - 100dB. This implies that R_{I-AMP} can be as low as 10 – 100 Ω . Since the TIA front-end provides low R_{I-AMP} , there will be minimal Q-loading.

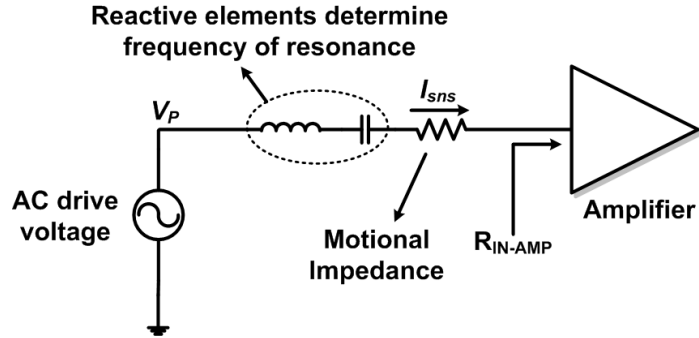


Figure 3.2: Series resonant oscillator showing impedances that load the quality factor.

The TIA interface allows the proof-masses to be maintained at a constant DC

potential unlike [28, 29, 30], where an AC capacitance bridge configuration is used. Applying a switching signal to the proof-masses [29] increases the amount of electronic coupling into the zero rate output of the gyroscope. By maintaining the proof-mass at a constant DC potential, any spurious signal coupling into the sensing electrodes is eliminated and the number of demodulation and filtering stages required are minimized, thereby lowering power consumption as compared to [30].

Fig 3.1 shows the main noise contributors in the transimpedance front-end, where v_{op-amp}^2 and i_{op-amp}^2 are the input referred voltage and current noise of the core op-amp, respectively, and $I_F = 4kBT/R_F$ represents the thermal noise power of the feedback resistor (R_F). Since the sensor output is a current proportional to proof-mass displacement, it is the total input referred current noise of the TIA front-end that ultimately determines the minimum detectable capacitance (Eq.(3.3)), and hence resolution of the microgyroscope. The equivalent input noise current (I_{N-TOT}) [32] for a TIA front-end, given by Eq.(3.6), includes effects of both the total parasitic capacitance seen at the input node (C_{TOT}), and the input resistance of the core amplifier, $R_{IN-op-amp}$.

$$\overline{i_{N-TOT}^2} = \overline{i_{op-amp}^2} + \frac{4k_B T}{R_F} + \overline{v_{op-amp}^2} \times \left(\frac{1}{R_F} + \frac{1}{R_{IN-op-amp}} + \omega C_{TOT} \right) \quad (3.6)$$

The noise contributions of i_{op-amp}^2 and $R_{IN-op-amp}$ are ignored for succinctness, reducing Eq.(3.6) to:

$$\overline{i_{N-TOT}^2} = \frac{4k_B T}{R_F} + \overline{v_{op-amp}^2} \times \left(\frac{1}{R_F^2} + \omega^2 C_{TOT} \right) \quad (3.7)$$

In a bandwidth of 10Hz about the sensor operating frequency, the equivalent input noise spectrum is assumed white, and thermal noise of the feedback resistor forms the dominant noise contributor. The electronic noise floor ($ENE\Omega$) for the $M^2 - TFG$ interfaced with a TIA is given by:

$$ENE\Omega = \frac{d_{SO}}{2V_P C_{SO} Q_{EFF} q_{Drive}} I_{N-TOT} \sqrt{BW} \quad (3.8)$$

The advantage of using a TIA front-end becomes clear when we consider the signal to noise ratio (SNR) of the front-end interfaced with a microgyroscope. A TIA with transimpedance (TZ) gain R_F yields an output signal voltage of $I_{SNS} \times R_F$ (for input motional current I_{SNS}), and output noise voltage of $\sqrt{4k_B T R_F}$. The amount of displacement current $i_{Brownian}$ due to the random Brownian motion of the proof-mass along the sense axis is derived by applying the equi-partition theorem [33] to the $M^2 - TFG$ at resonance and computing the noise displacement x_n [23, 31].

$$\overline{x_n^2} = \frac{4k_B T Q_{EFF}}{M\omega_0^3} \quad (3.9)$$

The sense resonant mode of the microgyroscope can be modeled as a second order system with an equivalent series RLC representation, very similar to that presented for the drive mode. The Brownian noise displacement is related to the mechanical motional resistance of the sense mode ($R_{MOT-SNS}$), and the equivalent Brownian noise current is derived:

$$\overline{i_{Brownian}^2} = \omega_0^2 V_P^2 \left(\frac{\delta C_{S0}}{\delta x} \right) \overline{x_n^2} = \frac{4k_B T}{R_{MOT-SNS}} \quad (3.10)$$

By using $I_{SNS} = i_{Brownian}$, the overall SNR is derived as:

$$SNR = \sqrt{\frac{R_F}{R_{MOT-SNS}}} \quad (3.11)$$

Therefore, increasing R_F improves the total SNR of an angular rate sensor. From Eq.(3.7), Eq.(3.8) and Eq.(3.11), it is evident that a large R_F for capacitive detection is beneficial not only for obtaining increased TZ gain, but also for better SNR and lower input current noise. Therefore, the objective of this work is to focus on strategies that yield large on-chip transimpedance.

In practice, the TZ for the case of an op-amp with finite DC gain (A_0), dominant pole p_1 (at frequency ω_{P1}) and input capacitance C_{TOT} , is given by Eq.(3.12). C_{TOT} and R_F introduce a second pole (p_2) at frequency $\omega_{P2} = 1/R_F C_{TOT}$ in the transfer function. Instead of rolling off close to the unity gain bandwidth (UGBW) of the op-amp (ω_{UGBW}), C_{TOT} causes the TZ gain to roll-off much sooner.

$$\frac{v_{out}}{i_{in}} = \frac{-R_F A_{V0}}{\left(1 + \frac{s}{\omega_{p1}}\right) \left(1 + \frac{s}{\omega_{p2}}\right)} \quad (3.12)$$

Further, since Eq.(3.12) is quadratic, the gain will peak before rolling off. The frequency at which gain peaking occurs, (ω_{PEAK}), is given by the geometric mean of the input pole and the $UGBW$ of the op-amp, and sets the effective bandwidth of the TIA.

$$\omega_{PEAK} = \sqrt{\omega_{P2} \omega_{UGBW}} \quad (3.13)$$

Gain peaking and the position of poles p_1 and p_2 affect the phase response of the TIA, placing restrictions on the maximum TZ that can be used in the microgyroscope. The phase characteristics of the sensor at resonance are key in distinguishing the rate signal from the quadrature error. When operating at matched-mode condition, there is a net 360° phase shift, due to the fact that there are 4 poles at the same frequency. To ensure that the precise phase relationship between the sensor quantities is not affected by the electronics, in this work, the TIA front-end has been designed to provide no more than 3.6° of phase shift (100x lower) at the sensor resonant frequency. The stability requirement, that the maximum phase shift at the TIA bandwidth be no more than 45° , is therefore automatically satisfied. Care has also been taken to ensure that the gain peaking frequency is higher than the sensor resonant frequency (ω_0) so that bandwidth is not limited.

3.4 *T-TIA's for capacitive detection*

Large transimpedance gains can be implemented on-chip in a number of ways [14, 21, 34, 35]. In [14] the transresistance was implemented using a controlled impedance FET. In [34], long MOSFETs biased in the linear regime using a constant voltage were used. MOS-bipolar pseudo-resistors are used in [35] for generating large resistances, but the maximum bandwidth obtained for the neural amplifier was 7.2kHz. The main disadvantage of these approaches is that real-time control of the transresistance gain is not possible. Variation of the transresistance is possible to some extent using the approach proposed in [14], but involves variation of the duty cycle used to switch the bypass-transistor controlled impedance FET pair. The strategy adopted in this work is to implement the feed-back resistor in a TIA using a T-network of resistors. The implemented T-network TIA provides both high gain and low-noise for sub-atto Farad capacitive detection in an area and power efficient manner. Further, it allows for simple analog control of the TZ without excessive phase shift.

3.4.1 Design considerations

Figure 3.3 shows the complete schematic of the implemented T-network TIA front-end, interfaced for capacitive detection. The equivalent transimpedance of the T-network TIA (R_{F-EQ}) is given by Eq.(3.14), where the voltage divider formed by R_2 and R_3 in the feed-back path provides an amplification of the equivalent TZ.

$$\frac{V_{out}}{I_{in}} \equiv R_{F-EQ} = R_1 \left(1 + \frac{R_2}{R_3} \right) + R_2 \quad (3.14)$$

The primary advantage of using the T-network is that it reduces the resistance levels to be placed on-chip, making on-chip integration tractable. In this work, R_1 is implemented as a long MOS transistor operating in the triode or deep-triode regions, and R_2 and R_3 were on-chip poly-resistors. The MOSFET adds a degree of gain control to the transimpedance, which can be used for temperature compensation or

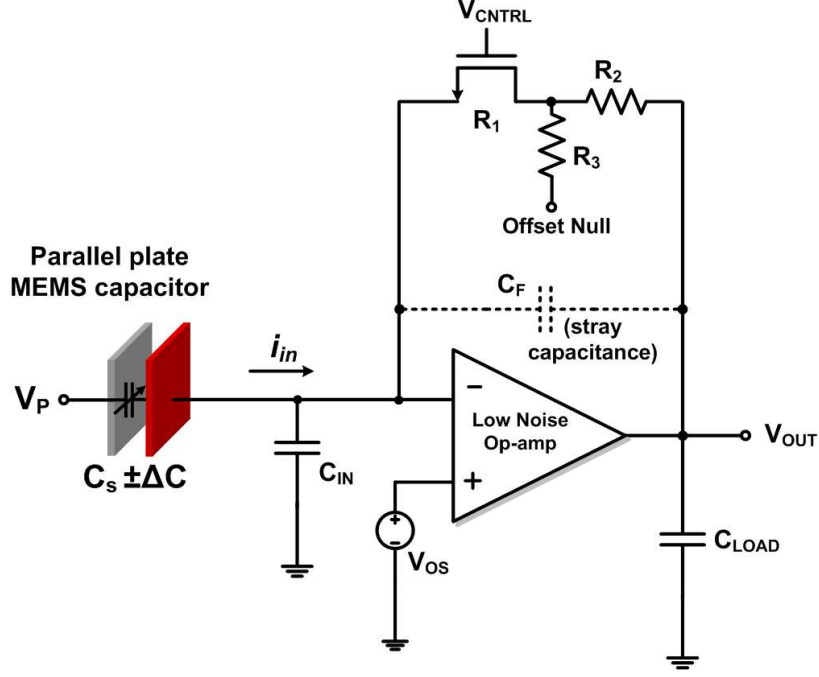


Figure 3.3: Schematic of the T-network TIA interfaced for capacitive detection.

for automatic level control applications. Further, the effects of the op-amp input referred DC offset (V_{OS}), can be nulled by applying an appropriate correction voltage to R_3 , i.e., at the base of the Tee . The resistances are designed such that $R_1 \gg R_2$ and R_3 . From Eq.(3.14) it might seem that arbitrarily high TZ can be obtained by increasing the R_2/R_3 ratio. However, in practice, the choice of this ratio is limited by bandwidth, noise, offset and stability trade-offs.

For the case of the T-network TIA interfaced to a capacitive sensor, the SNR of the front-end degrades by a factor of $\sqrt{(1 + R_2/R_3)}$, as given by Eq.(3.15), which places a limit on the maximum TZ that can be used in the front-end.

$$SNR = \sqrt{\frac{R_{F-EQ}}{R_{MOT-SNS} (1 + R_2/R_3)}} \quad (3.15)$$

The SNR degradation can be explained better by analyzing the noise gain of the T-network TIA (A_{NE-T}). While the noise gain might not limit the absolute value of the input referred current noise, it will impact the subsequent signal processing

stages. The noise gain of the T-network TIA is given by:

$$A_{NE-T} = (1 + R_2/R_3) \frac{1 + sR_1(C_{TOT} + C_F)}{1 + sR_{F-EQ}C_F} \quad (3.16)$$

By appropriately sizing the resistor ratio R_2/R_3 , it is possible to ensure $R_{F-EQ}C_F \approx R_1(C_{TOT} + C_F)$, thereby ensuring that the zero and pole cancel [36], yielding a constant value for the noise gain ($\approx 1 + R_2/R_3$). The relationship to prevent excessive noise increase due to the T-network's amplification of the op-amp's voltage noise is therefore given by:

$$\frac{R_2}{R_3} \leq \frac{C_{TOT}}{C_F} \quad (3.17)$$

C_{TOT} for the two-chip solution varies between 2 - 5pF. The stray feed-thorough capacitance (C_F) between the input and output is typically around 100 - 200fF. An R_2/R_3 ratio of 2 was therefore chosen as it allowed for sufficient amplification of the TZ gain without excessively increasing the noise gain. In TIA's, a shunt capacitance is usually placed in parallel with R_F to alleviate gain peaking considerations. The use of a feed-back Tee allows the increase of this capacitance to values that are less sensitive to parasitic effects [36].

DC offset restricts the maximum output signal swing, thereby determining the upper limit of the dynamic range. The expression for the output DC voltage due to finite offset (V_{OS}) for a T-network TIA interfaced directly with a capacitive sensor is given by Eq.(3.18). Interestingly, this is the value of the noise gain at DC. Optimizing the R_2/R_3 ratio for noise gain automatically minimizes effects of DC offset.

$$V_O = (1 + R_2/R_3) V_{OS} \quad (3.18)$$

3.4.1.1 Note on Noise Gain of a TIA

Noise gain is a term that is frequently used in circuits that need to sense small levels of currents or charge. The traditional application has been photonics, optical detectors as well as microwave/ millimeter wave communications and radar. Noise gain has been defined [37] as the reciprocal of the attenuation between the output of the op-amp to the input (via the feed-back network). Fig 3.4 summarizes the noise gain

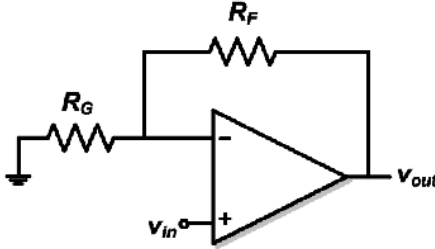
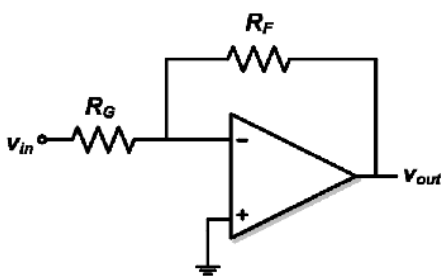
	Inverting Amplifier	Non-inverting Amplifier
		
Signal Gain	$-R_F/R_G$	$1+R_F/R_G$
Noise Gain	$1+R_F/R_G$	$1+R_F/R_G$

Figure 3.4: Summary of amplifier configurations with expressions for signal gain and noise gain.

as well as the signal gains for two commonly used amplifier configurations [38]. By convention, it is assumed that the input noise source is placed at the non-inverting terminal of the op-amp, similar to what is done in the case of input referred DC offset.

Next the noise gain expressions for a TIA is derived, and then the derivation is extended to the T-network TIA used in this work.

For the simple TIA shown in Fig 3.5(a), we can calculate the expressions for Z_F and Z_{IN} and thereby compute the noise gain as shown in Eq.(3.19).

$$A_{NE} = 1 + \frac{Z_F}{Z_{IN}} = \frac{1 + sR_F(C_{TOT} + C_F)}{1 + sR_FC_F} \quad (3.19)$$

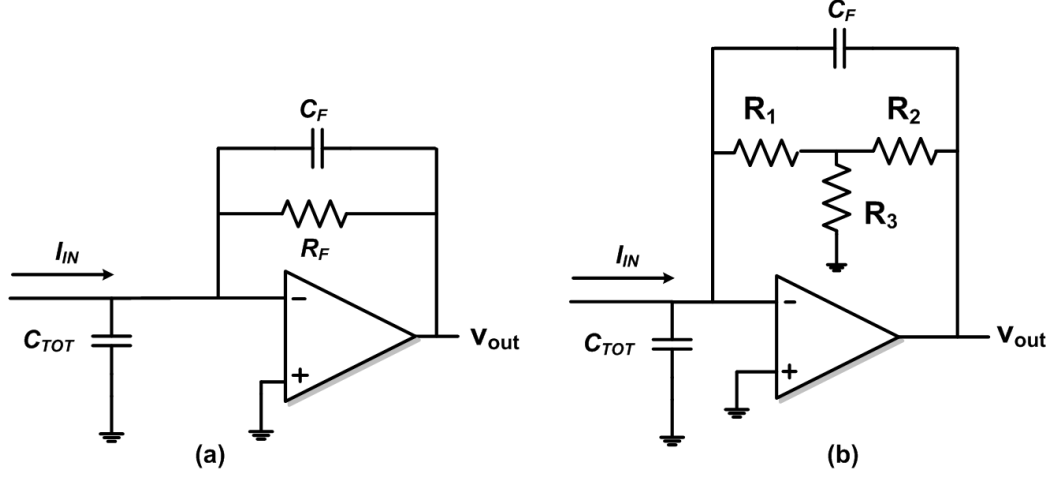


Figure 3.5: Schematic of (a) simple TIA and (b) T-network TIA with the relevant components for noise gain calculations.

The expression for the noise gain of the T-network TIA of Fig 3.5(b) is given by Eq.(3.16), and can be derived in a similar fashion to the previous case.

The values of the TZ gain and the noise gain are plotted for comparison in Fig 3.6. In both cases, the core op-amp is modeled to have a UGBW of about 2MHz and DC gain of 80dB. The values used for the T-network TIA are $R_1 = 0.5M\Omega$, $R_2 = 10k\Omega$ and $R_3 = 5k\Omega$. As seen in the upper graph, the equivalent transimpedance, R_{F-EQ} , is about $1.5M\Omega$ as given by Eq.(3.14).

The lower graph plots the noise gain for a simple TIA (Eq.(3.19)), with a single $1.5M\Omega$ resistance to provide the TZ gain. At low frequencies, the noise gain is 1. Both the simulations used a C_F of 500fF and a C_{TOT} of 3pF respectively. Also plotted on the lower graph is the noise gain of the T-network TIA (Eq.(3.16)) which has the same effective transimpedance. The low frequency noise gain of the configuration is now approximately 3 ($= 1 + R_2/R_3$).

At higher frequencies, both cases have the similar noise gains. This is because the noise gain is determined by the ratio of C_F and C_{TOT} . However, from an interfacing perspective, it is important to see where the noise gain begins to increase, and how any

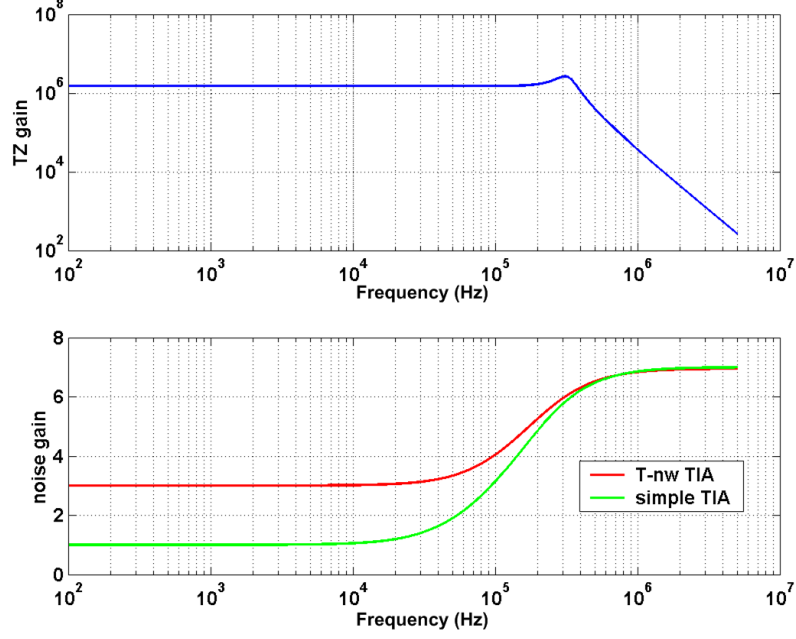


Figure 3.6: Simulation results showing transimpedance gain of the T-network TIA (top) and comparison of noise gain for simple and T-TIA configurations (bottom).

such increase can be mitigated in the frequency band of interest. For the T-network TIA case, as explained earlier, this is achieved by optimizing the R_2/R_3 ratio.

The analysis of noise gain follows exactly the same procedure as we do for offset - so think of calculation of noise gain as finding the response of the circuit to offset over a range of frequencies. Therefore, as expected, the noise gain expression reduces to the expression for the output referred DC offset, Eq.(3.18).

3.4.2 Low-noise CMOS Op-amp

A two stage Miller-compensated op-amp inherently has lower noise than a folded cascode OTA and was therefore chosen as the core amplifier. Figure 3.7 shows a schematic of the noise optimized op-amp, which is biased with a $1\mu A$ bias current generated by a constant transconductance bias circuit.

Transistors M_1 , M_2 , M_3 and M_4 are the primary noise contributors [32]. To minimize the input-referred flicker noise of the designed OTA, the PMOS input

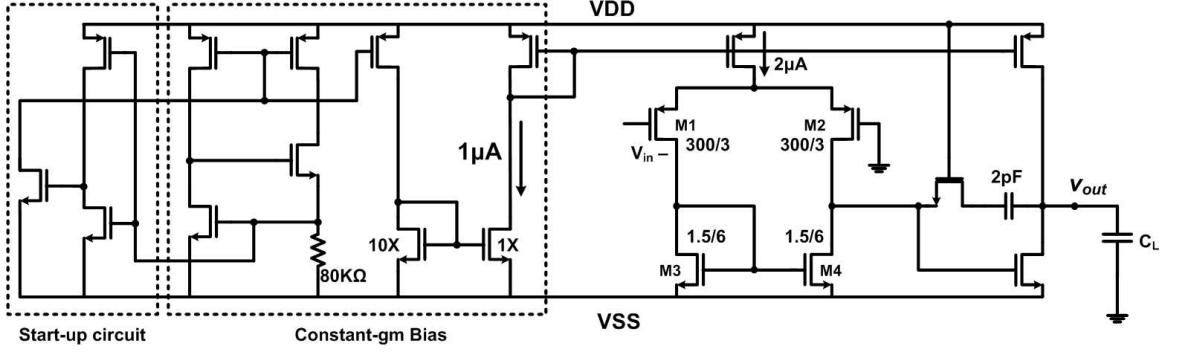


Figure 3.7: Schematic of the low noise op-amp used for in the T-TIA.

transistors (M_1 , M_2) are sized to be $300\mu\text{m}/3\mu\text{m}$. The transconductance of the input transistors is also designed to be large enough to avoid noise contributions of other transistors. When biased with a current of $1\mu\text{A}$, their transconductance ($g_{m1} = g_{m2}$) is calculated to be $84\mu\text{S}$ for the $0.5\mu\text{m}$ process. The NMOS load transistors (M_3 , M_4) are designed to have a W/L ratio of $1.5\mu\text{m}/6\mu\text{m}$ to ensure that their thermal noise contribution is minimized. The g_m of these transistors ($g_{m3} = g_{m4}$) is calculated to be $7.48\mu\text{S}$. The equivalent thermal noise floor of the core OTA is calculated to be about $17\text{nV}/\sqrt{\text{Hz}}$. Reliable flicker noise parameters (K_{F-PMOS} and K_{F-NMOS}) are not available for the process, but SPICE simulations performed with $K_{F-PMOS} \approx 5 \times 10^{-27}$ and $K_{F-NMOS} \approx 10^{-26}$ yielded a flicker noise corner frequency between 1 to 10kHz. Despite careful layout techniques and optimizing the core-amplifier to minimize systematic offset, the amplifier recorded a measured input referred offset of about 2mV . Table 3.1 summarizes the measured characteristics of the op-amp.

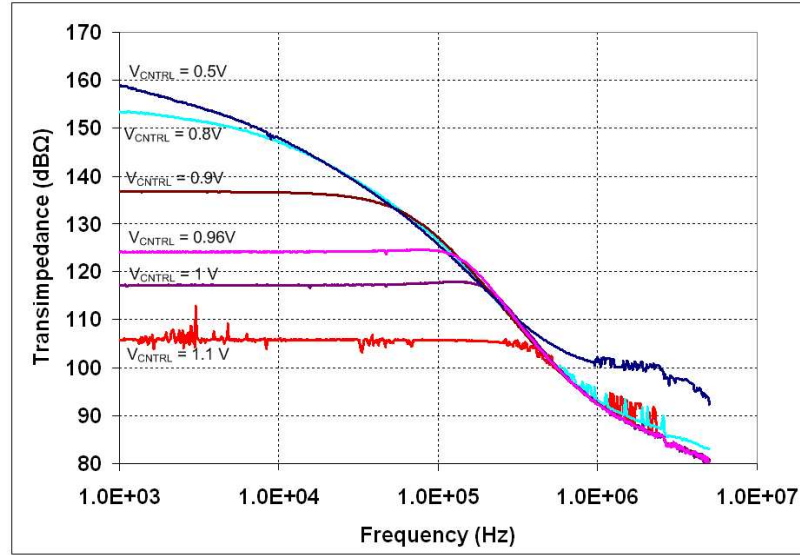
3.5 Measured Results of CMOS T-TIA

To measure the transimpedance characteristics, the microgyroscope was replaced with an external resistor that had roughly the same value as the motional resistance along the sense axis ($\approx 1\text{M}\Omega$). A voltage signal was applied to this $1\text{M}\Omega$ resistor

Table 3.1: Summary of measured op-amp parameters.

Parameter	Measured Value
DC gain	$> 100dB$
UGBW	$1.9MHz$
Thermal Noise Floor	$17nV/\sqrt{Hz}$
Flicker Noise corner frequency	$1 - 10kHz$
Max. Voltage swing at output	$2V_{PP}$
Power Dissipation	$400\mu W$
Power Supply	$\pm 1.5V$

which was connected in series with the TIA, and the gain was characterized using an Agilent 4395A network analyzer. The input of the TIA saw exactly the same input capacitance (C_{TOT}) as it would in the case of interfacing with the gyroscope. The transimpedance gain, plotted in Figure 3.8, was characterized for different values of gate control voltage (V_{CTRL}).

**Figure 3.8:** Transimpedance gain characterization of the T-TIA.

At $10kHz$, the TZ gain can be varied between $0.2M\Omega$ to $22M\Omega$ by varying the gate control voltage of the MOS resistor in the feed-back T. A transimpedance as large as $25M\Omega$ has been implemented on-chip, in a fraction of the area consumed otherwise. Optimizing the R_2/R_3 ratio has ensured that there is no gain peaking at

the frequencies of interest, as evident from Figure 3.8.

In reality, it is never possible to directly measure the input referred noise of a circuit. The total output noise of the T-network TIA was measured using the Agilent 4395A spectrum analyzer for different values of V_{CTRL} . The noise measurement set-up was similar to the one used to characterize the gain. For noise measurement, the $1M\Omega$ series resistor was replaced by a capacitor ($0.1pF$) that has roughly the same value as the total sensor rest capacitance. This capacitance prevents any TIA noise from shunting to ground. The measured output voltage noise is divided by the transimpedance measured from Figure 3.8 to yield the total input referred current noise of the TIA. Figure 3.9 shows the measured total input referred current noise of the T-network TIA for different values of transimpedance.

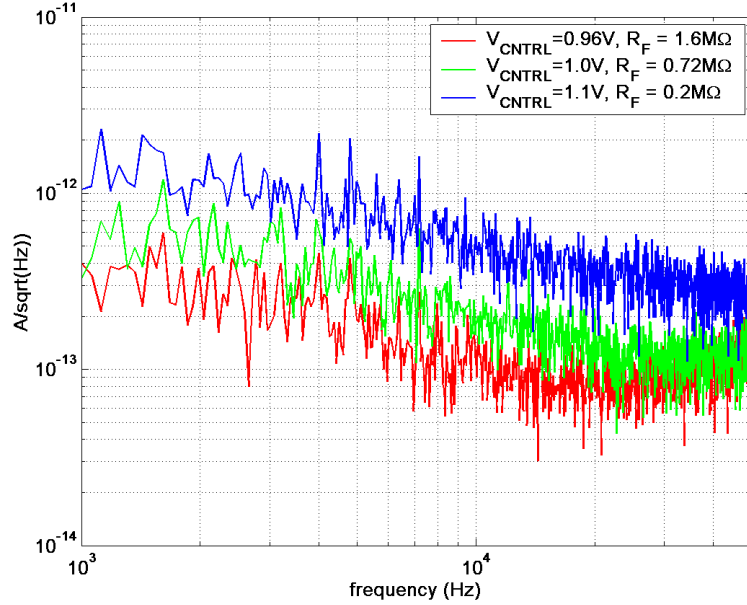


Figure 3.9: Measured input-referred current noise for the front-end T-TIA as a function of R_F .

It is clear from Figure 3.9 that, with increasing R_F , the current noise floor decreases, as predicted by Eq.(3.7). Therefore, a larger R_F lends to a lower noise floor, and hence smaller minimum detectable capacitance. In the region between 1 -

10 kHz, flicker noise is still significant, and accounts for the $1/f$ characteristic. The noise gain peaking due to the effect of the capacitance at the input node (C_{TOT}) is clearly visible from the plot. However, this noise gain peaking occurs beyond the sensor operating range (10 - 20kHz), and there is a minimum in the noise floor for the case of $R_F = 1.6M\Omega$ within the sensor operating range. This validates the claim that optimally sizing the R_2/R_3 ratio is effective in preventing excessive noise gain for the microgyroscope with sense motional impedance of $1 - 2M\Omega$.

When interfacing CMOS front-ends with high-Q narrow-band resonant MEMS sensors, the spot noise of the interface at the sensor resonant frequency determines the minimum detectable capacitance. At $15kHz$, the T-network TIA with a V_{CTRL} of $0.96V$ has a TZ gain of $1.6M\Omega$ and an input referred current noise of $88fA/\sqrt{Hz}$. The input referred current noise value corresponds to a capacitive resolution of $0.02aF/\sqrt{Hz}$ at $15kHz$ ($V_P = 40V$). This capacitive resolution is an order of magnitude better than that reported for the CT integrator of [34] and of the same order as the transcapacitance amplifier of [14]. While this resolution is comparable to the capacitive resolution of the chopper stabilized front-end interface of [30], it has been attained without any power consuming switching, and does not require any clock generation.

Figure 3.10 shows the measured TZ gain and phase characteristics for the case of $R_F = 1.6M\Omega$ (i.e. $V_{CTRL} = 0.96V$). At the sensor operating frequency, the maximum phase deviation is found to be 3.9° . The measured phase shift is close to the target value of 3.6° , validating the claim that the front-end T-network TIA provides the large gain and low noise, without adversely affecting the phase relationship between the sensor signals.

Figure 3.11 shows the measured output voltage noise of the T-network TIA for the case of $R_F = 1.6M\Omega$ ($V_{CTRL} = 0.96V$), as well as the measured output voltage noise of the core-amplifier. The thermal noise floor of the amplifier is measured to be about

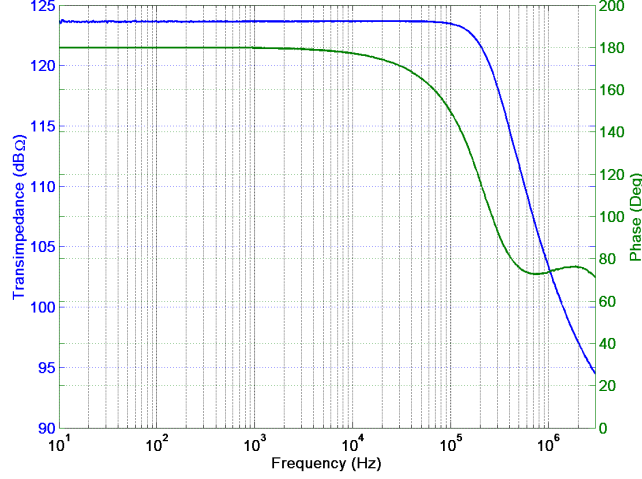


Figure 3.10: Measured transimpedance gain and phase relationship for the T-TIA with a transimpedance gain of $1.6M\Omega$.

$25nV/\sqrt{Hz}$, which is in excellent agreement with the theoretical value of $17nV/\sqrt{Hz}$ calculated earlier. Also, it is evident from the plot of the measured output noise of the amplifier that the flicker noise corner is between 1 - 10kHz.

The maximum dynamic range provided by the front-end T-network TIA for sensing is therefore of interest. The maximum dynamic range is defined in [32] as follows:

$$DR_{MAX} = \frac{Max. output signal}{Noise floor \times Bandwidth} \quad (3.20)$$

From Figure 3.11, the measured output spot voltage noise of the T-network TIA at $10kHz$ is about $250nV/\sqrt{Hz}$, which is slightly higher than the thermal noise from an ideal $1.6M\Omega$ resistor. This must be expected because of the noise gain of the T-network. This noise is integrated over a bandwidth of $10Hz$, and is used to determine the lower bound of the dynamic range.

While the noise floor determines the lower end of the front-end dynamic range, the upper limit is determined by the maximum output swing of the T-network TIA. The DC offset limits the output swing, thereby determining the maximum linear range

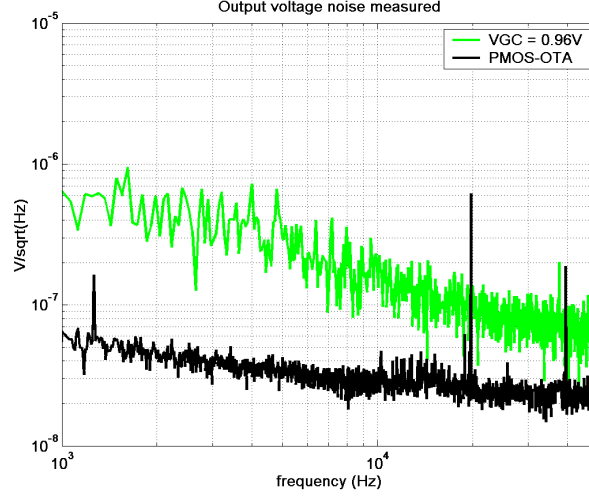


Figure 3.11: Measured output voltage noise of the core amplifier and the T-network TIA for $R_F = 1.6M\Omega$.

of the front-end interface. In order to find the maximum (non-distorted) signal-to-noise ratio, i.e., signal-to-(noise + distortion) ratio ($SNDR$) for the circuit, the input voltage level was swept upwards until the output signal was distorted. The maximum linear output swing of the TIA with TZ gain of $1.6M\Omega$ at a frequency of $10kHz$ is limited to about $0.4V_{RMS}$, as shown in Figure 3.12. Beyond this level, the nonlinearity in the output exceeds 2%, which is unacceptable. The distortion in carrier amplitude translates to phase inaccuracies, and hence it will no longer be possible to distinguish the Coriolis signal from the quadrature error. Therefore, this level forms the upper bound of the maximum usable dynamic range (DR_{MAX}). The maximum dynamic range is computed for a $10Hz$ bandwidth, and is found to be at least $104dB$ at the sensor resonant frequency.

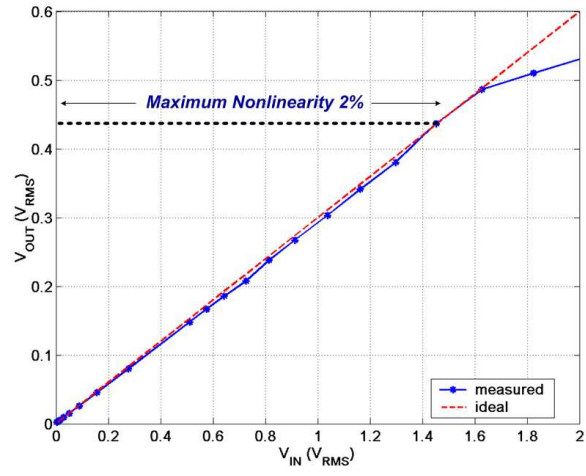


Figure 3.12: Measured SNR plot of the T-TIA for $R_F = 1.6M\Omega$ at 10kHz.

CHAPTER IV

DRIVE AND SENSE ELECTRONICS

This chapter discusses two implementations for the drive loop to set up the reference oscillations. The amplitude of the drive oscillations is a critical parameter that determines the performance of the gyro, and is discussed in detail. Finally, the implementation of an analog sense channel using CMOS synchronous demodulators for open-loop rate sensing is presented.

4.1 Drive Resonant Oscillator

The first implementation of the drive loop presented is similar to the approach used for micromechanical resonator oscillators [23]. Here the reference vibrations along the x -axis are set up and sustained by placing the TFG in an electromechanical oscillator, where the drive mechanical resonance is the frequency determining element. Proof-mass movement is detected by using the comb electrodes that are located symmetrically on either side of each proof-mass. It is essential that the proof-masses are driven anti-phase with respect to each other to retain the differential nature of the sensor.

The T-network TIA described in Chapter 3 is used as the front-end to convert the drive motional current into a voltage. A buffer is used to provide any necessary amplification and to ensure a loop phase shift of 0° . The signal is then applied back to the central electrode. The oscillations are started by the mechanical (Brownian) and electronic noise in the system. An automatic level control (ALC) is used to start up and subsequently control the amplitude of vibration. At power-up, the ALC ensures a start-up loop gain of greater than 1. An off-chip PLL [39] locks on to the drive signal

and is used to provide carefully phased signals for subsequent signal processing¹. The complete series resonant electromechanical drive loop and ALC interfaced with the TFG is shown in Figure 4.1.

The ALC circuit is based on the architecture presented in [40], and is used to keep q_{Drive} constant, thereby preventing false rate outputs. In the current implementation, all the blocks were implemented on-chip in a $0.5\mu m$ CMOS process. Since this CMOS process did not include lateral or vertical BJT's in the design library, an alternate method was used to implement the diodes in the rectifier. The diodes in the ALC were implemented using the source/drain-to-bulk junctions of a PMOS transistor. The ALC output voltage is passed through an off-chip low-pass ripple filter and used to control the gate of the MOS transistor in the front-end T-network TIA.

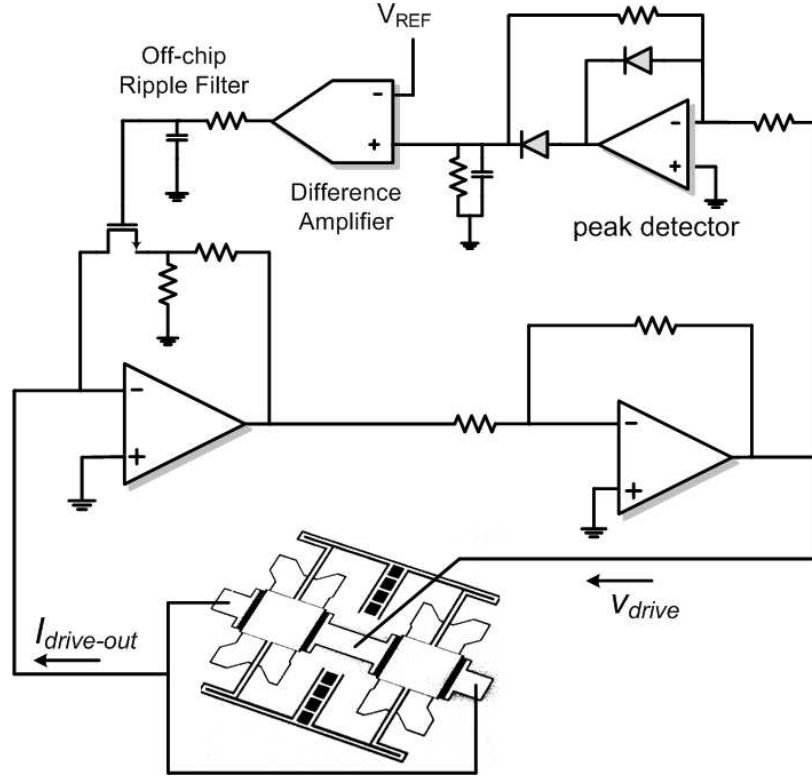


Figure 4.1: Schematic of the drive loop oscillator loop with the automatic level control circuit.

¹In this work, the PLL has not been integrated on the CMOS ASIC.

Figure 4.2 shows the buffered closed loop drive oscillation waveform and the spectrum of the signal when the drive loop was interfaced with a TFG². The high mechanical Q of the structure forms an excellent narrow-band filter at the mechanical resonant frequency, and therefore significantly alleviates the linearity requirements on the driving voltage output by the IC. While commercial gyroscopes use drive voltages in the order of $12V_{PP}$ [14], the high drive quality factor of this TFG allows for drive voltages as low as $200mV_{PP}$. The use of low-voltage drive signals significantly lowers power dissipation and precludes the need for high voltage transistors for charge-pumps and off-chip capacitors as in [14].

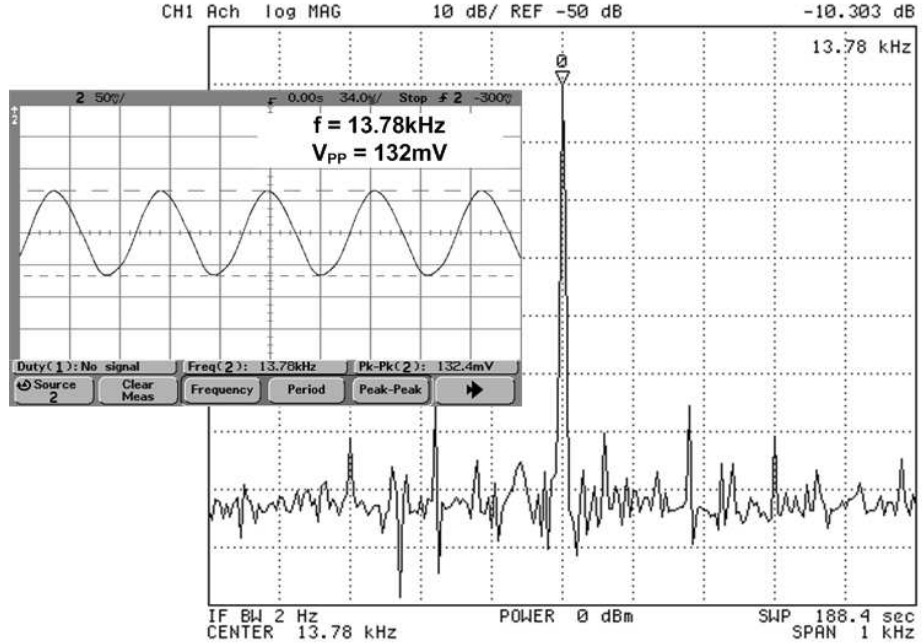


Figure 4.2: Drive oscillator spectrum and buffered output waveform.

4.2 PLL-based drive oscillator

While the electromechanical series resonant oscillator approach is attractive from a power dissipation point of view, there are certain limitations of the approach.

²This was a second sensor with a drive resonant frequency equal to 13.78kHz

As discussed in Chapter 3, the gap between adjacent combs must be increased to ensure larger drive amplitudes. A large drive-comb gap can lead to drive motional impedances as large as $20M\Omega$, and might require multiple cascaded stages of electronic amplification. In addition to increasing the overall power dissipation, cascading multiple stages greatly increases the chance of system instability due to the high gain and electromechanical impedances, thereby leading to spurious electronic oscillations.

The PLL that is used in the microsystem (Fig 2.3) to generate the signals for signal processing can also be used to excite and maintain the drive mode oscillations, unlike [21]. On start-up, the PLL locks on to the output of the front-end I-V converter, which is still implemented using the T-network TIA. The PLL used here is an off-chip HC4046 digital PLL [39] operated from a 3V supply to ensure compatibility with the $\pm 1.5V$ voltage rails of the CMOS circuitry. The output of the PLL, after down-conversion, is a rail-to-rail digital signal at the frequency of resonance. This digital output signal is then attenuated to achieve the desired voltage amplitude and used to drive the microgyroscope. The symmetric electrode configuration ensures that the PLL does not lock into the second in-plane spurious mode along the x -axis (i.e., in which the proof-masses vibrate in-phase). Fig 4.3 shows a schematic of the PLL-based drive oscillator loop and the oscilloscope waveforms of the 90° phase shifted signals.

The center frequency of the voltage controlled oscillator (VCO) in the PLL is set to be higher than the actual drive resonant frequency. A frequency divider consisting of digital latches is then used to down-convert the PLL center frequency to the sensor resonant frequency. A frequency division ratio of 4 is implemented by using two D flip-flops as shown in Fig 4.3 and serves three purposes:

- First, a division ratio of at least 4 is necessary to generate the 0° and 90° signals.
- Second, by placing the VCO center frequency much greater than the sensor resonant frequency, effects of VCO jitter on PLL dynamics and gyro sense channel signal processing are mitigated due to the down-conversion.

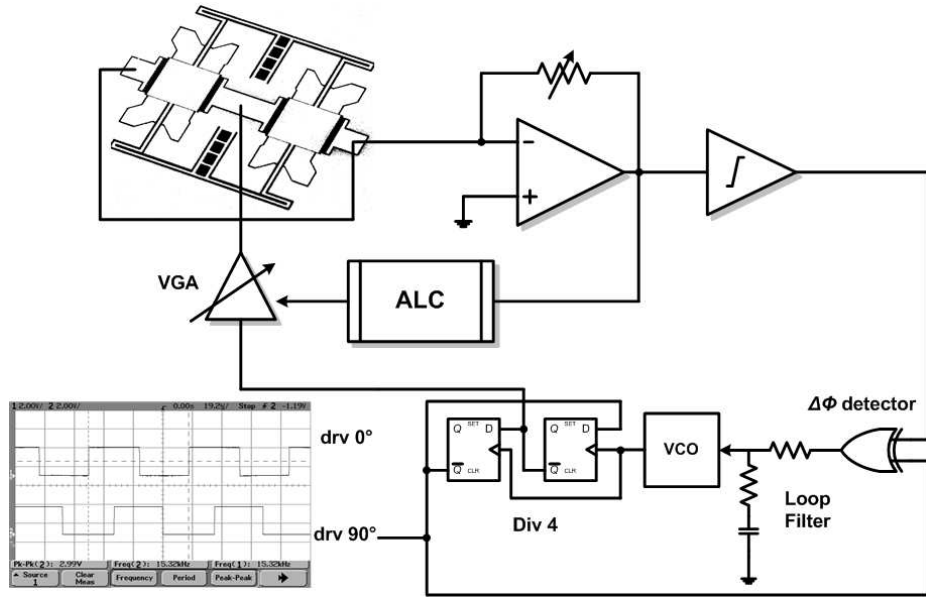


Figure 4.3: Block diagram of the PLL-based drive loop.

- Finally, a higher VCO frequency allows smaller reactive elements (L and C) to be placed on the PCB or on-chip, reducing system form-factor.

Fig 4.4 shows the attenuated square wave input signal to the gyroscope, and the sinusoidal output from the gyroscope at drive resonance. The glitches are due to electronic feed-through on the PCB. The characteristic 90° phase difference between input and output voltage waveforms is observed at electromechanical resonance.

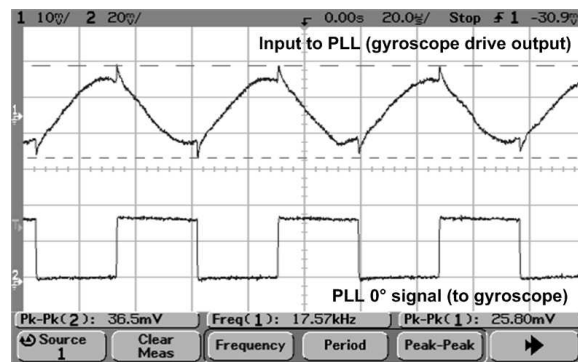


Figure 4.4: Voltage waveforms showing the input drive signal from the PLL and the output signal from the gyroscope.

Automatic level control can be performed using the same topology described in the micromechanical resonator approach. In the version of the systems implemented in this work, the drive amplitude level was set manually to allow flexibility in experimentation.

4.3 Measurement of drive amplitude

The amplitude of vibration of the proof-masses along the x -axis (q_{DRIVE}) is an important metric that determines the sensor Brownian noise floor (Eq.(1.2)) and Coriolis sensitivity (Eq.(1.5)). A reliable means of measuring the drive amplitude and characterizing its linearity are therefore critical when gyroscope performance targets navigation applications.

In a comb driven structure, the maximum achievable q_{DRIVE} is limited by lateral snapdown [20], and is proportional to the square of the gap between adjacent combs(g). Fig 4.5 shows a close-up of the drive combs and identifies key parameters. The maximum achievable drive amplitude, $q_{DRIVE-MAX}$, can be calculated as:

$$q_{DRIVE-MAX} = \frac{-\omega_0 + \sqrt{\omega_0^2 + 2(k_X/k_Y)g^2}}{2} \approx \frac{g}{\sqrt{2}} \quad (4.1)$$

where g is the gap between adjacent combs, ω_0 is the initial comb overlap, and k_X and k_Y are the mechanical stiffnesses along the drive(x) and sense(y)-axes respectively.

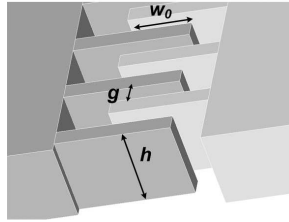


Figure 4.5: Schematic view of the x-axis drive combs with relevant dimensions.

The expression for the output motional current at resonance of the drive mode, is the same as that of the double ended tuning fork resonator described in [23], and

is given by:

$$i_{out-rms} = \frac{\partial C}{\partial x} \times V_P \dot{x} = \frac{\epsilon_0 N h V_P \dot{x}}{g} \quad (4.2)$$

Here \dot{x} is the velocity of the proof-mass displacement along the x -axis, N is the number of combs, h is the structural height, and V_P is the DC polarization voltage. Assuming sinusoidal oscillations of amplitude q_{DRIVE} , at frequency ω_0 , the magnitude of the maximum drive velocity is given by $\dot{x}_{MAX} = q_{DRIVE} \times \omega_0$. From the measured motional current at resonance, the value of q_{DRIVE} can therefore be calculated as:

$$q_{DRIVE-MAX} = \frac{i_{out-PP} g}{2\epsilon_0 N h V_P \omega_0} \quad (4.3)$$

where i_{out-PP} is the measured peak-to-peak value of the motional current.

The sensor is driven to oscillate using the PLL-based drive oscillator, and the variation of the drive amplitude with input excitation voltage is measured. The drive amplitude was computed from the measured output voltage waveform by de-embedding the effects of the 2pF parasitic capacitance present at the interface between the MEMS and the electronic front-end. Fig 4.6 shows the drive amplitude as a function of input peak-to-peak drive voltage.

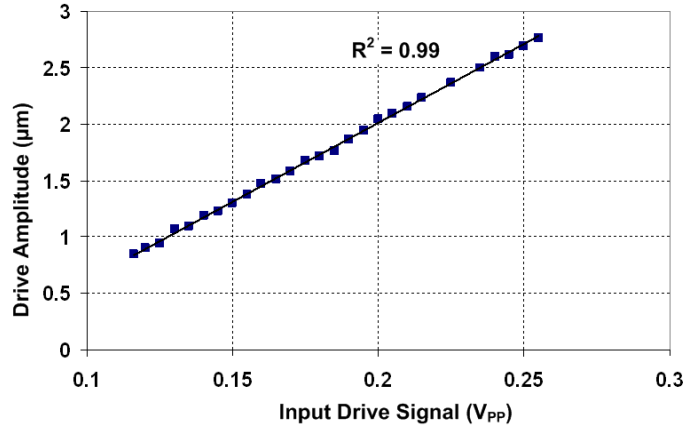


Figure 4.6: Measured variation of drive amplitude as a function of input drive signal.

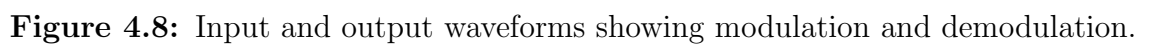
A least-squares curve fit shows that the drive amplitude varies linearly with increase in input drive voltage (Fig 4.6). Interestingly, the mechanical design of the sensor ensures that the zero rate output (ZRO) does not show a corresponding increase.

4.4 *Analog Sense Channel*

When subject to rotation about the z -axis, the proof-mass vibrates along the sense (y)-axis, and the amplitude of vibration is modulated by the applied rate signal. The sense channel detects this proof-mass displacement and extracts the amplitude modulated (AM) rate information. Proof-mass displacements, due to both Coriolis acceleration and quadrature error, take place at the sensor resonant frequency (ω_0). The only distinguishing characteristic between Coriolis and quadrature signals is that there exists a 90° phase difference between them. This phase difference arises due to the fact that quadrature error is proportional to the proof-mass position, while the Coriolis response is proportional to the proof-mass velocity along the driven axis. The rate and quadrature are distinguished by demodulating the sense output with the 0° and 90° signals from the PLL respectively. Therefore, the sense channel uses a phase sensitive synchronous I-Q demodulation scheme to extract the rotation rate, rather than a simple envelope detection scheme. Finally, the TFG electrode configuration shown allows for fully differential sensing topology, which automatically rejects linear acceleration as common-mode in the mechanical domain.

A CMOS Gilbert multiplier with $200k\Omega$ on-chip polysilicon load resistors is used for the multiplication. Figure 4.7 shows the mixer schematic and input and output test waveforms.

The output of the Gilbert multiplier is low pass filtered to yield an analog signal proportional to the rotation rate. The integrated, active 1^{st} order low pass filter uses a $1.5nF$ off-chip capacitor to set the cut-off frequency to 100Hz and has a low pass



gain of about 2. The rate signal from the two channels can be converted to a single ended signal using an off-chip instrumentation amplifier.

4.4.1 Rotation Response

The $M^2 - TFG$ was placed on an Ideal Aerosmith 1291BR rate table, and its scale factor was characterized as shown in Figure 4.9.

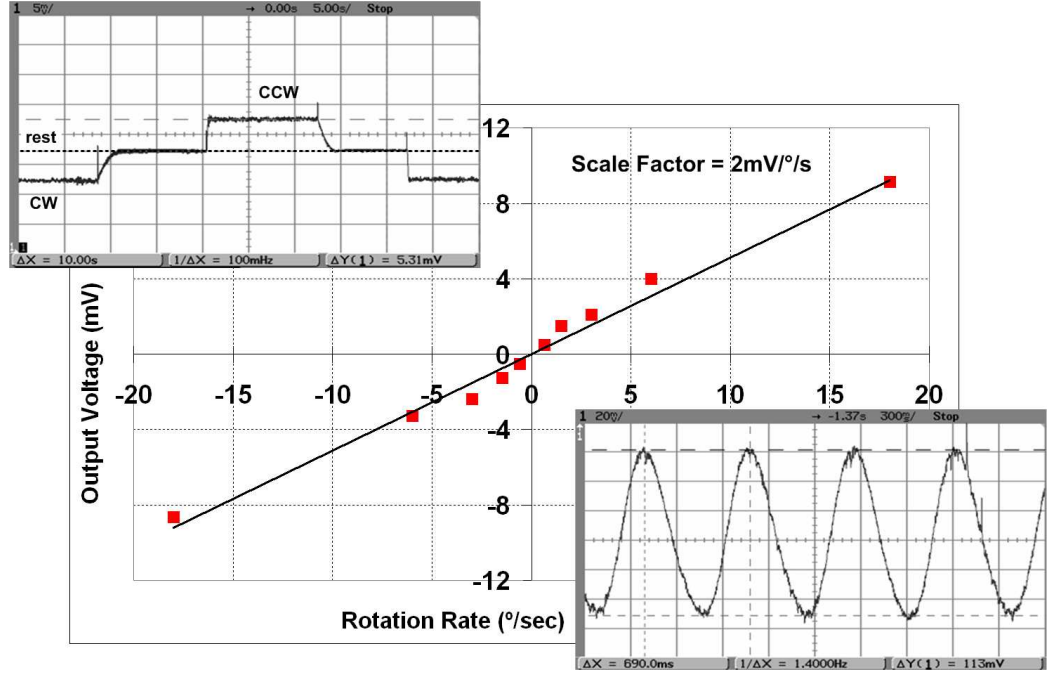


Figure 4.9: Rate response and scale factor of gyroscope.

The measured scale factor from one of the channels is $2mV/^\circ/sec$, with a maximum nonlinearity of 3% over the measured range. Nonlinearity in the sense channel signal processing chain arises due to the slight difference in the capacitive gaps on the MEMS structure, the nonlinearity of the front-end TIA and more significantly, the incomplete cancellation of the higher order harmonic terms as the Gilbert cell was operated in a single ended configuration. Figure 4.9 also shows the sensor response to a $1.5Hz$ sinusoidal input rotation as well as the response of the microgyroscope to both positive (CCW) and negative (CW) input step rotations.

4.5 Summary

The sense and drive loops are implemented in $0.5\mu\text{m}$ CMOS as shown in Fig 4.10. The ASIC measured $1.5\text{mm} \times 1.5\text{mm}$, and consumed 15mW from a $\pm 1.5\text{V}$ supply.

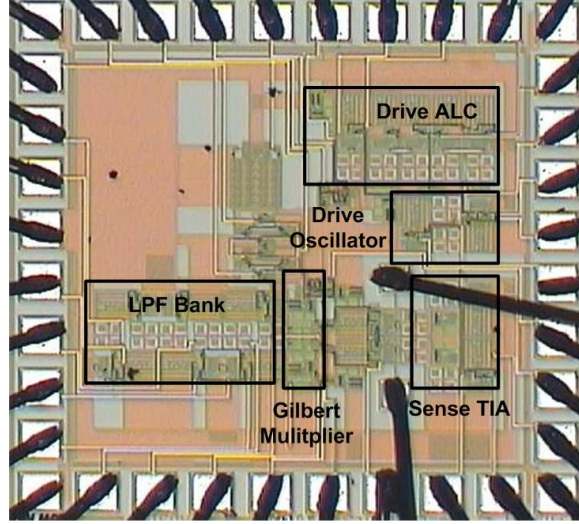


Figure 4.10: $0.5\mu\text{m}$ CMOS ASIC for gyroscope drive and sense channels.

Fig 4.11 shows the custom PCB that consists of the MEMS sensor and the CMOS interface IC. This PCB was placed in 1mTorr vacuum.

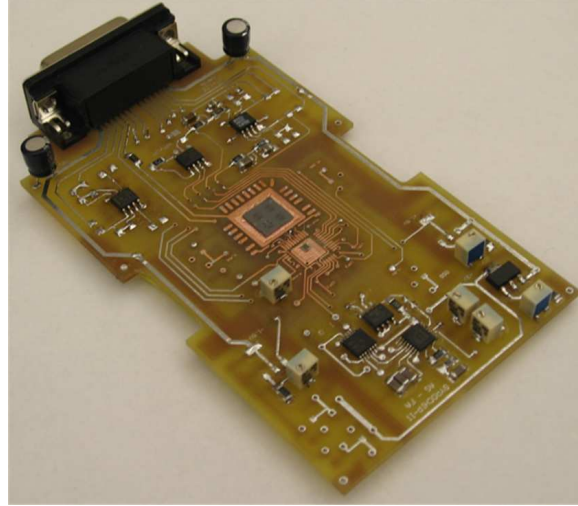


Figure 4.11: $0.5\mu\text{m}$ CMOS ASIC and MEMS die on custom PCB.

A summary of the sensor and IC parameters are listed in Table 4.1 below.

Table 4.1: Summary of key Sensor and drive/ sense ASIC parameters

Parameter	Measured Value
Sensor capacitive sensitivity	$80aF/\circ/s$
Amplitude of drive voltage applied	$130mV$
Range of minimum detectable ΔC (at 15kHz)	$0.02 - 2aF/\sqrt{Hz}$
Linear Dynamic Range of front-end of T-TIA	$104dB$
Rate sensitivity of Gyro + IC	$2mV/\circ/s$
Die Area	$2.25mm^2$
Total Power Consumption	$15mW$
Output voltage noise level at 10Hz	$15\mu V/\sqrt{Hz}$
Measured rate noise floor	$2.7^\circ/hr/\sqrt{Hz}$
Power Supply	$\pm 1.5V$

CHAPTER V

QUADRATURE ERROR AND MODE-MATCHING IN MICROGYROSCOPES

Micromachined structures suffer from fabrication induced imperfections that result in spatial misalignments as well as a deviation in mechanical resonant frequencies from the designed values. This chapter explores the origins of these errors and the impact they have on sensor performance. System solutions to compensate the effects of these errors are proposed and compared to the existing state-of-the-art.

5.1 Origins and Impact of Quadrature Error

Imbalances in the mechanical elements due to fabrication imperfections result in a significant error signal common to all CVG's [21]. Consider a single proof-mass that is free to move along the drive and sense axes as shown in Fig 5.1(a). Ideally, the motion of the proof-mass must be restricted to the x -axis when the drive mode is excited, and only to the y -axis when the sense mode is excited due to Coriolis acceleration. However, imbalances present in the mechanical structure cause the proof-mass to vibrate at an angle θ_Q from the actual x -axis as shown. This off-axis proof-mass displacement results in mechanical coupling of the drive resonator motion to the sensitive axis, and an oscillatory deflection that will be measured along the sense axis with the Coriolis induced deflections. This spurious mechanical coupling is termed *quadrature error*. Further, the mechanical coupling produces an output signal even in the absence of an input rotation, giving rise to what is often referred to as zero rate output (ZRO). In a shell-type microgyroscope, like the vibrating polysilicon ring [31] or the resonating star gyroscope [10], the spatial misalignment of the flexural

modes with respect to the 0° and 45° axes gives rise to quadrature error, as shown in Fig 5.1(b).

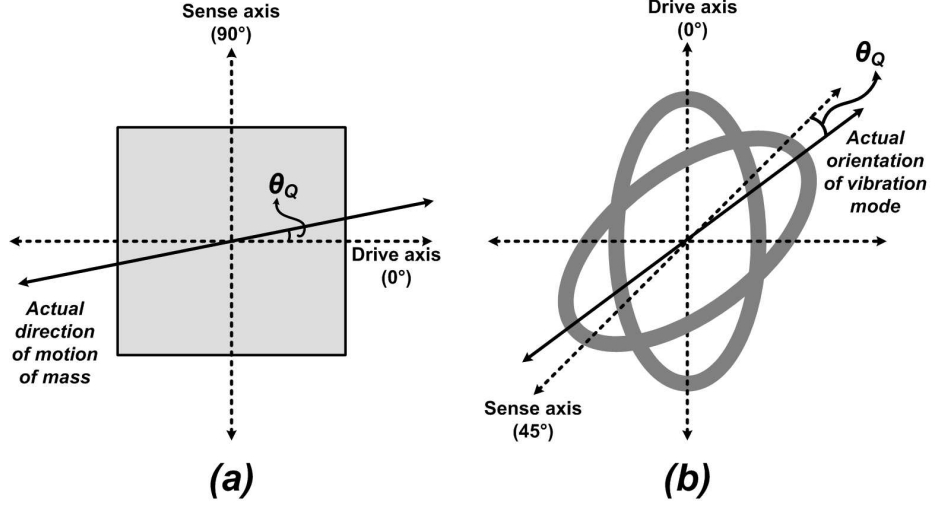


Figure 5.1: Sources of quadrature error in TFG (a) and a shell structure (b).

Consider the proof-mass of Fig 5.1(a) is oscillating sinusoidally along the drive axis with maximum drive displacement q_{drive} .

$$x_{drive}(t) = q_{drive} \sin(\omega_{drv} t) \quad (5.1)$$

The misalignment of the proof-mass by angle θ_Q results in a displacement component along the sense axis ($y_{quadrature}(t)$), given by:

$$y_{quadrature}(t) = \sin(\theta_Q) q_{drive} \sin(\omega_{drv} t) \approx \theta_Q q_{drive} \sin(\omega_{drv} t) \quad (5.2)$$

where the small angle approximation allows $\sin(\theta_Q) \approx \theta_Q$. However, the Coriolis acceleration of the proof-mass is given by $2\vec{v} \times \Omega_Z$, where \vec{v} is the proof-mass velocity along the drive axis and is given by $v_{drive}(t) = q_{drive} \omega_{drv} \cos(\omega_{drv} t)$. The Coriolis induced proof-mass displacement along the sense axis is therefore given by:

$$y_{Coriolis} = 2\Omega_Z(t) q_{drive} \omega_{drv} \cos(\omega_{drv} t) \quad (5.3)$$

Therefore, both the quadrature error and Coriolis deflection are amplitude modulated signals centered at the drive resonant frequency. The only distinguishing feature between the two signals is that they have a relative phase of 90° , hence the origins of the term quadrature error. This phase difference originates from the fact that the Coriolis acceleration is sensitive to proof-mass velocity along the drive axis, Eq.(5.3), while the quadrature error is proportional to the proof-mass position, Eq.(5.2), along the drive axis.

The above analysis also shows that the level of the quadrature signal is much greater than that of the rotation induced Coriolis signal. Dividing Eq.(5.2) by Eq.(5.3), the ratio of quadrature displacement to the Coriolis displacement is:

$$\frac{y_{quadrature}}{y_{Cor}} = \frac{\omega_{drv}\theta_Q}{2\Omega_Z} \quad (5.4)$$

This indicates that even a small angle θ_Q of misalignment can cause a significant amount of quadrature error that is much greater than the Coriolis induced displacement. Excessive quadrature error leads to saturation of the sense channel electronics, and therefore it must be compensated or nulled.

The impact of quadrature error on the microgyroscope system dynamics can be modeled effectively by adding cross-coupling coefficients in the 2-DOF spring stiffness matrix K_M [21].

$$\mathbf{K}_M = \begin{pmatrix} k_{xx} & k_{xy} \\ k_{yx} & k_{yy} \end{pmatrix} \quad (5.5)$$

where k_{xx} and k_{yy} are the mechanical spring stiffnesses along the x and y axes respectively. k_{xy} and k_{yx} are the cross-diagonal spring stiffness terms that model the quadrature induced mechanical coupling.

For this reason, reducing quadrature error is best achieved by ensuring that the spring matrix is diagonalized by the application of specific quadrature nulling

techniques. Further, these cross-diagonal terms cause the system to be a non-degenerate 2-DOF system, forming the single most important factor that precludes mode-matching.

5.2 *Quadrature Nulling*

Despite significant progress in the design and development of gyroscope structures with inherently low mechanical cross-talk [41], quadrature error still remains a significant issue. All CVG's use some form of quadrature nulling that involves electronic or mechanical compensation of the quadrature signal. However, quadrature nulling of any gyroscopic sensor depends significantly on the nature of the mechanical structure itself.

A number of techniques have been used to null quadrature error. Some of the earliest work involved trimming and bucking to control quadrature error [42, 43], but suffered from the fact that this did not track over temperature and life. Other techniques involved servo-mechanisms, whereby a force was applied to the mass so as to null any displacement of the proof-mass that is in phase with position [21]. Quadrature error in the polysilicon ring gyroscope [31] and the resonating star gyroscope [10] was nulled by the application of specific voltages at electrodes located at $\pm 22.5^\circ$, to allow a spatial rotation of the resonant modes until they are aligned along the respective axes. The Analog Devices gyroscope [14] uses a set of optimally designed levers to reduce quadrature error to less than 1ppm by improving the selectivity of the suspension flexures.

It is intuitive to think of quadrature error as a static/DC phenomenon. All of the above techniques reduce the quadrature by application of electrostatic forces that result in displacement or rotation of the mechanical elements. For a robust design, quadrature nulling must be repeatable and must be able to provide the required spatial reorientation of the mechanical structure over several batches of devices.

Previous designs of the TFG used in this work did not contain adequate electrodes for quadrature nulling, resulting in incomplete suppression of the error [44].

High Q devices are more susceptible to quadrature error. Due to the high Q's of the $M^2 - TFG$, any spurious displacement along the sense axis - due to quadrature or Coriolis - is amplified by the sense mode quality factor. One of the contributions of this work was to develop an electrode configuration for the TFG that would allow efficient and repeatable nulling of the quadrature error. The technique proposed uses rotational torques to rotate the proof-masses and thereby correct for any spatial misalignment. An illustration of the technique is shown in Fig 5.2. By applying the appropriate torques on each proof-mass, it is possible to rotate each of them clockwise (CW) or counter-clockwise (CCW), correcting misalignment of the drive axis and thereby suppressing the quadrature.

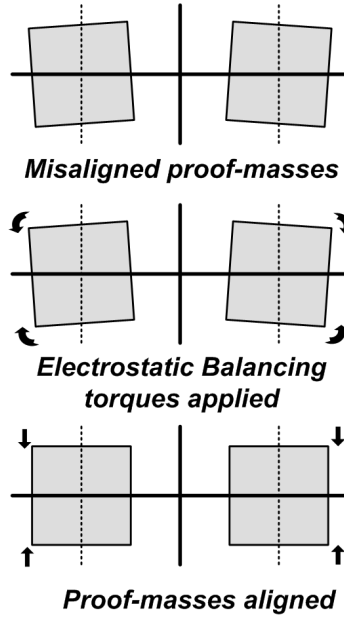


Figure 5.2: Conceptualization of quadrature nulling in the $M^2 - TFG$ by use of rotating torques.

Dedicated quadrature nulling electrodes were added to the TFG, two for each proof-mass, as shown in Fig 5.3. Two electrodes per proof-mass were found to be

sufficient for producing the required CW or CCW torque. Each electrode contains 4 parallel-plate fingers to apply an electrostatic force at the corner of the proof-mass.

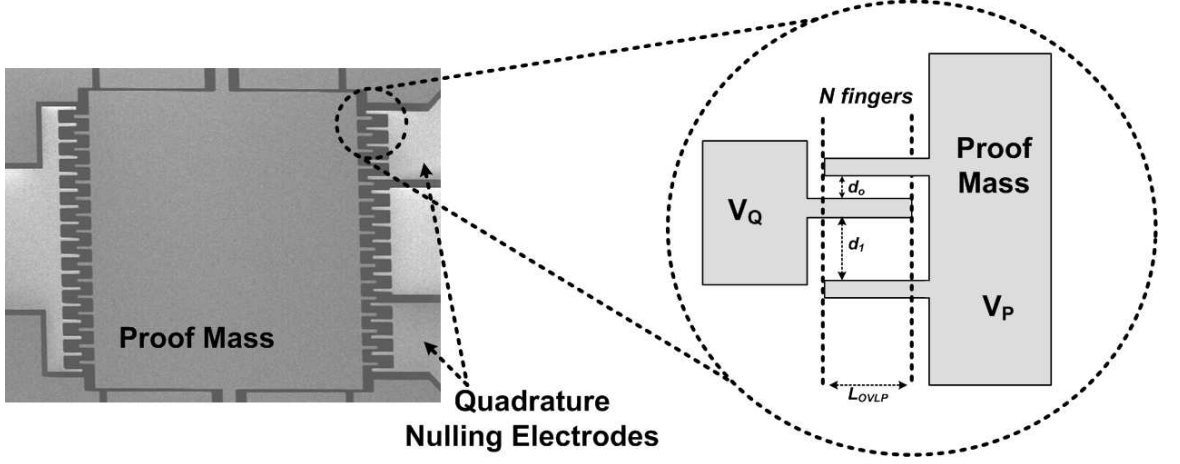


Figure 5.3: Dedicated quadrature nulling electrodes in the $M^2 - TFG$.

Mathematically, quadrature nulling can be represented as applying appropriate voltages to eliminate the cross-diagonal terms in the spring stiffness matrix of Eq.(5.5), as follows:

$$\mathbf{K}_M(\mathbf{QN}) = \begin{pmatrix} k_{xx} & k_{xy} \\ k_{yx} & k_{yy} \end{pmatrix} + \begin{pmatrix} 0 & -k_{xy-elec} \\ -k_{yx-elec} & 0 \end{pmatrix} = \begin{pmatrix} k_{xx} & 0 \\ 0 & k_{yy} \end{pmatrix} \quad (5.6)$$

where $k_{xy-elec}$ and $k_{yx-elec}$ are stiffness coefficients that result from the electrostatic torques applied to the dedicated quadrature nulling electrodes, resulting in the electromechanical matrix $K_M(QN)$.

Quadrature error in vibratory gyroscopes has been recognized as the single most important factor that precludes perfect mode-matching, i.e., zero frequency split between the drive and sense resonant frequencies [21]. A mode-matched gyroscope is one in which the drive and sense modes are eigenmodes, i.e., they are degenerate. The 2-DOF microgyroscope system can be considered degenerate only when its mass- and spring-stiffness matrices are diagonal. The quadrature induced off-diagonal terms in the spring-stiffness matrices prevents the eigenmodes to be degenerate leading

consequently to a mismatch in the resonant frequencies. In order to achieve mode degeneracy, it is necessary that these terms are electronically eliminated¹, and the spring-stiffness matrix be diagonalized. Therefore, it is clear that quadrature nulling is the first step to achieve perfect mode-matching.

Once the quadrature error has been nulled, the drive- and sense-stiffness coefficients can be made equal to ensure that the drive and sense frequencies are made equal. This is achieved through electrostatic spring softening and is the subject of the next section.

5.3 *Electrostatic Frequency Tuning*

The imperfections in micromachining that give rise to the quadrature error also result in deviation of the mechanical spring widths from their original design values. Despite tight process control, a $1.7\mu m$ wide beam can be defined no better than $0.2\mu m$ [14], causing the resonant frequencies to deviate from the desired value. For this reason, most MEMS devices use some form of electronic frequency control. Electrostatic spring softening is used to compensate this frequency variation.

Selective electrostatic tuning of the sense mode resonant frequency is an attractive feature of the $M^2 - TFG$. Due to the parallel plate electrodes along the sense direction, an increase of the DC polarization voltage (V_P) causes a lowering of the sense resonant frequency. The drive oscillations, on the other hand, are excited using comb-drive electrodes, making the drive frequency relatively independent of the changes in polarization voltage [45]. The sense mode resonant frequency is given by Eq.(5.7):

$$\omega_{SNS} = \sqrt{\frac{k_{y-mech} - \sum_{i=1}^N \left(\frac{\epsilon_0 A_i}{d_{so-i}} V_P^2 \right)}{M_{EFF}}} \quad (5.7)$$

¹In practice, it is never possible to attain perfect alignment in a mechanical structure. Therefore the objective of quadrature nulling is to decrease the quadrature signal sufficiently, so that it does not impede future mode-matching.

where N is the number of parallel plate electrodes with a DC voltage difference of V_P across them, A_i is the area and d_{so-i} is the capacitive gap of the i^{th} electrode, and M_{EFF} is the effective mass of the structure.

Fig 5.4 shows the measured variation of the sense mode frequency as a function of applied polarization voltage (V_P) for the $M^2 - TFG$. Note that the drive mode frequency stays relatively constant, as expected. The variation of the sense mode frequency as a function of V_P is parabolic, similar to that measured in micromachined resonators transduced electrostatically using parallel plate electrodes [23]. The sense frequency measured a variation of approximately $1600\text{ppm}/V$ over a tuning voltage range of 20V.

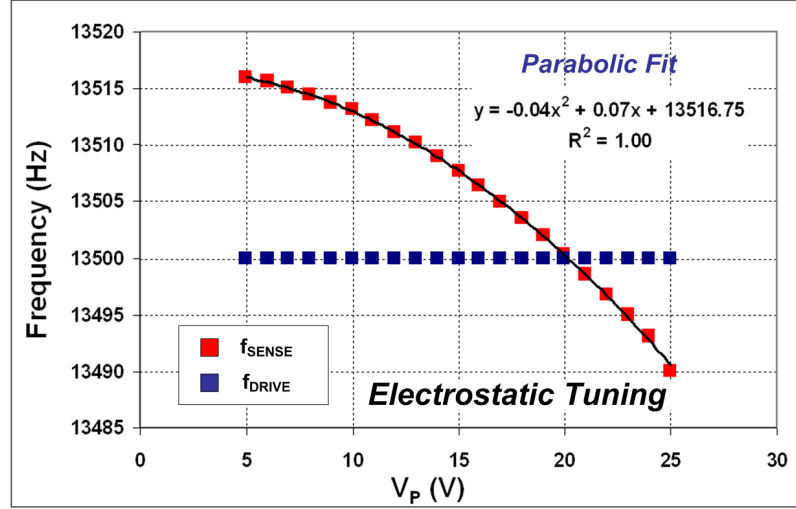


Figure 5.4: Tuning characteristics of the sense and drive resonant frequencies.

This selective electrostatic tuning of the sense mode resonant frequency is key to mode-matching. Eliminating the quadrature induced cross-coupling terms in the matrix, Eq.(5.6) alone is not sufficient to make the system degenerate. Electrostatic tuning complements quadrature nulling by ensuring the remaining diagonal elements are equalized electronically, thereby resulting in a diagonal matrix. This is represented

mathematically as:

$$\mathbf{K}_M(\mathbf{V}_P) = \begin{pmatrix} k_{xx} & 0 \\ 0 & k_{yy} \end{pmatrix} + \begin{pmatrix} \sum_{i=1}^N \left(\frac{\epsilon_O A_i}{d_{so-i}} V_P^2 \right) & 0 \\ 0 & \sum_{i=1}^N \left(\frac{\epsilon_O A_i}{d_{so-i}} V_P^2 \right) \end{pmatrix} = \begin{pmatrix} k_{xx} & 0 \\ 0 & k_{xx} \end{pmatrix} \quad (5.8)$$

Electrostatic spring softening can only be used to lower the mechanical resonant frequency due to the *negative* nature of the electrostatic springs. For this reason, the sense mode is specifically designed to be slightly higher in frequency than the drive mode, to enable frequency tuning and mode-matching even in the presence of process variations. Mode-matching is achieved by increasing V_P until the sense mode frequency decreases, and becomes equal to that of the drive mode - ~ 0 Hz split. Fig 5.5 shows the measured frequency response of the gyroscope as observed at one of the sense monitoring electrodes. The drive frequency stays constant with V_P , and the sense frequency is lowered until mode-matching is achieved.

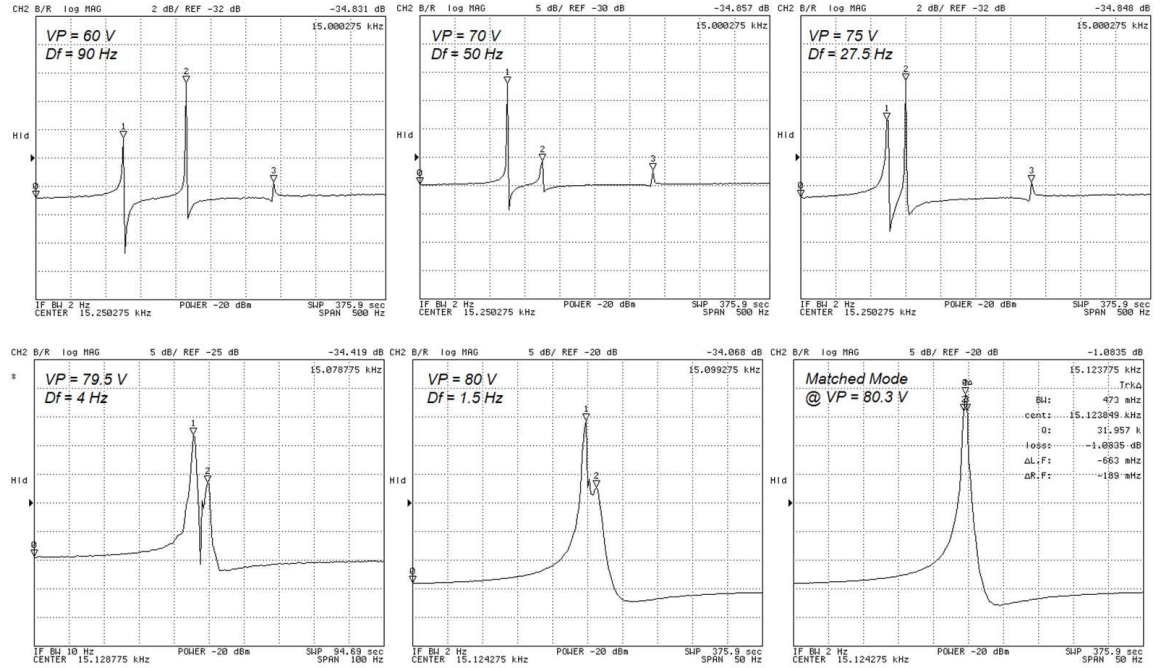


Figure 5.5: Measured frequency response function of the TFG showing mode-matching, as observed at one of the sense electrodes.

From the above discussion, it is clear that both quadrature nulling and frequency

tuning are necessary to attain mode-matched operation. Incomplete quadrature nulling does not eliminate the off-diagonal elements in the matrix, resulting in mode non-degeneracy. Attempts to match such a TFG will result in the minimum achievable separation between the drive and sense frequencies being much greater than zero. Quadrature error in previous designs of the $M^2 - TFG$ could not be completely nulled due to the lack of dedicated quadrature nulling electrodes [46]. Hence, the minimum frequency separation that could be achieved was 12Hz [44].

Finally, electronic control of the sense mode by means of V_P can be used for temperature compensation. Parabolic temperature compensation of micromachined resonators has been demonstrated to achieve frequency stabilities as low as $39ppm/^\circ C$ [25]. A similar technique can be applied for the temperature compensation of micromachined silicon gyroscopes.

This combination of electronic quadrature nulling and electrostatic tuning results in the previously non-degenerate modes of the TFG to become eigenmodes (degenerate modes), differentiating this mode-matched tuning fork gyro ($M^2 - TFG$) from other MEMS gyros [21, 14].

5.4 Importance of Mode-matching

The primary motivation for mode-matching is to leverage the mechanical signal amplification provided by the effective quality factor (Q_{EFF}) of the gyroscope. Typical mechanical quality factors are in the range of 10,000 - 50,000 [19]. Q_{EFF} depends on the inherent mechanical quality factors of the structure, as well as on the frequency split between the drive and sense modes. For a given mechanical structure, Q_{EFF} is maximum when the drive and sense resonant mode frequencies are equal.

A higher Q_{EFF} lowers both the Brownian noise floor as well as the electronic noise floor (via improved capacitive sensitivity), as given by Eq.(1.2) and Eq.(1.3) respectively. Since Coriolis induced energy transfer takes place the drive resonant

frequency, Q_{EFF} represents the effective mechanical gain of the sense resonant mode at the drive resonant frequency. It depends on the inherent mechanical sensor parameters as well as the separation between ω_{DRV} and ω_{SNS} . The capacitive sensitivity of the $M^2 - TFG$ depends on the amount of displacement of the proof-masses along the sense axis, q_{SNS} . This q_{SNS} – and therefore capacitive sensitivity of the sensor – is strongly dependent on the mode separation. When the drive- and sense-resonant modes are not matched [21], the capacitive sensitivity of the $M^2 - TFG$ is given by:

$$\frac{\Delta C}{\Omega_Z}|_{unmatched} = \frac{2N\epsilon_o A q_{drive} \omega_{DRV}}{d_{SNS}^2 \omega_{SNS}^2 \left(1 - \frac{\omega_{DRV}^2}{\omega_{SNS}^2}\right)} \quad (5.9)$$

where N is the number of sensing electrodes of area A , q_{drive} is the drive amplitude along the x -axis, and Ω_Z is the input rotation along the z -axis. For the unmatched case, the separation between the modes gives the sensor bandwidth. In the limiting case, when $\omega_{SNS} \rightarrow \omega_{DRV}$ (i.e., $\omega_{SNS} = \omega_{DRV} \sim \omega_O$), the modes are considered matched and the capacitive sensitivity is amplified by the mechanical Q_{EFF} as given by:

$$\frac{\Delta C}{\Omega_Z}|_{matched} = \frac{2N\epsilon_o A q_{drive} Q_{EFF}}{d_O^2 \omega_O} \quad (5.10)$$

The above improvement in capacitive sensitivity lowers the $ENE\Omega$, and therefore alleviates the noise specifications of the interface electronics. Finally, empirical studies have shown that a high Q_{EFF} contributes directly to a low bias drift.

Therefore, for a given form-factor, Eq.(1.2), Eq.(1.3), and Eq.(1.6) show that microgyroscope performance can be enhanced by orders of magnitude by the use of mode-matching. A high Q_{EFF} also alleviates the constraints on the interface circuit design in terms of operating frequency, gain, and power.

However, mode-matching is not without its own problems. Q -amplification increases the sensitivity of the gyro to the Coriolis-induced acceleration by Q_{EFF} ,

as well as any spurious displacements along the y -axis – like quadrature error. Further, mode-matching must be stable over time as well as temperature. Otherwise, continuous time monitoring must be performed, which can be power- and area-intensive. Finally, to leverage the benefits of mode-matching in a cost-effective manner suited for commercialization, it is necessary to achieve mode-matching automatically. Often, the challenges involved with the mode-matching of high-Q resonant modes of a structure are so significant that it is preferred to operate the gyroscope with a mode-mismatch of 5–10% in resonant frequencies.

5.5 Automatic Mode-Matching - Prior Art

The previous sections have discussed the motivation behind mode-matching to improve the drift, resolution and noise floor. Over the last few years, the potential CVG performance improvements via mode matching have spurred considerable research toward the development of automatic mode-matching schemes. Earlier methods of mode matching involved laser trimming of the proof-masses or flexures to reduce frequency split. This is expensive and time consuming, and the cost and time overheads are not justified in a number of applications. Therefore, there has been considerable work in developing automatic systems for electrostatic mode-matching MEMS gyroscopes [17, 47, 48].

Initially, electronic mode-matching was preformed manually. The frequency response of the gyroscope was measured on a network or dynamic signal analyzer to identify the drive and sense resonant frequencies. Appropriate voltages were applied to control the frequencies, so as to null the separation. This iterative procedure was repeated until the optimum set of mechanical bias voltages that yielded a drive and sense mode frequency separation of 0Hz was determined. For high-Q structures, this procedure could take several hours [17, 49].

Techniques wherein the resonant frequency of one micro-machined resonator is

pulled to the frequency of another resonator, forming an electro-mechanical frequency locked-loop have also been proposed. In [50], the frequency of a secondary oscillator is tuned so as to make it equal to that of a primary oscillator. The signal from the primary oscillator is sent to a frequency generator that produces test signals. These test signals are frequency-shifted versions of the primary resonant frequency, and are used to excite the secondary resonator. The amplitude- and phase-characteristics of the secondary resonator output are measured and compared with the output of the primary oscillator. The mechanical DC bias voltages that control the frequency of the second resonator are then varied by a controller, so that any difference signal is nulled. This is possible only if the secondary resonator is oscillating at exactly the same frequency as the primary oscillator. Thus, the tuning of the two resonant frequencies is achieved.

The use of a dual-PLL approach [48] has also been suggested to implement automatic mode-matching. In this approach, a first PLL is used to generate the drive oscillations. The second PLL is electro-mechanical, with the sense mode of the gyroscope forming the VCO. The electromechanical PLL is frequency-locked to the primary signal, where the phase detector and loop filter output act as the tuning voltage which is applied to the MEMS structure. No experimental results have been presented regarding the actual frequency separation of the modes.

So far, the most promising results in terms of automatic mode-matching as applied to microgyroscopes come from researchers at JPL and Boeing Systems [17], using the JPL microgyroscope [51]. Boeing and JPL have implemented a mode-matching ASIC that uses evolutionary computation to achieve automatic mode-matching of the drive and sense modes. The drive mode of the JPL MEMS microgyroscope was excited open loop and the frequency response measured [17]. Due to the quadrature induced cross-coupling, two peaks are observed in the frequency spectrum. These peaks correspond to the drive- and sense-resonant frequencies. The frequency separation between these

two peaks is first computed using peak-fitting algorithms, that are run on a PC. An evolutionary computation software then employs dynamic hill-climbing algorithms to determine the new DC bias voltages that must be applied to reduce the frequency split. This procedure is repeated iteratively until final optimum values of the DC bias voltages are determined. The complete procedure of the dynamic hill-climbing algorithm to reduce the frequency split from about 1.5Hz to less than 0.1Hz involved 47 iterations, and took about 1 hour.

Each of the above described methods suffers from important limitations. With the wide process spread prevalent in both surface- and bulk-micromachining technologies, laser trimming of each sensor element is not a cost-effective business model. The frequency-pulling technique of [50] and the dual-PLL approach of [48] are best suited for micromachined structures that have similar drive and sense excitation electrodes (both parallel plate or both combs). Both these approaches involve applying a time-varying tuning voltage to the mechanical structure. Both these approaches maintain the sense mode in a quasi-steady state of operation (i.e., the sense frequency is continually adjusted). This results in significant electronic feed-through and can lead to false rate outputs, especially in high-Q systems. Neither of these methods clearly demonstrates the effects on the quality factor of the sense mode. Finally, neither of the gyroscope systems described in [50, 48] exhibit navigation-grade performance.

The JPL-Boeing solution is the only MEMS-based gyroscope till date that demonstrates near-navigation-grade performance, while using automatic mode-matching. While the evolutionary algorithm can be placed on an FPGA, the hardware platform described in [17] requires the use of a network or dynamic signal analyzer to measure the frequency domain transfer function. Although impressive improvements have been reported in terms of the overall time taken for mode-matching as compared to manual tuning, due to the extensive hardware requirements and the time taken (\approx 1 hour), this approach is best suited for a one-time trim or calibration at a test facility.

Further, navigation gyroscopes operate in diverse environments: a navigation-grade gyroscope from the factory can be placed either in a satellite, or in the down-hole electronics module of an off-shore oil rig. Actual field conditions are impossible to recreate at the time of manufacture.

An automated system for mode-matching of gyroscopes would be invaluable for use in applications where frequent calibration of the gyroscope is not possible - for instance inertial measurement units for aircraft, unmanned surveillance vehicles, etc. The scheme developed in this work, on the other hand, exploits the imperfections present in a micromachined structure to control the resonant frequencies, and achieve mode matching in a fraction of the time and hardware as compared to the existing state-of-the-art.

5.6 Automatic Mode-Matching - Proposed Concept

The mode-matching scheme presented here exploits the unique characteristics of the sensor in the time domain, to achieve and maintain zero or finite frequency split between the two modes in a fraction of the time and hardware as compared to [17].

In practice, the required DC voltages to be applied at the quadrature nulling voltages are identified in a post-fabrication trimming step. However, despite quadrature nulling, there always exists a finite amount of ZRO. The key to developing an automatic mode-matching system is to leverage this often-ignored residual quadrature error. When the modes are matched, the sensor is sensitive to any displacement along the y -axis, whether quadrature-induced or Coriolis-induced. Hence, the amplitude of the residual ZRO serves as an accurate indicator of sensor sensitivity. Fig 5.6 shows the measured amplitude of the ZRO as a function of applied polarization voltage, and Fig 5.7 shows a close-up of the ZRO amplitude near mode-matched condition.

It is evident from Fig 5.6 that the maximum in ZRO amplitude occurs when the

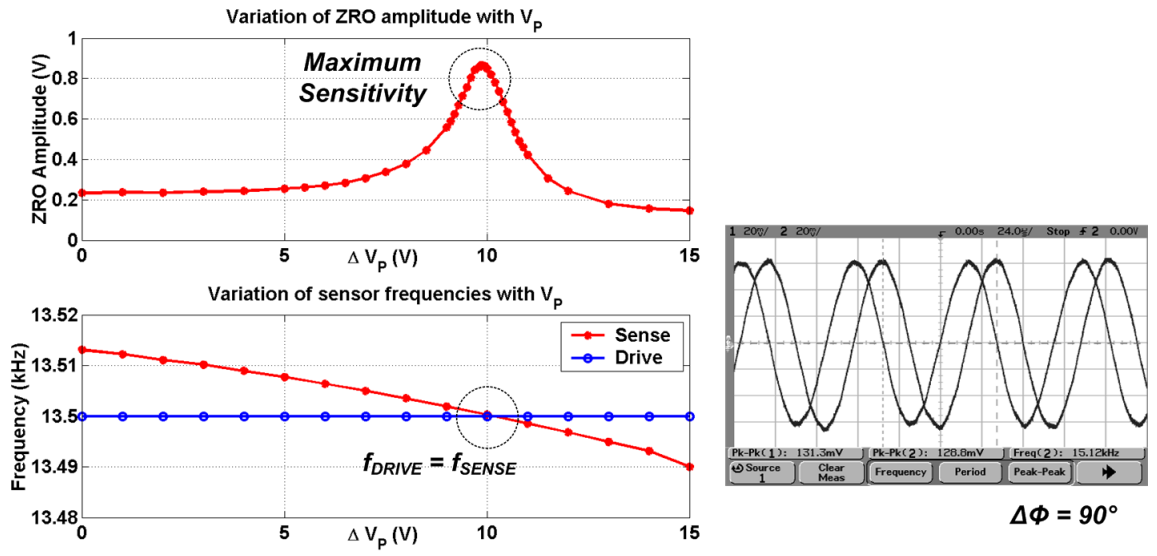


Figure 5.6: Characteristics of the TFG at mode-matched condition.

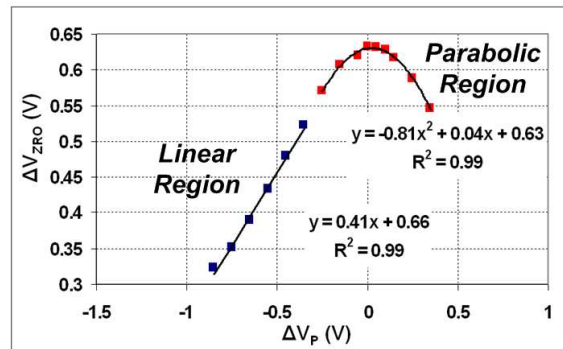


Figure 5.7: Close up of ZRO values as mode-matching is achieved, showing linear and parabolic regions.

frequency separation between the drive- and sense-resonant modes is nulled. Further, the unique 90° phase difference that exists between the drive output and the ZRO at mode-matched condition, as seen in Fig 5.6, is monitored for any modal instability after matching. Once matched, synchronous I-Q demodulation is used to distinguish between the quadrature error and the Coriolis signal.

Automatic mode-matching of the TFG is achieved using an iterative procedure, as shown in the flow chart of Fig 5.8. The ZRO level is measured and the V_P increased until a maximum in ZRO amplitude is detected. Once the maximum is detected, the V_P is held constant.

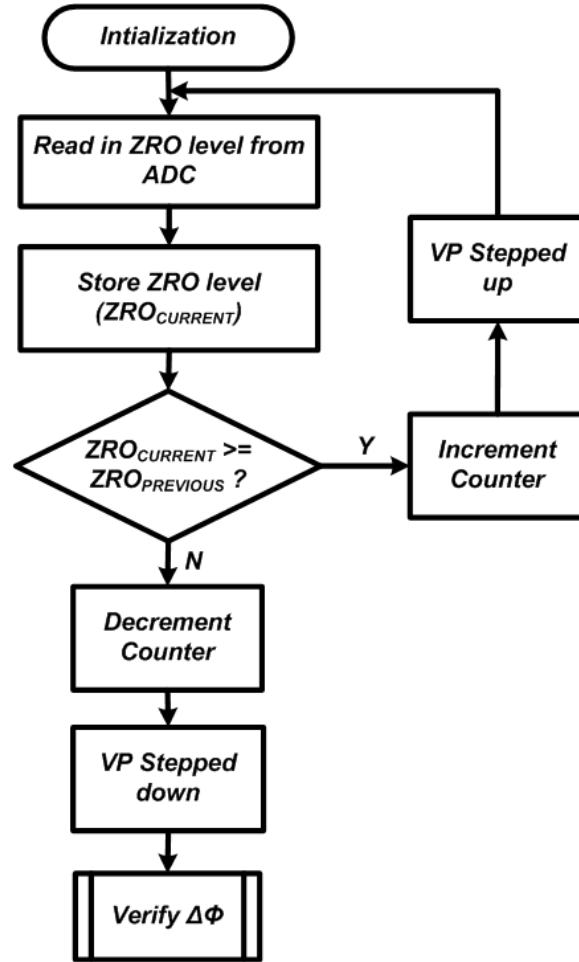


Figure 5.8: Flow-chart showing the proposed automatic mode-matching scheme.

An attractive feature of the proposed approach is that the frequency separation

between the modes can be determined from the ZRO amplitude. This feature can be used for bandwidth control of the microsensor, where a finite separation between the modes can be introduced and maintained. Therefore, dynamic configurability of the sensor during operation is possible without having to recalibrate or power-down.

CHAPTER VI

CMOS AUTOMATIC MODE-MATCHING SYSTEM

6.1 Circuits and System design

A schematic of the proposed automatic mode-matching system is shown in Figure 6.1. The ZRO level monitor produces a digital bit-stream whose average value is representative of the amplitude of the input signal. The amplitude of the ZRO is detected using a CMOS level detector. The DC level is then converted into a pulse-width modulated bit-stream using a $\Sigma\Delta$ modulator. Since the duty cycle of the bit-stream is proportional to the input DC level, the computed average of the bit-stream yields an accurate measure of the ZRO amplitude. Based on the ZRO level, the mode-matching algorithm determines the appropriate direction to step the V_P using the V_P -Stepper. The CMOS implementation of the various blocks and the software interface are discussed below.

6.2 ZRO Level Detector

6.2.1 Design Considerations

Classically, a level detector consists of a diode-based voltage rectifier, and peak detector which stores the maximum value of a signal on a capacitor [40, 52, 53, 54]. This method suffers from a number of draw-backs. An op-amp with a very high slew rate is required. The peak-detection method is sensitive to random variations in the input signal level [55], which makes it especially unusable in the current application for microgyro ZRO level detection. Diodes for rectification require the use of a BiCMOS process (which is not cost-effective) or substrate BJT's in a CMOS process. Substrate BJT's can suffer from junction leakage, thereby affecting the stored level. Level detection by synchronously demodulation and low-pass filtering of the ZRO signal

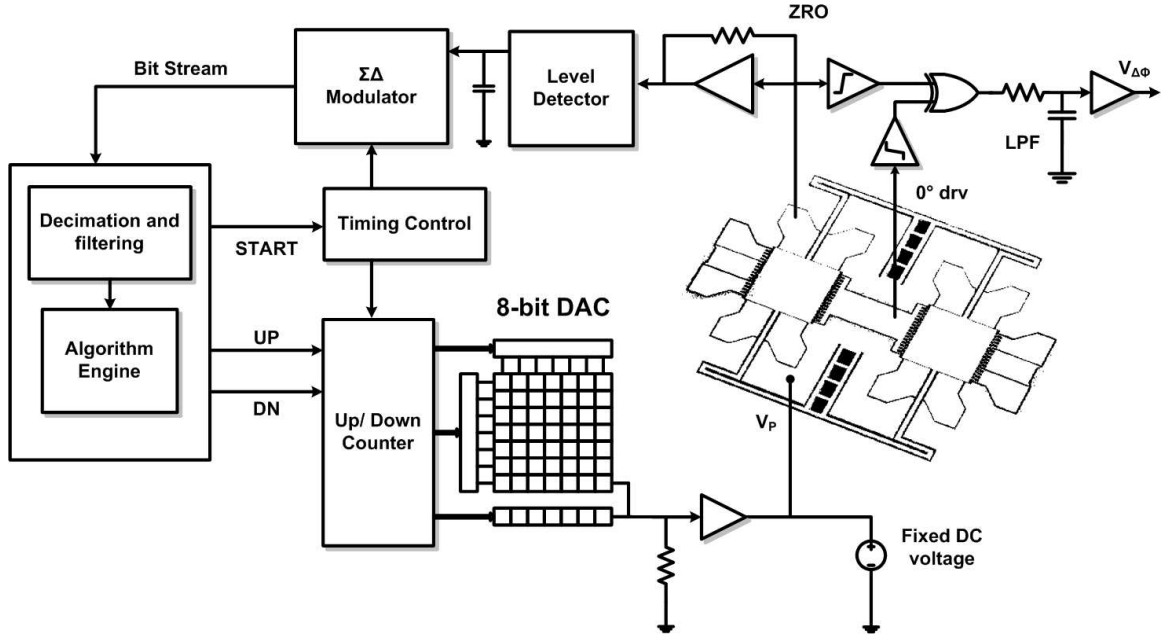


Figure 6.1: Schematic of the automatic mode-matching system.

cannot be used in the mode-matching sub-system. This is because both phase- and frequency-variations, which arise during electrostatic tuning, will appear at the low-pass filtered output, causing an incorrect recording of the ZRO level. Therefore, it is necessary to employ a level detection technique that is independent of the frequency or phase of the ZRO.

In this work, ZRO level detection is accomplished by converting the input voltage signal into a current, rectifying the current, and integrating it on a capacitor [55]. The schematic of the ZRO CMOS level detector is shown in Fig 6.2. Amplitude detection, using current rectification followed by integration, is not as sensitive to signal variations as peak detection. Any transient signal variations are averaged out by the integration, thereby offering a better estimate of the ZRO level.

Voltage-to-current conversion of the input ZRO signal is performed using a two-stage push-pull differential to single ended op-amp. The fully differential nature of the first stage is retained by using diode connected PMOS loads instead of a current mirror load. The gain of the first stage is set by the ratio of g_{m1}/g_{m3} . In this case,

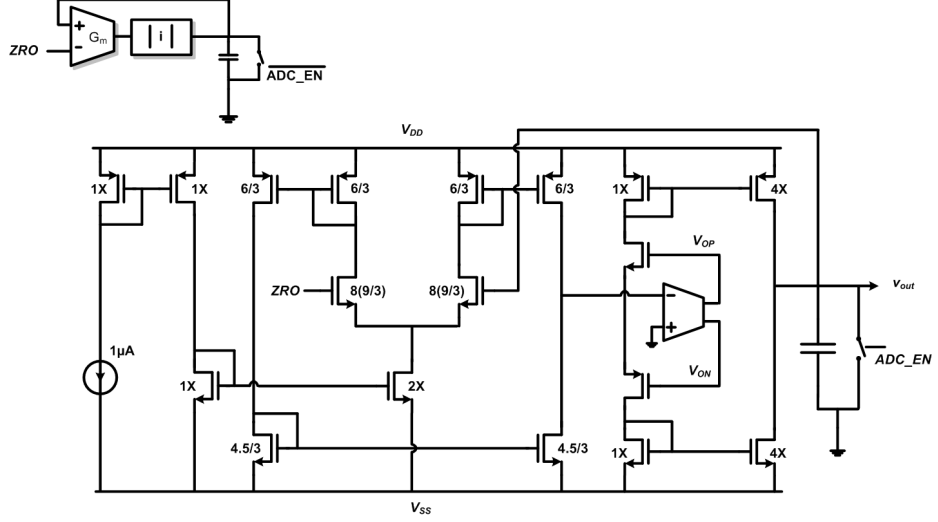


Figure 6.2: Schematic of the envelope detector.

the transconductance ratio is chosen to be 12. The output current is then rectified using a class-B mirror topology with active feed-back [56]. Full-wave rectification is possible since this topology allows for sourcing and sinking of current I_{IN} . Dead-zone reduction improves dynamic range of this current rectifier and this has been implemented by introducing a DC level shift by means of a *floating-battery* active feed-back amplifier, as suggested in [56]. The DC level shift also improves the response time of the amplitude detector to low input current values. The integration capacitor was implemented as an off-chip 1nF capacitance. A CMOS transmission gate switch was placed in parallel with the capacitor to allow discharging after level detection, and to reset the capacitor before the next level was detected. All the biasing currents are generated using a constant transconductance bias circuit.

6.2.2 Measured Performance

Fig 6.3 shows the measured input-output characteristics of the level detector, which has 6.5 bits of linearity between $200mV_{PP}$ and $1.2V_{PP}$, for an input signal with frequency 20kHz. Also shown in Fig 6.3 are the 20kHz input sinusoidal signal with increasing and decreasing amplitudes, and the corresponding DC level output by the

level detector. As shown in the inset of Fig 6.3, the ZRO level detector is sensitive to variations as small as 1mV in the input signal amplitude, which is sufficient for interfacing with the $M^2 - TFG$.

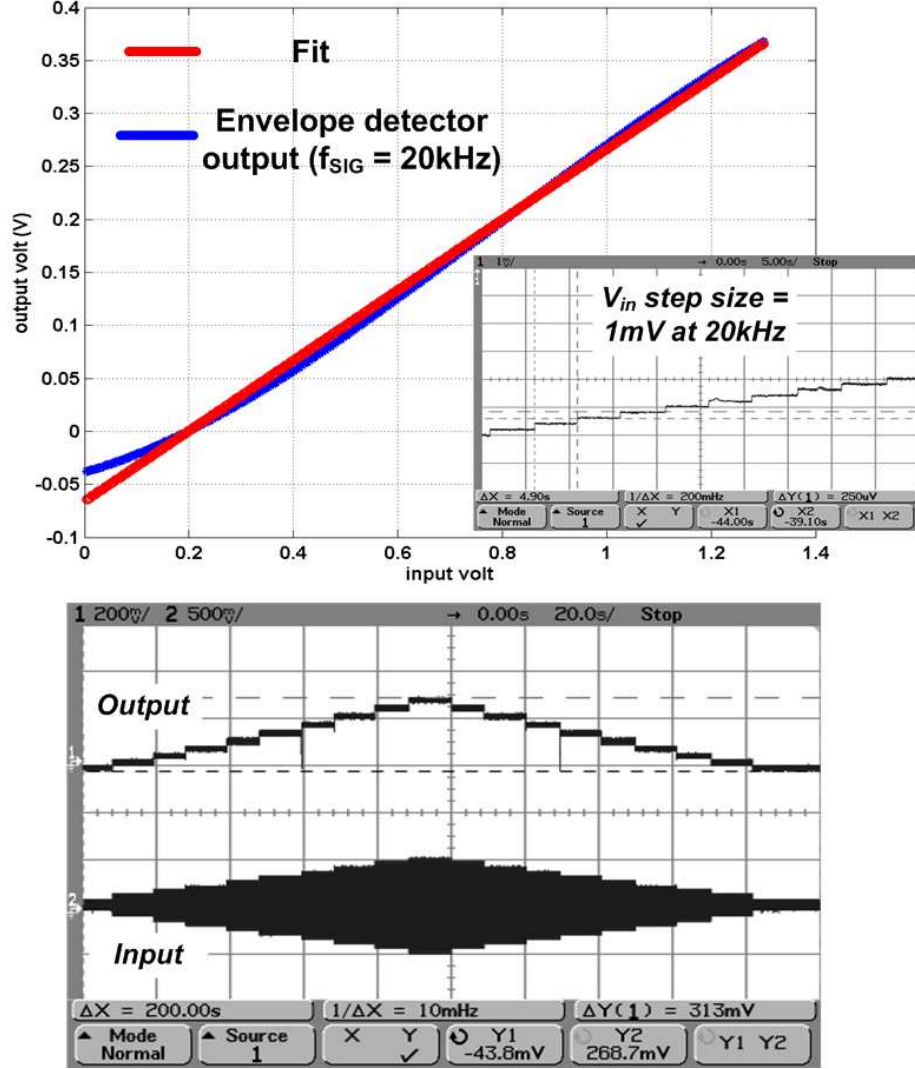


Figure 6.3: Measured input-output characteristics of the envelope detector and waveforms showing amplitude stepped 20kHz input signal and corresponding output (Inset) Response of the envelope detector to 1mV change in input amplitude.

6.3 *Sigma-Delta Modulator*

6.3.1 Design Considerations

Decreasing the frequency split from 10Hz to ~ 0 Hz resulted in an increase in ZRO amplitude of about 500mV as seen in Fig 5.6. Since the level detector can resolve a DC level shift of as low as 1mV, this implies the A/D converter must have a resolution of at least 9 bits. A $\Sigma\Delta$ modulator is used to convert the ZRO level into a bit-stream as it offers the required resolution, with minimal area and power consumption. The duty cycle of the bit-stream is proportional to the input DC level, and the computed average (i.e., after decimation) of the bit-stream yields an accurate measure of the ZRO amplitude. The $\Sigma\Delta$ is operated in a one-shot manner, where each iteration of the tuning algorithm involves reading the bit-stream into the PC via GPIB, and performing the decimation to yield the DC value.

Fig 6.4 shows the circuit schematic of the implemented 1st order switched-capacitor $\Sigma\Delta$ modulator which uses correlated double sampling (CDS) to mitigate flicker noise and offset. The core op-amp used for the $\Sigma\Delta$ integrator was a two-stage Miller-compensated OTA that was optimized for noise. The OTA used large PMOS input transistors for lower flicker noise, had a high DC gain (>110 dB) to reduce input referred offset, a measured UGBW of 2MHz, and consumed 500μ W of power. The buffer between the integration capacitor and the $\Sigma\Delta$ is necessary to prevent loading of capacitor C_S . The $1nF$ external integration capacitor of the level detector serves as an effective anti-aliasing filter for the DC input. The capacitors C_S and C_F were fixed to 1pF and 0.5pF respectively, and C_{CDS} was chosen to be 2pF.

6.3.2 Measured Performance

Fig 6.5 shows the input and output time domain waveforms of $\Sigma\Delta$ to a sinusoidal and DC ramp input. From the output of the $\Sigma\Delta$ to the DC ramp, the full scale voltage range is calculated to be 1.8V. However, to maintain linearity of conversion, the $\Sigma\Delta$

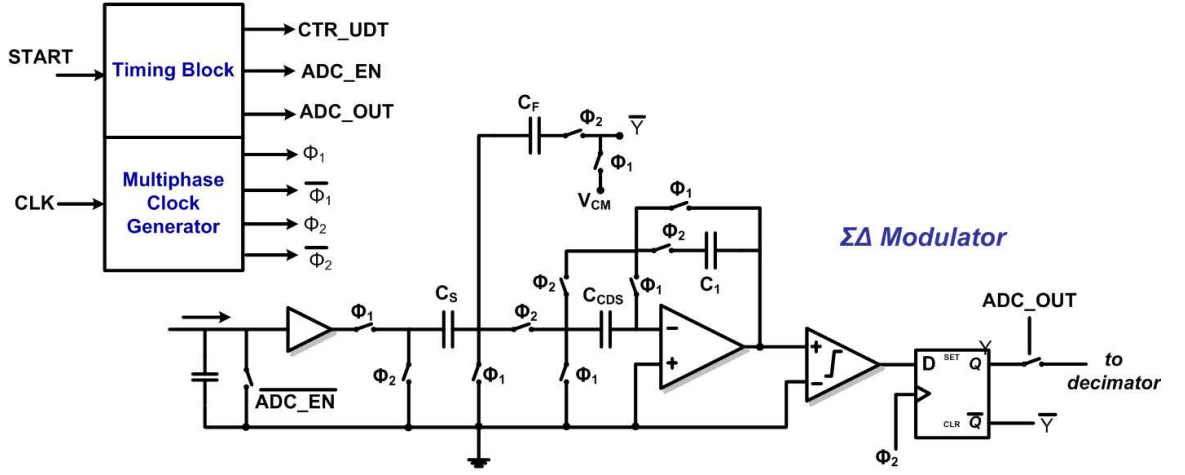


Figure 6.4: Schematic of the sigma-delta modulator.

input was restricted to half of that value ($\pm 0.5V$), which corresponds to 25% - 75% duty cycle of the PWM bit-stream, and is sufficient for this application.

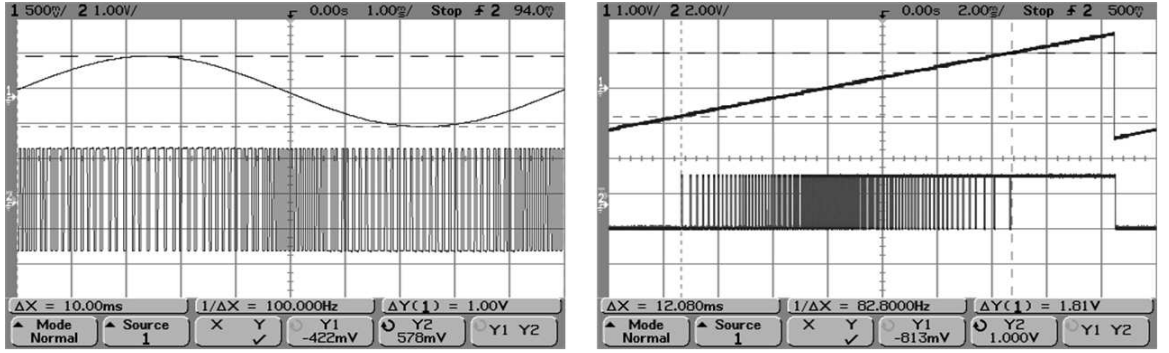


Figure 6.5: Measured response of the $\Sigma\Delta$ to sinusoidal and ramp input signals.

The SNR of the $\Sigma\Delta$ must be at least 65dB (~ 10 bits) to resolve the ZRO level. The noise characteristics of the $\Sigma\Delta$ in Fig 6.6 clearly show the first order noise shaping. Also shown in Fig 6.6 is the measured input referred voltage noise of the core OTA. The noise floor at 100Hz is $200nV/\sqrt{Hz}$, and the thermal noise floor is about $40nV/\sqrt{Hz}$. The maximum $\Sigma\Delta$ SNR measured was 88dB(~ 14 bits) at 100Hz with an OSR of 256, which was sufficient for this application. The inset of Fig 6.6 shows the variation of the SNR at 100Hz as a function of input power. The $\Sigma\Delta$

was designed to meet a higher SNR specification, so that the clock frequency can be lowered to be an integer multiple of the sensor operating frequency (between 20 - 30 kHz). This helps to lower power dissipation, and any ripple from the envelope detector can then be eliminated due to the over-sampling. When clocked at 25.6 kHz, the power dissipation of the $\Sigma\Delta$ was 0.9mW.

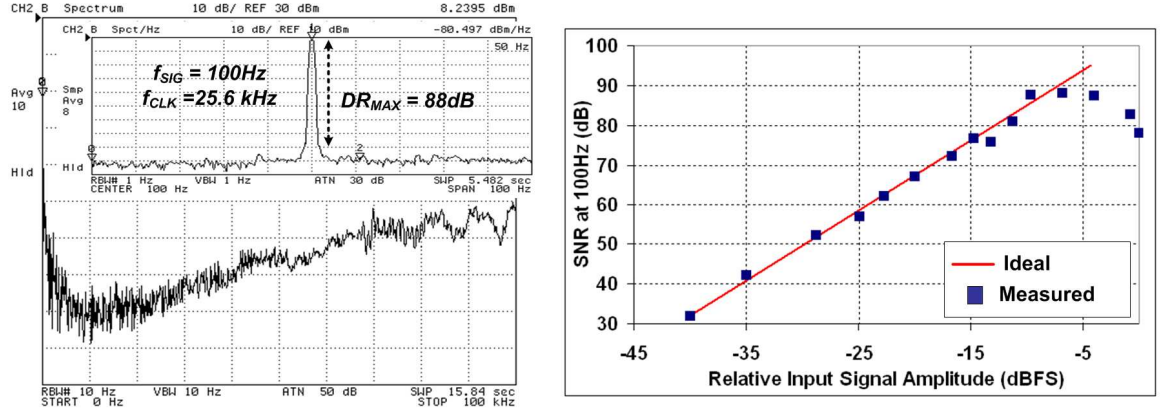


Figure 6.6: Measured noise spectrum of the $\Sigma\Delta$ modulator showing the first order noise shaping with maximum SNR of 88dB/Hz. Plot of SNR vs. relative input signal level.

6.4 Timing Considerations

The initial value of polarization voltage (V_P) is set using an external DC power supply. The mode-matching algorithm is implemented in MATLAB, and performs the following three steps in each iteration until a maximum in ZRO level is detected:

1. Sends an interrupt (START) to the timing unit that generates digital pulses which read in the ADC bit stream, resets the level detector and updates the counter values
2. Compares the decimated value of the ZRO level from the current iteration with that from the previous one
3. Outputs a 2b control word to the V_P stepper

A timing diagram is shown in Fig 6.7. Once the maximum has been detected, V_P is decremented to its previous value, which corresponded to peak sensitivity. At matched mode, the distinct 90° phase difference that exists between the drive signal ($0^\circ drv$) and the ZRO is monitored to ensure that mode-matching has indeed been achieved.

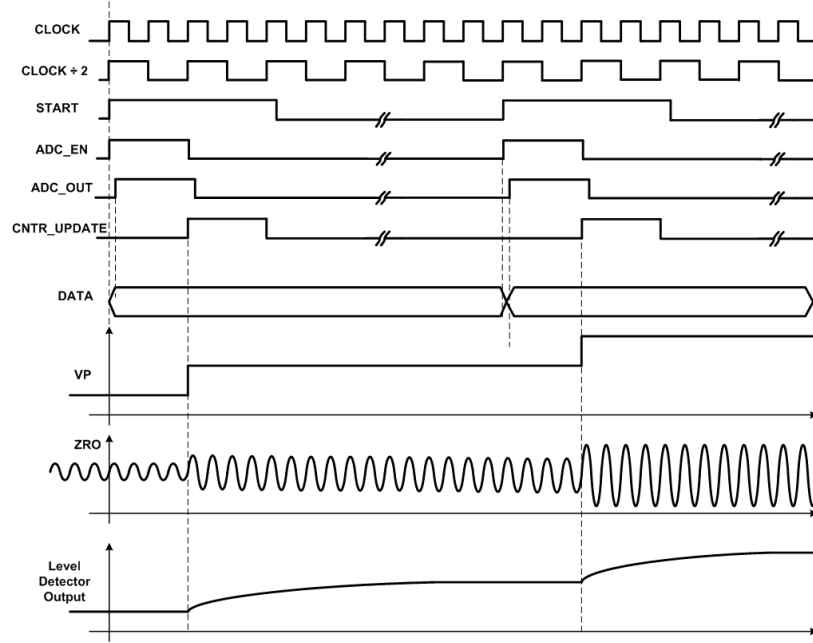


Figure 6.7: Timing Diagram showing relationship between control signals and sensor outputs.

Due to the high open-loop mechanical quality factor, the microgyroscope has a settling time of about 1 - 2 seconds. A single iteration of the mode-matching algorithm was therefore allotted a total of 200ms (about 10% of the total sensor settling time). The longest component of each iteration involved reading in the 4096 cycles of the $\Sigma\Delta$ bit-stream ($\sim 164\text{ms}$ at f_{CLK} of 25.6 kHz).

6.5 V_P -Stepper

6.5.1 Design Considerations

From the plot of ZRO amplitude vs. change in polarization voltage (ΔV_P) of Fig 5.6, a 1V variation of V_P about the value required for mode-matching (V_{P-MM}) causes the ZRO level to change by as much as 50%, and corresponds to a reduction in Δf from 15Hz to 0.5Hz. To obtain sufficiently fine frequency control, the minimum voltage step for V_P is chosen as 5mV over a span of 1V. This calls for a V_P stepper resolution of at least 8 bits. In addition, the V_P stepper must be able to increase as well as decrease V_P , to implement electronic bandwidth control.

The V_P stepper has been implemented by cascading an 8-bit bi-directional counter with a digital to analog converter (DAC), as shown in Fig 6.8. The bi-directional counter counts up, down, or holds its value, and can be controlled by means of a 2 bit control word [57].

The DAC has been implemented using a 6 + 3 partially segmented current steering architecture, adapted from the 12-bit design presented in [58]. While the DAC was designed for 9-bit resolution, the measured results presented here are for the DAC operated with 8 bits ($B_8 = 0$). A segmented current steering topology was chosen, because it is inherently monotonic and provides the required resolution at a reasonable area and power budget. The 3 LSBs were set by binary weighted current sources, while the 6 MSBs were generated using two 8×8 array of 64-unit current sources (i.e., thermometer decoded). The number of bits in the thermometer section was limited to 6 in order to retain the simplicity of the decoding logic. The thermometer row and column decoders were implemented using conventional combinatorial logic [59] without any pipe-lining, as speed is not a limiting design criterion.

Fig 6.9 shows a circuit schematic of the DAC current cell. In order to minimize power dissipation, the full scale current of the DAC was chosen to be $15\mu\text{A}$, which corresponds to an LSB current of 30nA. For a given ($V_{GS} - V_T$), the minimum gate

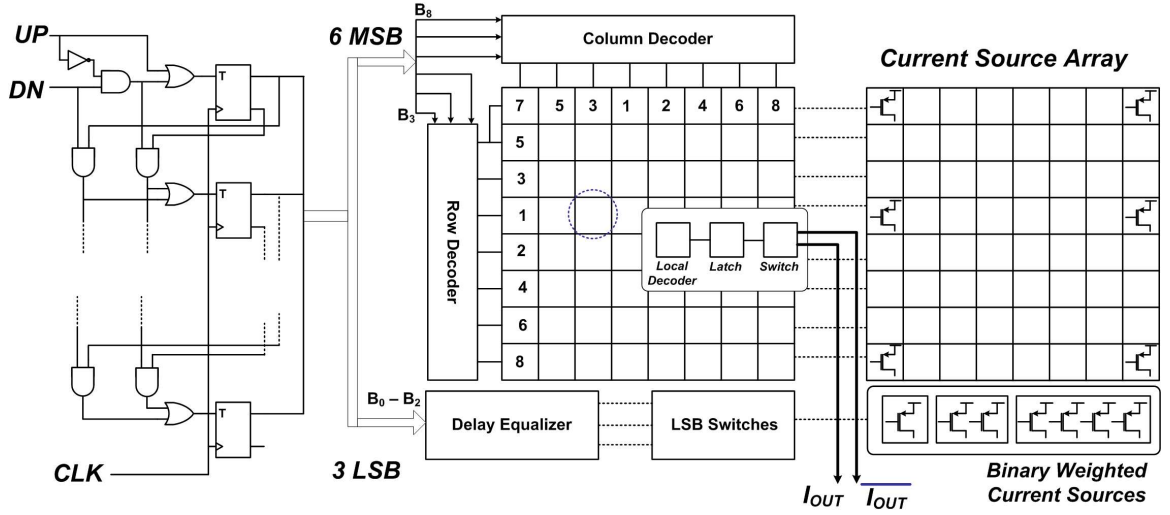


Figure 6.8: Schematic of the V_P stepper.

area required to meet the matching requirements in the $0.6\mu\text{m}$ CMOS process used here can be computed [58]. The LSB current determines the W/L ratio of the current source transistor, and along with the minimum gate area requirement, the size of the transistor is determined as: $W = 3.75\mu\text{m}$, $L = 21\mu\text{m}$.

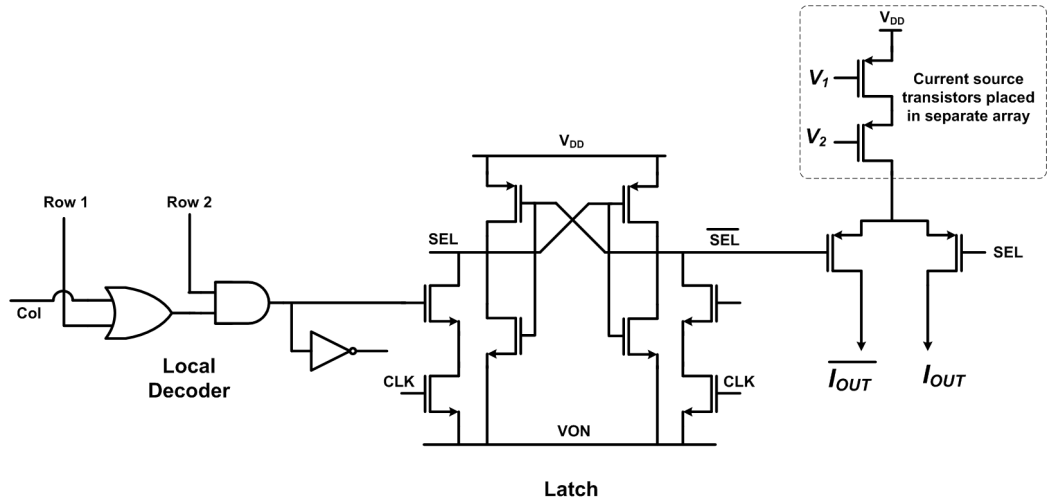


Figure 6.9: Schematic of the current cell used in the DAC of the V_P stepper.

The current source transistors were placed in a separate array, away from the local decoders [59] and switching transistors, to ensure good matching and immunity

from switching noise. Each of the cells in the switching matrix comprised of the local decoder [59], a latch with a reduced voltage swing [58] to ensure higher linearity and faster operation, and switching transistors. Each of the 63 current source transistors that implement the 8×8 MSB array was split up into two sub-units placed in a 1-D common centroid fashion, to minimize random mismatch. Due to area limitations, a full 2-D common centroid layout of the array was not possible. Further, a symmetrical switching scheme [59] was used to switch the current source transistors, allowing for the compensation of 2-D random mismatch errors in each of the two sub-arrays.

6.5.2 Measured Performance

Fig 6.11 shows the measured INL and DNL of the DAC, when cascaded with the 8-bit bi-directional counter ($B_8 = 0$). The measured DNL is less than ± 0.5 LSB, ensuring that there are no missing codes during 8 bit operation. The maximum update frequency of the DAC was 1MHz, which is sufficient to satisfy the 200ms timing budget for an iteration. Further, measured the full-scale current is $8\mu\text{A}$, and the corresponding INL was 0.92LSB. The measured INL is slightly higher than the target value of 0.5LSB, and is attributed to the incomplete mismatch cancellation of the MSB unary current sources.

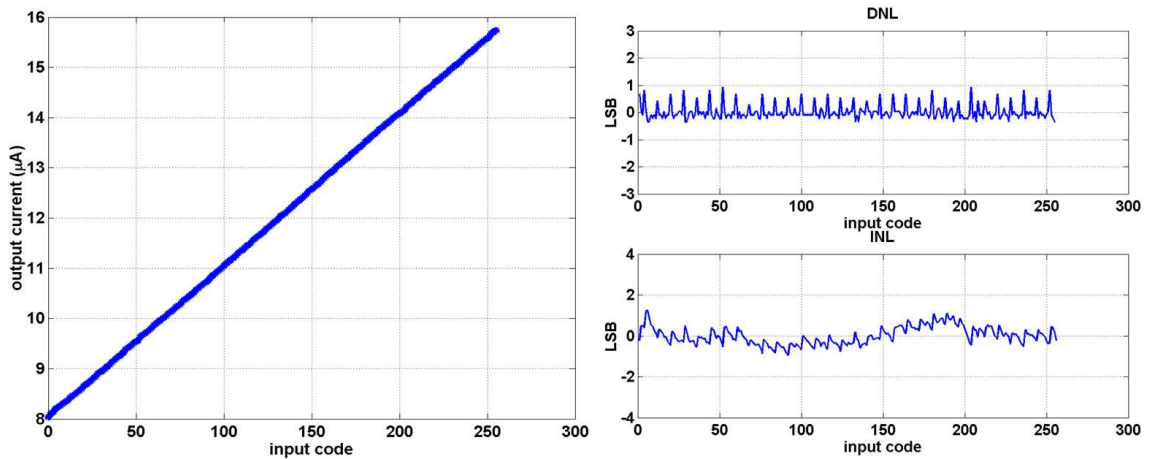


Figure 6.10: Measured output of the DAC and the measured INL and DNL.

The output current of the DAC is converted into a voltage using an off-chip $15\text{k}\Omega$ resistor. The voltage is buffered, added to the required offset voltage from a DC power supply, and applied directly to the MEMS structure. Fig 6.11 shows the output of the 8-bit V_P stepper while the counter is incremented and decremented. Note that the counter updates (and hence the V_P value changes) only at the negative edge of the CTR_{UDT} signal generated from the timing block.

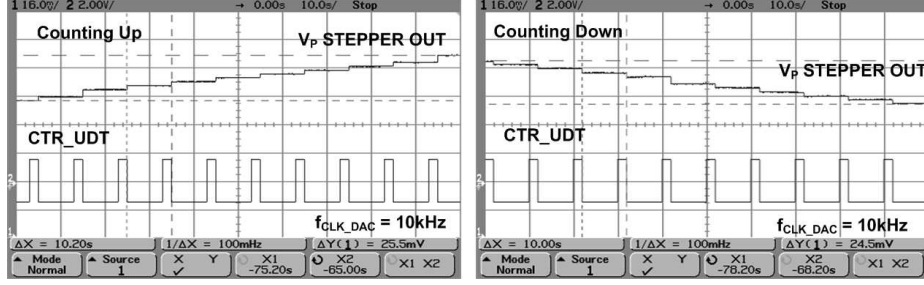


Figure 6.11: Results of the V_P stepper.

6.6 Experimental Results

6.6.1 Mode-matching in Time and Frequency Domains

The initial value of V_P corresponds to a mode separation of about 20Hz for the $60\mu\text{m}$ -thick SOI TFG. As seen in Fig 6.12, the minimum frequency separation that can be achieved between the drive- and sense-frequencies, without any quadrature nulling, is about 8Hz .

Fig 6.13 shows the time domain results of interfacing the $M^2 - \text{TFG}$ with the mode-matching CMOS ASIC and control algorithm. The gyroscope drive mode is excited into resonance using the PLL-based electromechanical oscillator. The predetermined DC voltages are applied to the quadrature nulling electrodes, and the mode-matching algorithm is started on the PC. Fig 6.13 shows the ZRO output increasing (upper trace) as the DAC is incremented (lower trace). Once the maximum in ZRO amplitude has been reached, the ZRO level does not increase further, and the DAC decrements to its previous value.

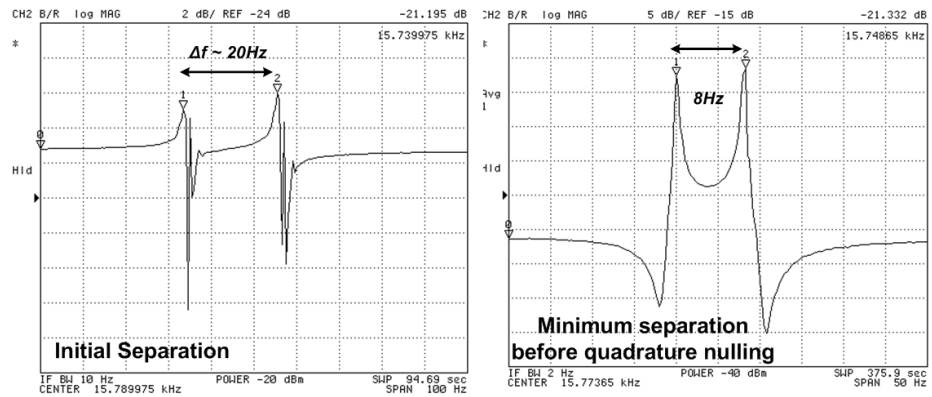


Figure 6.12: Initial separation between the modes and minimum achievable separation without quadrature nulling.

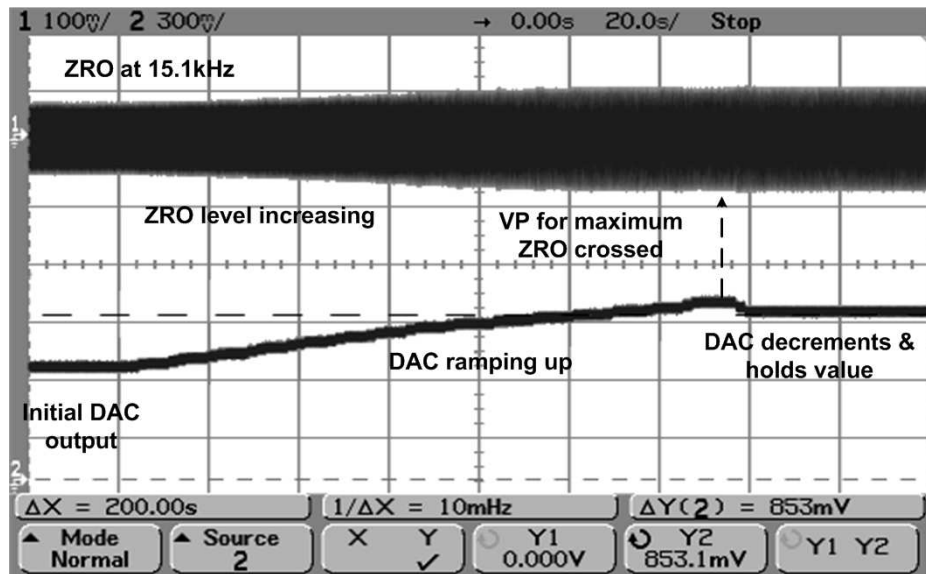


Figure 6.13: Time domain plot showing increase of the ZRO with VP.

The frequency separation between the drive and sense modes have been nulled, and the effective matched-mode quality factor (Q_{EFF}) is measured to be 36,000, as shown in Fig 6.14. This verifies that quadrature nulling and mode-matching of the $M^2 - TFG$ have been achieved without any degradation of quality factor.

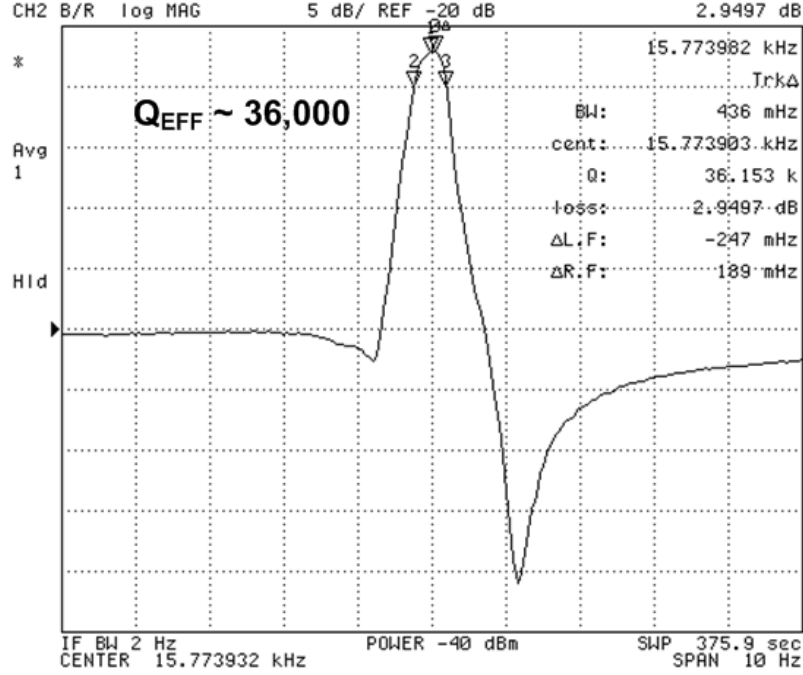
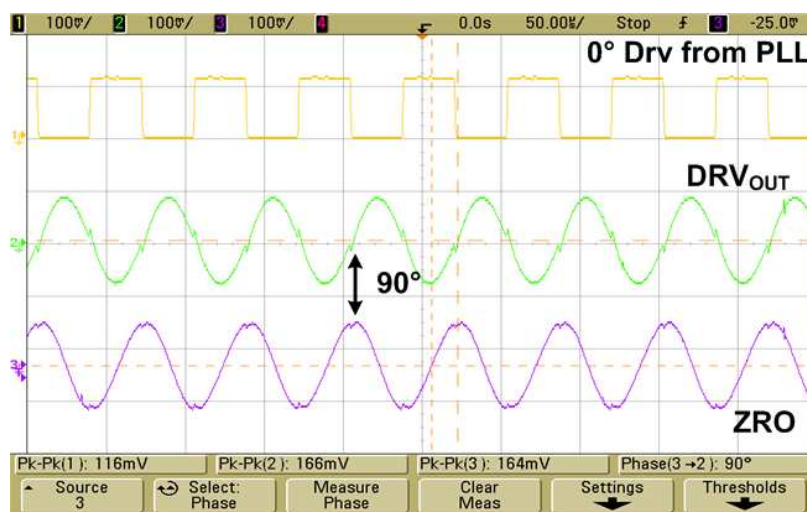


Figure 6.14: Mode-matched operation showing Q_{EFF} of 36,000.

The algorithm took about 18 iterations to match the two modes, with the DAC output varying by 300mV. Fig 6.15 shows a snapshot of the various signals at mode-matched condition. As expected, at matched-mode, there is the characteristic 90° phase difference between the drive output signal and the ZRO.

6.6.2 Mode-matching stability over temperature

The mode-matched sensor is extremely stable over temperature. This is because once matched, the two resonant modes track with temperature and hence mode-matching is retained, as shown in the inset of Fig 6.16. The slight degradation in matched-mode Q_{EFF} is attributed to thermoelastic damping [19].



Waveforms at Mode-matched condition

Figure 6.15: Microgyroscope waveforms at mode-matched condition showing the 90° phase difference between drive output and ZRO.

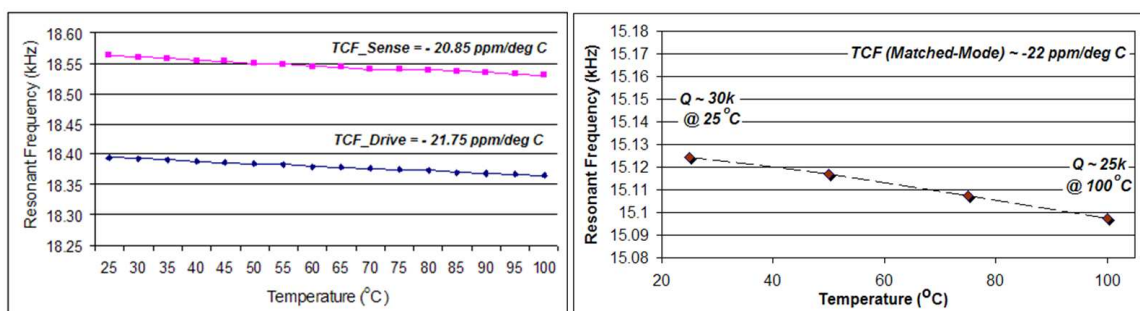


Figure 6.16: Mode-matching as a function of temperature.

The proposed mode-matching scheme allows for easy integration with temperature compensation schemes that have been reported for micromechanical resonators [25]. A current-mode DAC has the advantage that a PTAT current can be added to the DAC output to ensure temperature stability of the V_P . This current mode approach has the potential for lower power operation as compared to other schemes.

6.6.3 Mode-matching stability over time

Long-term microsensor performance was characterized to analyze the stability of mode-matching over time. Any mismatch of modes over time leads to a reduction in the Q_{EFF} from its mode-matched value, thereby affecting sensor performance. Environmental effects like temperature fluctuations can be compensated for, but random mismatch of the modes can be corrected only by performing periodic checks and re-calibration as required. This involves monitoring the modes in continuous time, and appropriate correction circuitry, which involves a considerable hardware and power overhead.

To test for any random mismatch of the modes after mode-matching, the microsensor was operated (i.e., locked into drive resonance) at rest continuously for a period of 30 hours at $25^\circ C$. The drive oscillator signals and ZRO were recorded for the period in intervals of 10 seconds. The analysis of the data collected determines whether periodic calibration of the sensor is necessary, and if so, how often it must be performed.

The buffered DAC output voltage that supplies the V_P was sampled for a period of 4 hours, and the maximum variation was measured to be $\pm 0.05\%$. This variation is small, and its effect on overall system stability is negligible. A more sensitive measure of mode stability is the 90° phase difference that occurs at mode-matched condition. Fig 6.17 shows the recorded rms value and phase difference of the ZRO over a period of 30 hours, which proves that once matched, the modes remain matched. Any mode

separation due to changes in circuit parameters or inherent to the MEM device would have resulted in a change of the phase or amplitude of the ZRO.

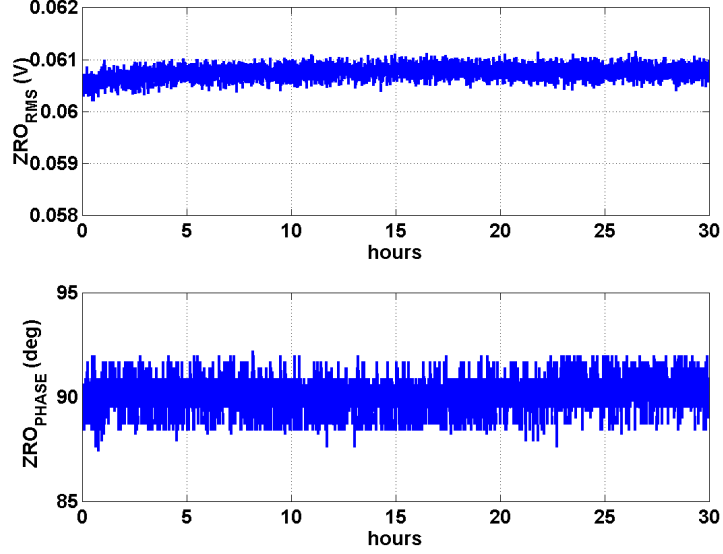


Figure 6.17: Long-term stability of the mode-matched gyroscope.

This validates that the automatic CMOS-software mode-matching of the $M^2 - TFG$ modes is extremely stable over time. No continuous-time monitoring or periodic calibration of the modes is necessary to maintain sensor performance.

6.6.4 Scale factor

The $60\mu m$ $M^2 - TFG$ was placed on an Ideal Aerosmith 1291BR rate table and characterized to measure the scale factor. The maximum mode-matched rate sensitivity was measured to be $88mV/^\circ/s/$ as shown in Fig 6.18, with the maximum nonlinearity measured to be less than 2%.

Also shown in Fig 6.18 are the rate outputs from one of the channels of the sensor when it is subjected to a $0.1^\circ/sec$ 0.1Hz sinusoidal rotation and a $5^\circ/s$ 1Hz sinusoidal rotation, respectively. It must be noted that there is a dependence of scale factor on the input signal bandwidth. However, for bias drift measurements, the maximum possible scale factor must be taken into account, since this is a DC phenomenon.

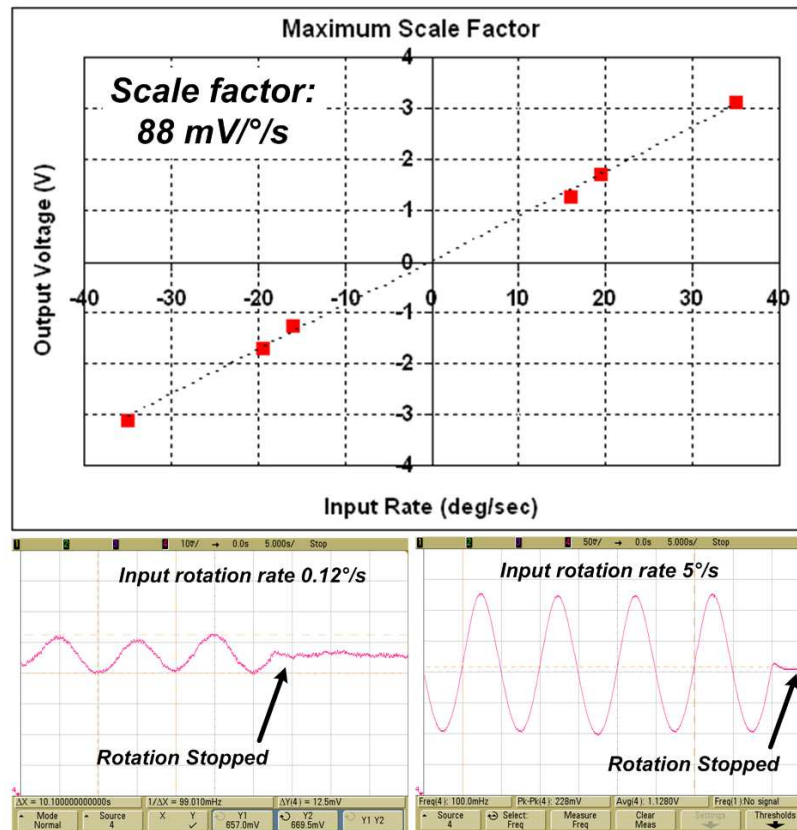


Figure 6.18: Scale factor measurement and output of gyroscope sinusoidal rates.

6.7 Electronic Bandwidth Control

For a micromachined Coriolis vibratory gyroscope, the frequency separation between the two resonant modes (Δf) is a measure of the effective open-loop sensor bandwidth. The advantage of this proposed mode-matching scheme is that once matched, controlled electronic separation of the drive and sense resonant modes are possible, thereby allowing programmability of the microsensor bandwidth, as shown in Fig 6.19.

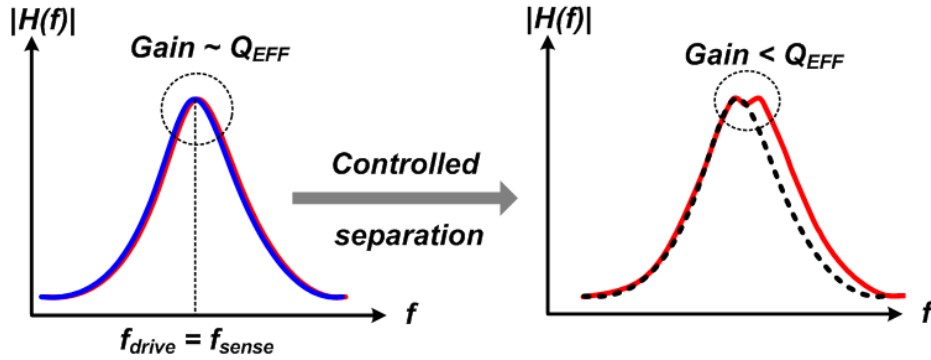


Figure 6.19: Concept of electronic bandwidth controlled using controlled split up or resonant modes.

The change in V_P (ΔV_P) necessary to introduce a specific amount of mismatch between the drive and sense modes is calculated from the tuning characteristics of the microgyroscope, and stored in a look-up-table (LUT). Since the DAC voltage step is fixed, the number of iterations the DAC must increment or decrement to achieve the desired frequency separation is known. The required number of CTR_{UDT} pulses is sent out by the PC to the bidirectional counter, and the V_P stepper increments or decrements until the target V_P is set. This automatically sets the bandwidth of the microsensor without addition of an extra control loop or added hardware. Fig 6.20 shows the schematic of the electronic bandwidth control system.

The proposed bandwidth control technique was verified using a second M^2-TFG that was matched automatically. The bandwidth was programmed between 1 to 10Hz and the V_P varied accordingly using the mode-matching ASIC. For each bandwidth,

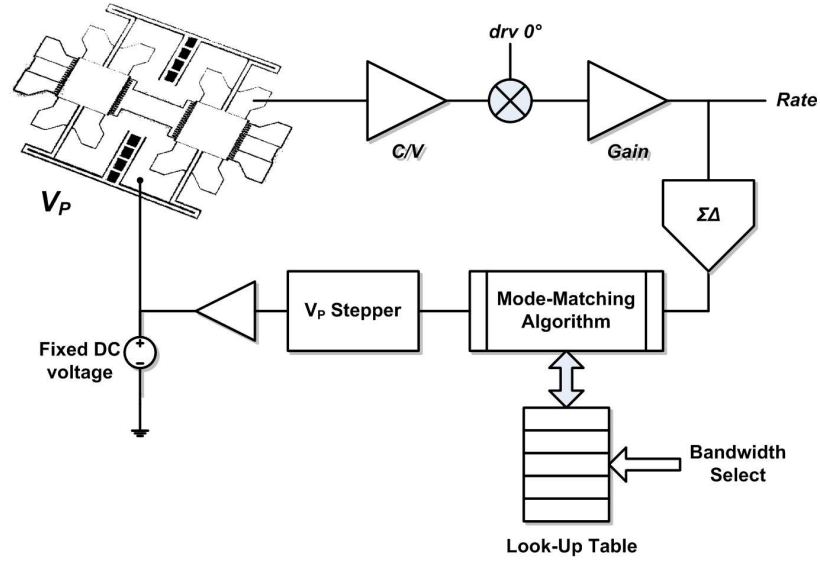


Figure 6.20: System implementation of programmable bandwidth control.

the scale factor was characterized using the same set up described in the previous section. The scale factors for the different bandwidths are shown in Fig 6.21. The microsystem bandwidth was increased from 1 Hz to 8 Hz by varying the V_P by 700mV about the value required for mode-matched condition.

A trade-off between gain and bandwidth is fundamental to analog circuit design. Therefore, it is not surprising that, in the control technique described here, the increase in bandwidth was achieved at the expense of mechanical gain.

For each bandwidth setting, the effective quality factor (Q_{EFF}) was measured using an Agilent 4395A network analyzer. A plot of measured scale factor vs. Q_{EFF} is shown in Fig 6.22. The linear fit proves that the microgyro scale factor varies linearly with Q_{EFF} , which corresponds with the theoretical analysis that forms the basis for using mode-matched operation to improve sensor performance.

Fig 6.23 shows the variation of the scale factor with frequency, validating that controlled splitting of the resonant modes is a viable alternative conventional closed-loop force-feedback topologies to increase bandwidth of microgyroscopes.

To the author's knowledge, this is the first reported scheme in literature where

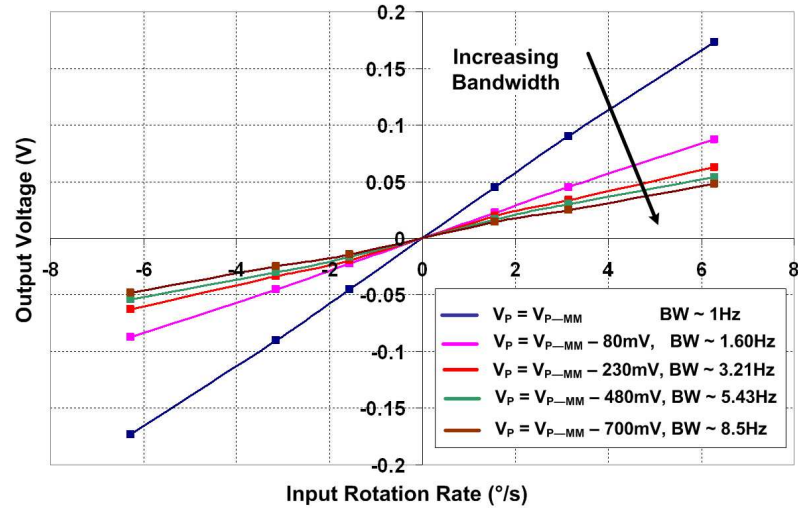


Figure 6.21: Scale factor measurement for V_P settings.

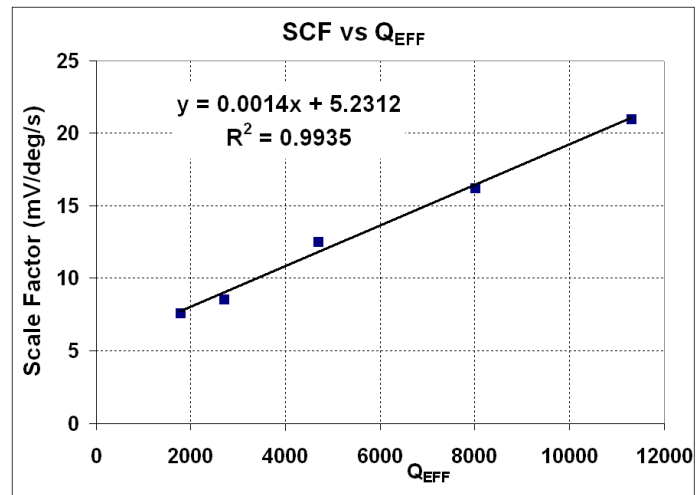


Figure 6.22: Scale factor vs. measured effective quality factor for different bandwidths.

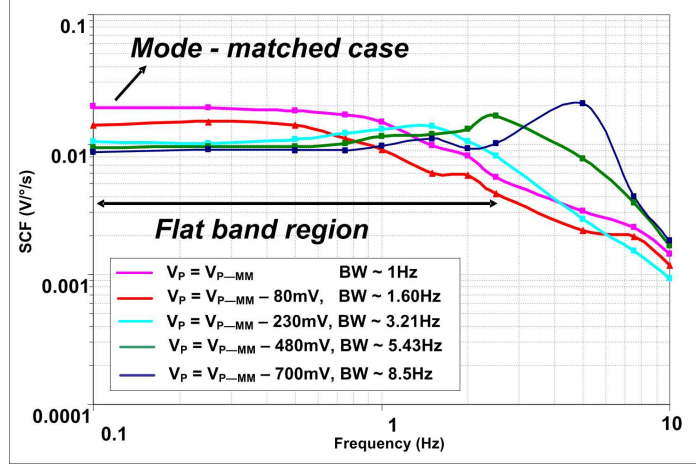


Figure 6.23: Scale factor vs. frequency for different V_P settings.

bandwidth control has been demonstrated by the use of a controlled mismatch of two high-Q resonant modes of a tuning fork gyroscope. Once mature MEMS fabrication processes are in place, the mechanical parameters of the micromachined structure and the tuning coefficient of the sense mode frequency will be known a-priori, allowing it to be coded along with the control algorithm. This will eliminate the need of the LUT before setting the bandwidth of the sensor.

6.8 Summary

The mode-matching ASIC is shown in Figure 6.24. The mode-matching algorithm is implemented in MATLAB, and is run on a PC which interfaces with the $M^2 - TFG$ via a dedicated mode-matching ASIC, as depicted in Fig 6.1. The blocks of the mode-matching ASIC are shown in Fig 6.1 and a die micrograph in Fig 6.24. The ASIC is fabricated in a $0.6\mu m$ two-poly three-metal (2P3M) CMOS process with a die size of $2.25mm^2$ and power consumption of $6mW$.

A summary of the $60\mu m$ thick SOI TFG and mode-matching ASIC parameters are listed in Table 6.1.

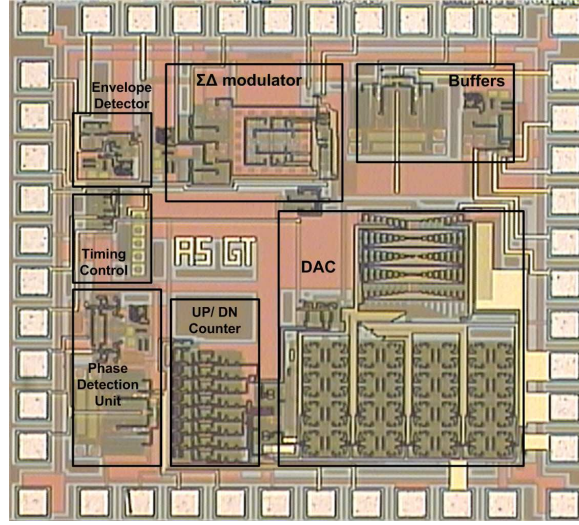


Figure 6.24: CMOS ASIC for gyroscope drive and sense channels.

Table 6.1: Summary of key Sensor and mode-matching ASIC parameters

Parameter	Measured Value
Sensor capacitive sensitivity	$80aF/\circ/s$
Amplitude of drive voltage applied	$130mV$
Range of minimum detectable ΔC (at 15kHz)	$0.02 - 2aF/\sqrt{Hz}$
Linear Dynamic Range of front-end of T-TIA	$104dB$
Rate sensitivity of Gyro + IC	$2mV/\circ/s$
Die Area	$2.25mm^2$
Total Power Consumption	$15mW$
Output voltage noise level at 10Hz	$15\mu V/\sqrt{Hz}$
Measured rate noise floor	$2.7^\circ/hr/\sqrt{Hz}$
Power Supply	$\pm 1.5V$

CHAPTER VII

BIAS DRIFT IN MICROMACHINED GYROSCOPES

7.1 *What is Drift?*

The output of a gyroscope in the absence of an input rotation rate is referred to as the gyro bias or the Zero Rate Output (ZRO). As explained in Chapter 1, gyro bias is analogous to DC offset in electronic amplifiers. Expressed in terms of angular rate, the bias is an accurate measure of the long-term stability of a gyroscope. Bias drift, the variation of gyro bias, is of concern to designers, and is the subject of this chapter.

Bias drift has systematic and random components. The systematic component of the drift is related to environmental conditions such as temperature, pressure, voltage fluctuations, and mechanical vibration. Often, these can be calibrated and compensated in a system. The other component, by virtue of being random, cannot be compensated and is therefore of concern. This random variation in bias, computed over specified finite sample time and averaging time intervals, is referred to as *bias instability*, and is related to the noise build up in a sensor.

Bias instability of a gyroscope forms the fundamental limit that determines if the sensor is capable of navigation grade performance. The lower the gyro bias instability, the smaller the angular error over time, and better the overall heading accuracy of the inertial navigation system. Typically, the accumulated error over time is corrected in the system by periodic calibration with an external reference, such as GPS. Dependence on external references such as GPS and beacons makes the gyro susceptible to electronic jamming and other electronic counter measures. A gyro with low bias instability allows for a longer time between calibrations, reducing the dependence on the external reference, and therefore, is better suited to military

applications.

Analysis of the bias drift of a micromachined gyroscope offers insights into the inherent noise mechanisms in the sensor. While significant characterization of bias drift of FOG's and RLG's has been undertaken, there have been few such studies related to drift in micromachined gyroscopes.

7.2 The Allan Variance Technique for Drift Characterization

Since bias drift is a long term average of the data, it cannot be specified in terms of a single data point. In addition, bias drift is a statistical phenomenon, and stochastic methods are used to model the it. Earlier, drift was specified as a single RMS number over time. However, this was a very conservative estimate, and did not offer any insight into the actual noise mechanisms. Subsequently, since bias drift is related to random noise in a system, the power spectral density (PSD) was used to characterize gyro drift. The output of the gyroscope in the absence of any rotation input is recorded in the time domain, and Fourier analysis yields the two-sided $\text{PSD}(S_{\Omega}(f))$.

A time-domain method that determines the angular error characteristics over time offers more insight for navigation applications, to determine the long-term stability of a gyroscope. One such method is the Allan Variance technique, which has been used extensively in recent times to study drift, both in FOG's and Coriolis vibratory gyroscopes. This technique, developed in the 1960's by David Allan [7], is a time-domain (TD) analysis, and was introduced to study frequency stability of oscillators. It helps us to understand the underlying random processes that give rise to data noise, and also enables us to identify the source of a given noise term in the collected data. The Allan Variance method can be applied to study the noise characteristics of any instrument. While using the method, it is important to realize that the uncertainty/ randomness in data are assumed to be generated by noise sources with specific characteristics. When applied to characterization of bias drift in gyros, it

represents the RMS random drift error as a function of averaging time used over the data.

The IEEE is undertaking several initiatives to standardize the specification and test procedures for CVG's [60]. Currently, the Allan variance technique is used as the standard for drift characterization in MEMS gyroscopes [8].

7.2.1 Computing the Allan Variance

Formally, the Allan Variance is defined as; one half the mean value of the square of the difference of adjacent time averages from a time series as a function of averaging time [61] and is expressed mathematically as:

$$\sigma^2(\tau) = \frac{1}{2(n-1)} \sum_i (y(\tau)_{i+1} - y(\tau)_i)^2 \quad (7.1)$$

where $\sigma(\tau)$ is the root Allan variance as a function of averaging time τ , n is the total number of data clusters, and y_i is the average value of the measurement in cluster i .

The procedure to compute the root Allan variance consists of repeatedly averaging the data over different clustering times. These clusters are sometimes referred to as *bins*. The iterative procedure used in this work to compute Allan variance is as follows:

- Step 1: Data Collection: Sample the bias data from the CVG at a specified sampling interval (τ_O) for a given period of time (usually for at least a few hours to gain any meaningful information).
- Step 2: Data Clustering: Take the long sequence of data and divide it into clusters based on an averaging time, τ . The τ will be a multiple of the initial sampling interval τ_O .
- Step 3: Data Averaging: Average the data in each cluster, i.e., sum up all the data points in each cluster and average them over the length of that cluster.

- Step 4: Compute variance: Take the difference in average between successive clusters, square this number, add them all up, and divide by the rescaling factor. Take the square root of the result: this gives a quantitative measure of how much the average changed at that particular value of averaging time. This term is referred to as the *Allan Deviation* or root Allan Variance.
- Step 5: Repeated averaging: Go back and increase τ , and repeat Steps 1 through 4. Keep doing this until there are at least 10 time clusters to average over - any less, and the results begin to lose their significance ¹.

Since both the PSD and Allan Variance are obtained from the same time domain data, it is natural to expect that there is a relation between the two. The Allan Variance can be computed from the two-sided PSD of the collected data [61], as given by:

$$\sigma_{\Omega}^2(\tau) = 4 \int_0^{\infty} S_{\Omega}(f) \frac{\sin^4(\pi f \tau)}{(\pi f \tau)^2} df \quad (7.2)$$

This can be interpreted as the Allan variance being directly proportional to the output noise power of the gyroscope when the output is passed through a filter with a transfer function $\frac{\sin^4(\pi f \tau)}{(\pi f \tau)^2}$. This particular transfer function arises due to the nature of the process used for computing the Allan Variance - i.e., the data clustering and averaging. The filter bandwidth depends on the sampling time τ . Therefore, by varying τ , different types of random processes, and therefore different properties associated with the noise, can be studied.

However, it must be noted here that we are referring to random variations of the gyro bias. If there is a direct correlation between bias and an external factor (such as temperature and polarization voltage), this can skew the data and hence

¹One of the disadvantages of the Allan variance technique is that the uncertainty of the variance estimate increases at large cluster times [61]

the Allan Variance can yield erroneous results. Therefore it is recommended [7] that any correlations in the data be removed (de-trending) before performing an Allan Variance analysis. This is why most navigation systems use an adaptive high pass filter to remove long-term correlations in the data. An explanation of the filtering performed is presented in Appendix D.

7.2.2 Noise components in a gyroscope

Once the repeated clustering and averaging described above is completed, the values of the root Allan variance are plotted as a function of averaging time. Fig 7.1 has been adapted from [7] and plots the Allan variance curve that is typical for any CVG at rest.

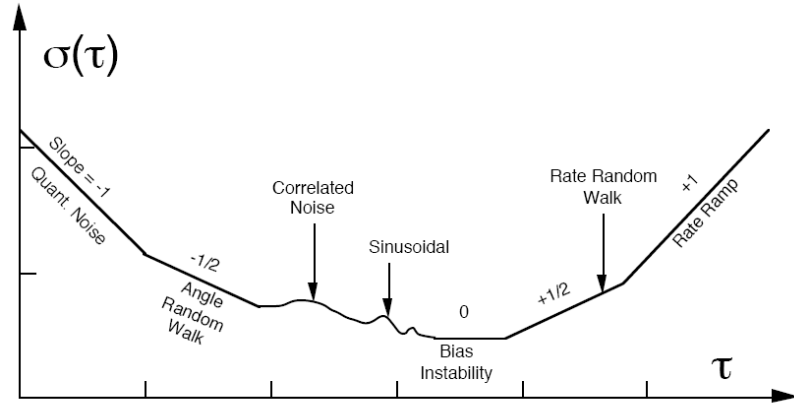


Figure C.8— $\sigma(\tau)$ Sample plot of Allan variance analysis results

Figure 7.1: Typical Allan variance plot for a gyroscope showing the portions corresponding to the different noise sources.

The time domain data from the CVG contains contributions from different noise terms. It has been observed and verified that each of the noise terms are correlated with different averaging times (τ), and hence correspond to different portions on the Allan Variance curve. The Allan Variance curve allows for easy identification of the various random processes that exist in the gyroscope output, and is therefore the preferred means for gyroscope drift analysis.

From Fig 7.1, it is seen that there are 4 distinct regions in the Allan variance curve, which correspond to the following noise terms:

1. Quantization Noise
2. Angle Random Walk
3. Bias Instability
4. Rate Random Walk

The random processes that contribute to these noise terms can be assumed to be uncorrelated (i.e., statistically independent). The total Allan variance at a given sampling time τ can be obtained by the root-mean-square (*rms*) sum of the magnitude of each of these components at that τ , as:

$$\sigma_{Total}^2(\tau) = \sigma_{Quantization}^2(\tau) + \sigma_{ARW}^2(\tau) + \sigma_{Bias-Instab.}^2(\tau) + \sigma_{RRW}^2(\tau) \quad (7.3)$$

7.2.3 Quantization Noise

The quantization noise is represented by the portion of the Allan variance curve that has a slope of -1 (i.e., is proportional to $1/\tau$), when plotted on a log-log scale. The expression for the quantization term coefficient (Q_N) is given by:

$$\sigma_{Quantization}^2(\tau) = \frac{Q_N}{\tau^2} \quad (7.4)$$

The source of this noise is the sampling at the gyroscope output to record the value of the bias over time. Since the sampling is at a relatively higher frequency than other gyro time constants, in the time domain, this noise term corresponds to small values of τ . Quantization noise is more of an issue in gyroscopes with direct digital read-out as compared to analog output CVG's.

7.2.4 Angle Random Walk

The angle random walk (ARW) is a measure of the angular error build up with time that is due to *white noise* in angular rate. In FOG's and RLG's, the source of this noise is photon emission, while in CVG's, it is the Brownian noise of the mechanical structure. This component is referred to as a *random-walk* because it is a non-stationary random process (like all noise is!) with expected mean zero, but with a mean square error that grows linearly with time [62]. Being white, in the frequency domain, this component corresponds to the flat region of the PSD plot. Therefore, from Eq.(7.2), in the root Allan Variance plot, the ARW noise term is represented by the portion of the curve proportional to $\tau^{-1/2}$, or which has a slope of -1/2 on a log-log scale.

$$\sigma_{ARW}^2(\tau) = \frac{N}{\tau} \quad (7.5)$$

where N is the ARW coefficient. The value of the ARW coefficient (N) is obtained by fitting a straight line to the portion of the root Allan variance plot that varies as a function of $\tau^{-1/2}$. N/60 gives the magnitude of the ARW component in the gyroscope output, yielding a measure of the total white noise. This noise error term is typically expressed in $^{\circ}/\sqrt{hr}$ and is an accurate indicator of the short term stability of the system. Often, the ARW is converted to noise density by multiplying its value by 60, Eq.(1.4), and expressed in $^{\circ}/hr/\sqrt{Hz}$. Most data sheets specify the noise of the microgyroscope system in terms of its noise density. It must be noted that the noise density of the sensor plus electronics is its $TNE\Omega$ Eq.(1.1).

It is interesting to analyze what the ARW translates to an actual navigation system that is periodically calibrated (i.e., aided) by GPS. An angular random walk of $0.003^{\circ}/\sqrt{(hr)}$ indicates that the angular error (uncertainty) due to random walk (unaided) is 0.001° after 6 minutes (1σ value). The angle random walk is very important for the accuracy of north seeking, because if the random walk decreases

by 2, then the needed duration for north seeking decreases by a factor of four (if the resolution of the gyro is high enough). Being a measure of short term system stability, the ARW is significant at start-up, as it can prevent the initial biases of the system from being measured accurately.

7.2.5 Bias Instability

The random process that contributes to bias instability has a $1/f$ PSD, and therefore, is referred to as the flicker rate noise. The root Allan Variance curve for this noise term shows a flat region - which corresponds to the minimum attainable bias drift. It represents the best bias stability that could be achieved for a given gyro, assuming that bias averaging takes place at the interval defined at the Allan Variance minimum. In data sheets, the value of the Allan variance curve that corresponds to this minimum is quoted as the bias drift of the gyro.

7.2.6 Rate Random Walk

The rate random walk (RRW) represents the drift rate error build-up with time that is due to white noise in angular acceleration. The exact origins of this noise are not yet known, but consist of random processes with very long correlation times. The PSD is associated with a $1/f^2$ characteristic, and the Allan variance corresponding to this noise term is given below:

$$\sigma_{RRW}^2(\tau) = \frac{K^2}{3}\tau \quad (7.6)$$

where K is the rate random walk coefficient. This indicates that rate random walk is represented by a slope of $+1/2$ on the log-log plot of $\sigma(\tau)$ vs τ , where K is usually in $^{\circ}/hr^2/\sqrt{Hz}$.

7.3 Relationships between noise sources, drift and Allan variance

To obtain a better understanding of how noise sources with different spectral characteristics are mapped on to the root Allan variance plot, a SIMULINK model for the drift sources in a generic system was implemented. Fig 7.2 shows the SIMULINK model for the system with uncorrelated white and flicker noise sources. The flicker noise term and long-term random variations are obtained by passing white noise through an integrator $(1/s)^2$.

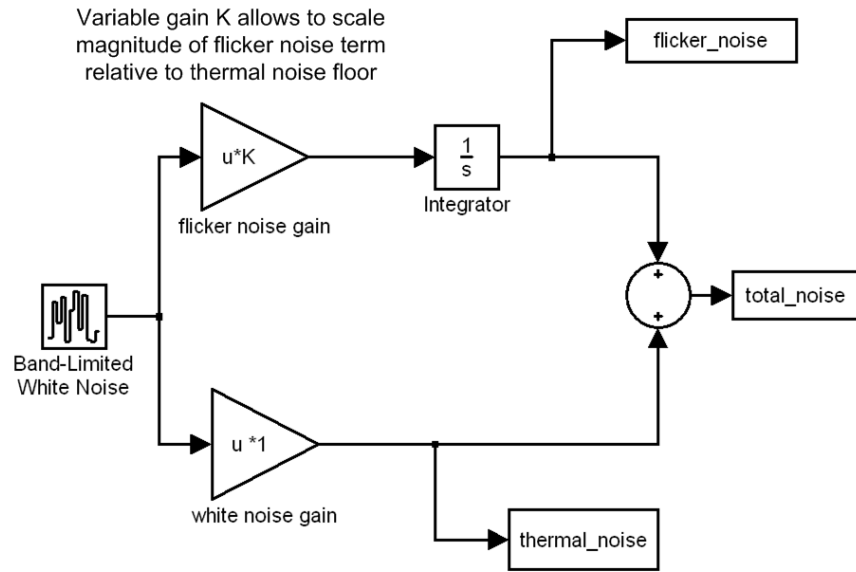


Figure 7.2: SIMULINK model for noise sources that contribute to the drift in a gyroscope system.

To ensure that the noise sources are truly uncorrelated, the white noise generator block in Fig 7.2 uses a new randomly generated seed for white noise generation. The amplitude of the flicker noise is variable to investigate the impact of the flicker noise corner frequency (f_c) on bias stability and root Allan variance. For a given slope,

²This model provides a purely qualitative analysis and does not reflect actual noise magnitudes. However, the model is scalable and will provide fairly accurate quantitative results if the exact parameters (i.e., thermal noise floor and flicker noise corner frequency) of the system being analyzed are known.

increasing the magnitude of the flicker noise term implies a higher $1/f$ noise corner frequency. On simulation, this SIMULINK model provides a time domain waveforms for the different noise sources on which an Allan variance analysis can be performed. However, it is intuitive to look at the power spectral density (PSD) of the output of the SIMULINK model. The power spectra for the thermal noise, flicker noise, and total noise floor of the system are shown in Fig 7.3. Increasing the magnitude of the flicker noise term shifts the $1/f$ corner frequency higher. The two main regions of the PSD plot are evident: flicker noise dominated low-frequency regions and thermal noise dominated high frequency regions.

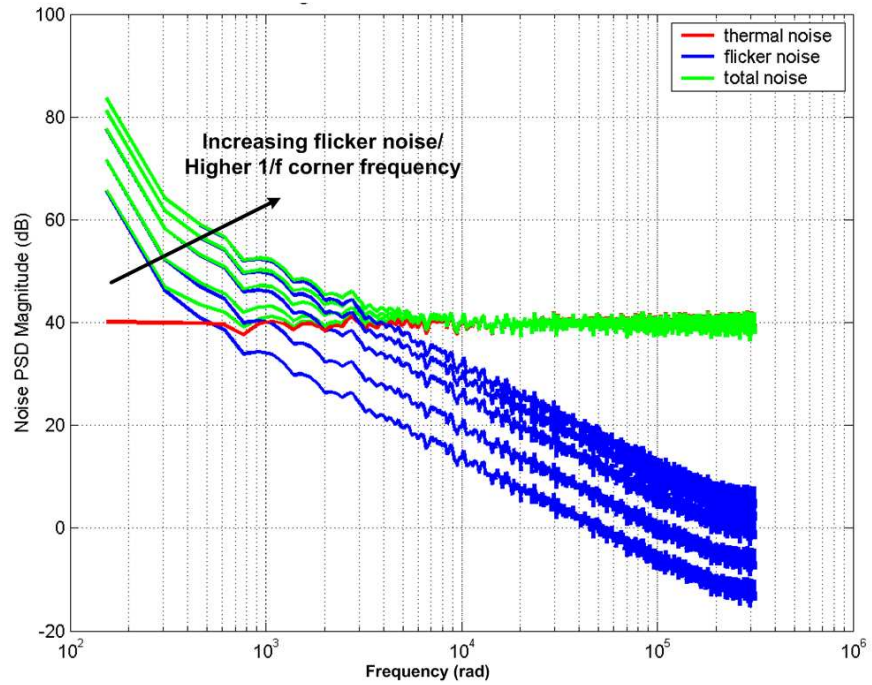


Figure 7.3: Power spectral density plots for the flicker, thermal and total noise generated by the SIMULINK model.

The Allan variance analysis was performed on the total noise obtained from the SIMULINK model. The results are shown in Fig 7.4, along with the root Allan variance for the case of the system with no flicker noise. The flat portion of the root Allan variance curve (which corresponds to system bias instability) is strongly

correlated with the amount of flicker noise in the system.

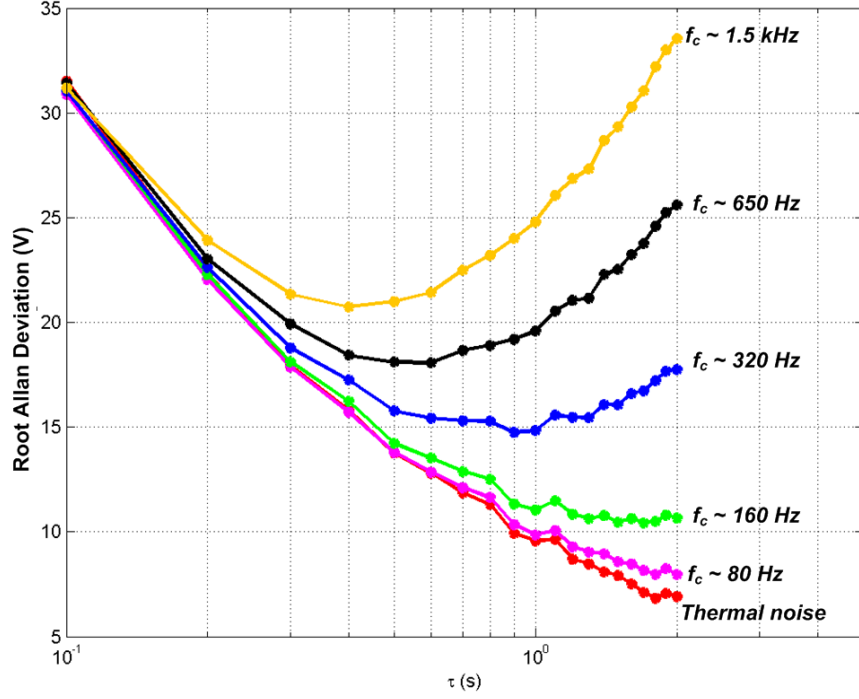


Figure 7.4: Root Allan variance of total system noise for different flicker noise corner frequencies.

Therefore, a system with higher flicker noise exhibits larger bias instability or drift. Since the thermal noise floor is relatively constant, there is no significant change in that portion of the root Allan variance curve corresponding to the ARW.

7.4 Drift in the $M^2 - TFG$

In Chapter 6, it was shown that once matched, the $M^2 - TFG$ remains stable over time. The Allan variance analysis performed on this data provides a methodology to quantify the stability or instability over time. The $M^2 - TFG$ was locked into drive resonance using the electromechanical drive loop, and the amplitude of the forcing voltage is adjusted to provide maximum proof-mass drive amplitude. It must be noted that since the bias drift is a DC phenomenon, nonlinearity at large input rotation rates is not an issue.

The DC value of the rate output was sampled using an Agilent 34401A digital multimeter. The root Allan variance ($\sigma(\tau)$) was computed for various sampling times (τ), using the MATLAB code shown in Appendix A. The magnitude of the various noise components in the gyroscope were extracted by a least-squares curve fit. The expression that is used to curve-fit $\sigma(\tau)$ vs. τ is given by Eq.(7.7), which follows from the previous section.

$$\sigma(\tau) = Q_N\tau^{-1} + N_N\tau^{-0.5} + B_N + K_N\tau^{+0.5} \quad (7.7)$$

The curve-fitting routine is written in MATLAB, and uses the Levenberg-Marquardt technique [63] to perform a least-squares fit.

7.4.1 40 μm thick SOI TFG

Fig 7.5 shows the root Allan variance plot for a 40 μm thick SOI TFG that was discussed in Chapter 4. The mode-matching of this device was performed by manually varying the V_P as shown in Fig 5.5 and is the sensor reported in [49] and [64]. The TFG was locked into drive resonance and the root Allan variance was measured for the time data that was collected over a period of 12 hours.

The slope at short cluster times (τ) yields the angle random walk (ARW), which is a measure of the white noise in the system. The ARW is $0.045^\circ/\sqrt{hr}$, which corresponds to a measured noise floor of $15\mu V/\sqrt{Hz}$ ($-96dBV/\sqrt{Hz}$) over the signal bandwidth (1 - 10Hz) for the entire microsystem. The output-referred total equivalent noise density (MEMS plus electronics) is therefore $2.7^\circ/hr/\sqrt{Hz}$. The minimum of the Allan variance plot gives the value of the bias drift of the system, which for the 40 μm case is $1^\circ/hr$.

7.4.2 60 μm thick SOI TFG

Fig 7.6 shows the root Allan variance plot for a 60 μm thick SOI TFG that was discussed in Chapter 6 and is used in [65]. The TFG was mode matched automatically

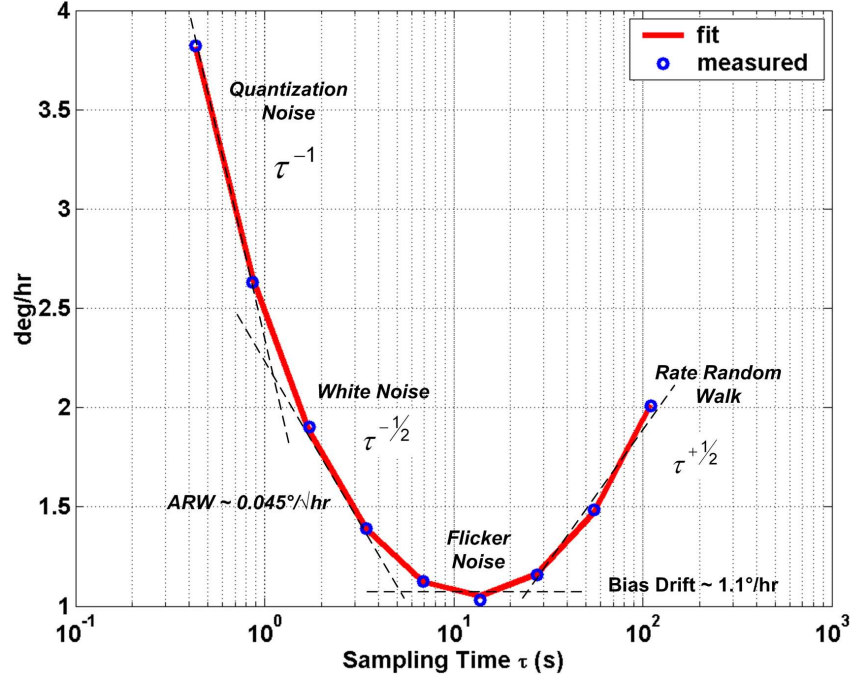


Figure 7.5: Allan Variance plot of the $40\mu m$ TFG.

using the scheme proposed in Chapter 5. The random component of $M^2 - TFG$ drift is characterized using the Allan variance after compensating/ de-trending external deterministic factors such as V_P variation and vibration. The procedure is explained in Appendix D.

As in the previous case, the ARW is given by the slope of the curve-fit that is proportional to $\tau^{-0.5}$, and for this case is measured to be $0.003^\circ/\sqrt{hr}$. This corresponds to a $TNE\Omega$ of about $0.2^\circ/hr/\sqrt{Hz}$, which is slightly higher than the theoretical total noise floor. The bias drift for this case was measured to be $0.15^\circ/hr$. This is about an order of magnitude better than commercially available gyroscopes [14], and is one of the lowest recorded for a silicon vibratory gyroscope.

7.4.3 Drift vs. Temperature

As discussed in Chapter 6, once matched, the drive and sense resonant modes track each other with temperature, and hence mode-matching is maintained. The bias

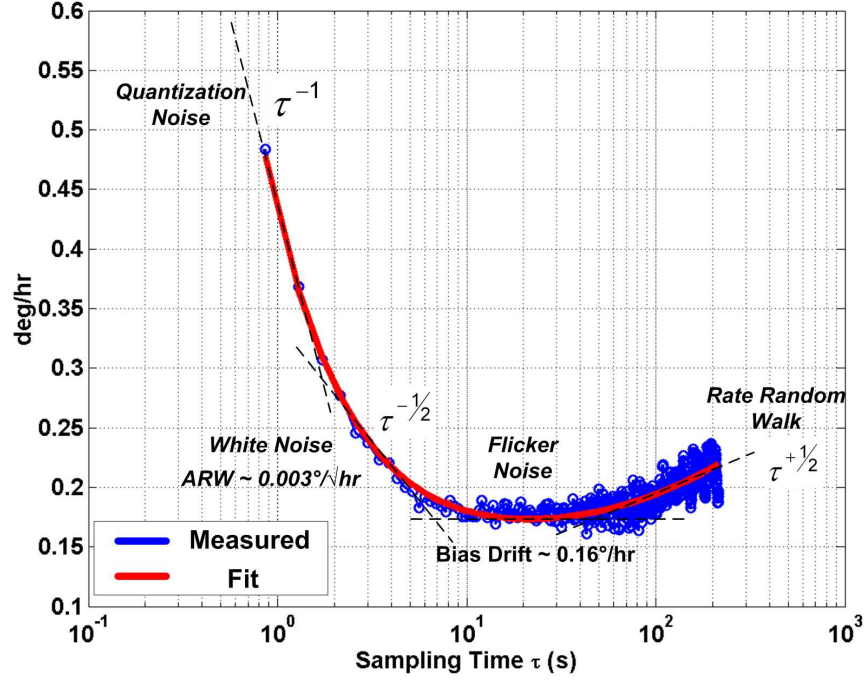


Figure 7.6: Allan Variance plot of the 60 μ m TFG.

drift of the $M^2 - TFG$ was measured at different temperatures to study the effects of temperature on the drift, as shown in Fig 7.7.

As seen from Fig 7.7, the bias drift degrades with increasing temperature. While the bias drift decreases to 0.08°/hr at 5°C, it degrades to 0.5°/hr at 50°C. This temperature dependence of the bias drift is attributed to thermoelastic damping which causes Q_{EFF} to degrade at elevated temperatures [49]. Despite this degradation, the bias drifts measured are at least two orders of magnitude better than commercially available MEMS gyroscopes [14].

From the above discussions, it is seen that the bias drift is of the order of 0.1°/hr. A common misconception is that this translates to the lowest measurable angular rate! This is not so. It must be noted that in practice, it is impossible to measure an input signal that is equal to the system noise floor. Any meaningful signal that can be measured must be at least 2X or 3X times larger than the number given by this noise floor.

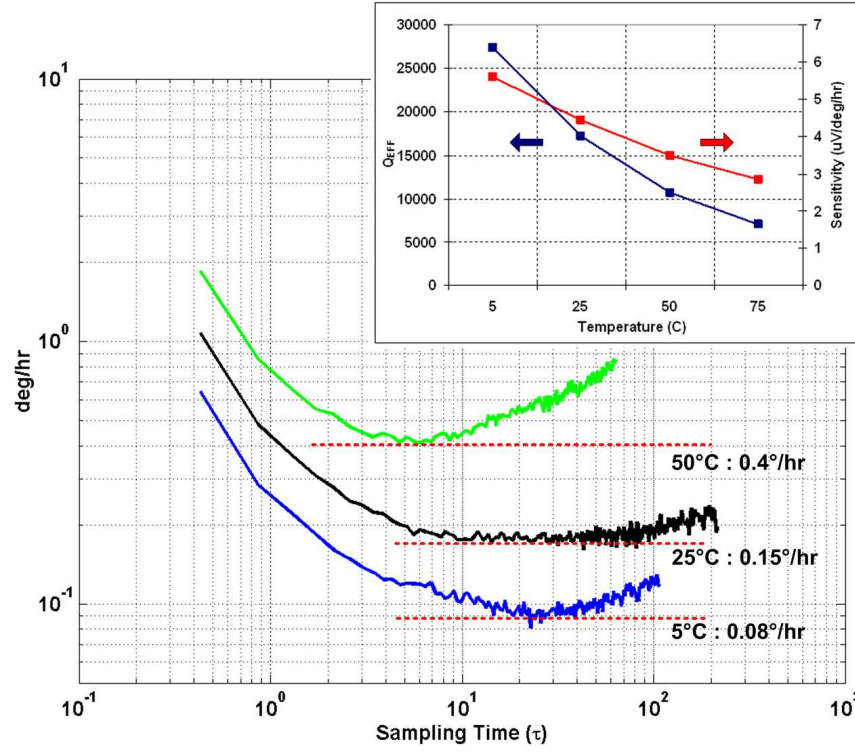


Figure 7.7: Root Allan Variance plot of the $M^2 - TFG$ for different temperatures.

7.4.4 Drift vs. Bandwidth

Microsystem bandwidth was set electronically by the controlled mode-splitting described in Chapter 6, and the bias drift was measured for each scale factor/bandwidth setting of Fig 6.23. An Allan variance analysis was performed for each bandwidth setting using the corresponding scale factors. As seen in Fig 7.8, the bias drift varies inversely with scale factor, and corresponds to the gain-bandwidth trade-off inherent to any system.

7.5 Guidelines to reduce drift in micromachined gyroscopes

Analyzing the long-term stability and drift of micromachined gyroscopes has led to the analysis of factors that affect the bias drift in CVG's. Once the main factors that affect bias drift are known, techniques to reduce the drift of micromachined gyroscopes can be outlined. The research conducted as part of this work has led to

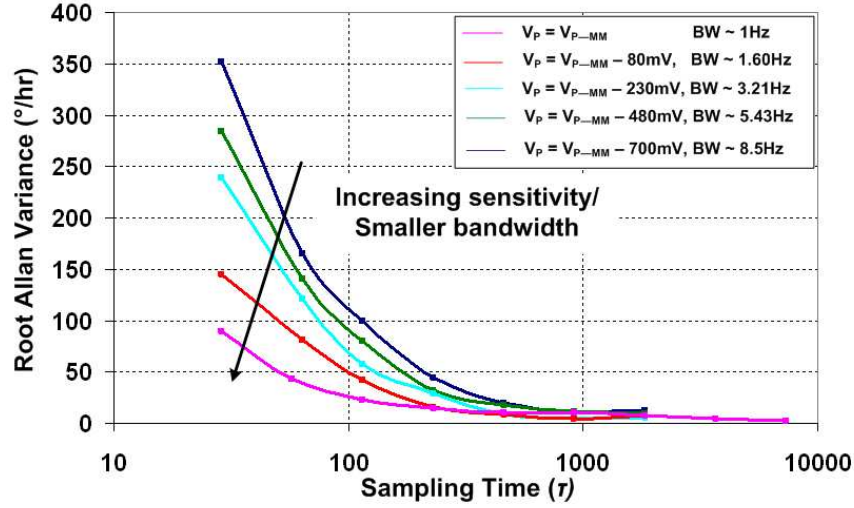


Figure 7.8: Root Allan Variance plot of the $M^2 - TFG$ for different sensor bandwidths.

the development of the following guidelines to reduce bias drift:

1. Bias drift has been shown to depend on the noise build-up in the sensor. Therefore, techniques that lower the total system noise floor (Brownian plus electronic) also result in superior gyroscope bias drift. Hence, in order to obtain a sensor with inherently low bias drift, one must first design a sensor with a sufficiently low system noise floor (i.e., ARW). Increased mass is key to lowering the noise floor as well as the bias drift.
2. Gyro bias drift has been shown to depend significantly on the Q_{EFF} . Therefore, it is essential to design mechanical structures with inherently high quality factors in both the drive and sense modes. Additionally, circuit topologies like transimpedance amplifiers (TIAs), that do not excessively load the mechanical quality factors, must be adopted³.

³Bias drift in a gyroscope can intuitively be likened to phase noise in an oscillator. Hence techniques that reduce the phase noise of a micromechanical resonator can also be applied to decrease drift of a gyroscope.

3. Increasing the capacitive sensitivity of the sensor directly reduces the bias drift.

This is apparent from a comparison of the TFG's fabricated in $40\mu m$ -thick SOI and $60\mu m$ -thick SOI. The $60\mu m$ TFG had a maximum scale factor of about $88mV/^{\circ}/s$ and recorded a bias stability of $0.3^{\circ}/hr$, while the $40\mu m$ TFG had a maximum scale factor of only $24mV/^{\circ}/s$, and recorded a bias stability of $1^{\circ}/hr$. Both TFG's had comparable Q_{EFF} . The improvement in bias drift is clearly due to the improvement in capacitive sensitivity, owing to a higher aspect ratio in the $60\mu m$ -thick sensor prototype.

4. The noise considerations imply that a low-bias drift gyroscope must have ultra-low noise interface circuits. While low-noise front-ends are necessary to ensure a low minimum detectable capacitance, the flicker noise of subsequent stages is also of concern. The bias drift of the gyroscope is given by the flat portion of the Allan variance curve, and quantifies the flicker noise in the system, as discussed previously. Large flicker noise due to electronics therefore results in a direct increase in bias drift. Decreasing the flicker noise corner frequency of the interface electronics can significantly improve bias stability. It has been reported that flicker noise of the output stages contribute significantly to the measured bias drift [14], which is why the Analog Devices gyroscope uses bipolar output stages. Hence, low-noise techniques that mitigate flicker noise, like chopper stabilization or CDS, must be used from the output stages as well. Further, since BJT's and JFET's exhibit significantly lower flicker noise corner frequencies, these must be used in the sense signal chain, if available in a process. Lateral BJT's are available even in a standard CMOS process, and must therefore be exploited. For the measurements obtained in this work, the final output stage was a discrete JFET op-amp that had low voltage and current noise [66].

5. One of the main motivations of using the Allan variance technique to characterize the long-term stability of a gyro is the ability of the method to separate out the contributions of the various noise components. Before performing an Allan variance technique, any trend (or verifiable effects arising from the test set-up) in the recorded data must be removed, as this can skew any statistical analysis. Post-processing of the acquired data includes the quick look, data editing, trend removal, digital filtering of other deterministic signal (i.e., periodic) and other pre-whitening signal processing [61]. One such post-processing step that has been employed on some sets of data is to apply a digital high pass filter to remove the bias fluctuations caused by variations in the polarization voltage, V_P . This can eliminate unwanted error sources, and provides an accurate representation of the bias drift of the sensor itself.

7.6 Comparison of drift from inertial grade gyroscopes

It is worthwhile to compare the drift performance that has been reported as part of this research with current state-of-the-art microgyroscopes and IMU's. The values of the bias instability and the corresponding averaging times at which the Allan Variance curve reaches a minimum (i.e., settles) are of interest, and will be compared in this section. The comparison of bias drift and settling time is done over different technologies - macromachined bulk gyroscopes like the HRG, other MEMS rate sensors, and fiber-optic gyroscopes (which rely on the Sagnac effect for rotation rate sensing).

As explained in the previous section, techniques that results in low $TNE\Omega$, also result in lower bias drifts. Therefore, it is evident that lower absolute values on the Allan variance curve will translate into smaller cluster-times that correspond to the bias instability. Simply put, lowering the over-all noise of the system (sensor plus electronics) will lower the cluster time at which bias drift can be measured.

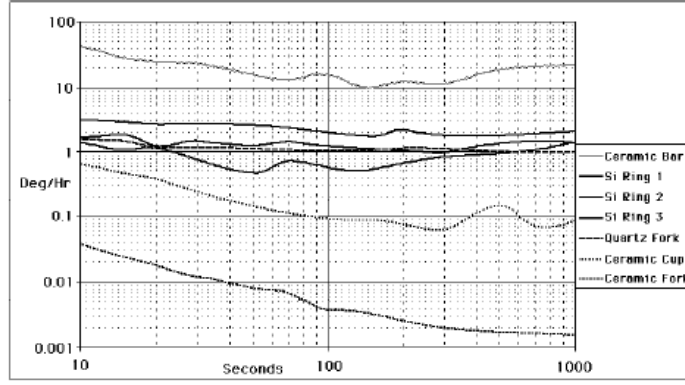


Figure 7.9: Comparison of drift from bulk macromachined and MEMS gyroscopes of different configuration.

The work presented in [11] compared the effects of gyroscope configuration on bias drift. However, this comparison was restricted to bulk-implementations made from silicon, quartz, and ceramic. Fig 7.9 shows that while the bias drift numbers attain sub-degree per hour values, the settling time is in the order of 100 seconds. Interestingly, ceramic and macromachined quartz fork designs offer the best bias drift performance.

The silicon MEMS ring gyro from Silicon-Sensing/BAE Systems measures a bias drift of about $2^\circ/hr$ at a settling time of approximately 50 seconds [67], as shown in Fig 7.10.

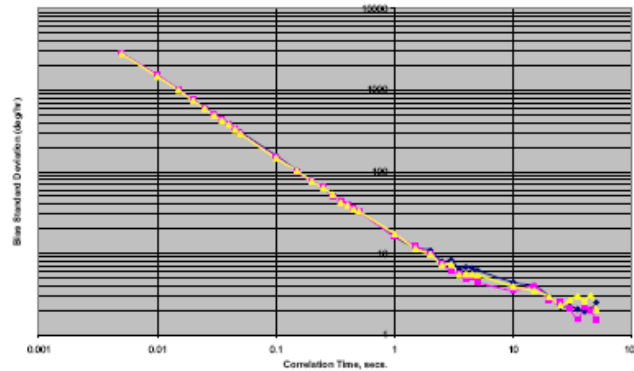


Figure 7.10: Bias drift plot from VSG series of rate sensors from Silicon-Sensing.

The ADXRS series of gyroscopes from Analog devices [14] are single-chip rate sensors targeted toward automotive applications. The bias stability of these devices is measured to be $50^\circ/hr$, as shown in Fig 7.11, and the recorded settling time is in the order of 10 seconds.

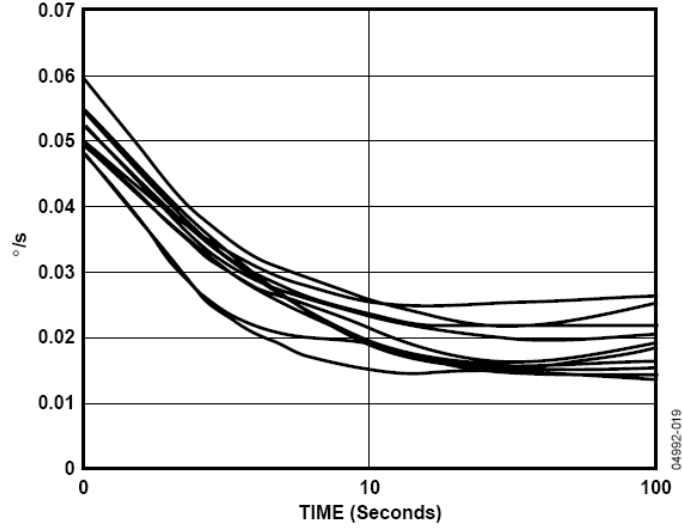


Figure 7.11: Bias drift plot from ADXRS series of rate sensors from Analog Devices.

Automotive-grade sensors must have a larger sensor bandwidth as compared to navigation-grade devices. This implies that the settling time at which the root Allan variance plot reaches a minimum must be small (in the order of 1 - 10 seconds). The SAR-10 sensing element from Sensor-Nor (Norway) [68], similar to the clover-leaf gyro from JPL, is a micromachined Silicon 'butterfly' gyro aimed for the automotive market. Most of the signal detection and processing are done in the digital domain to eliminate flicker noise. As shown in Fig 7.12, the ARW for this sensor was $0.003^\circ/\sqrt{sec}$, and the bias drift was measured to be $3.2^\circ/hr$.

Robert Bosch GmbH has performed extensive research on the development of angular rate sensors for automotive applications [69], especially for use in ESP modules. The DRS-MM3 angular rate sensor exhibited a bias drift of $1.2^\circ/hr$ within a settling time of about 100 seconds, as shown in Fig 7.13.

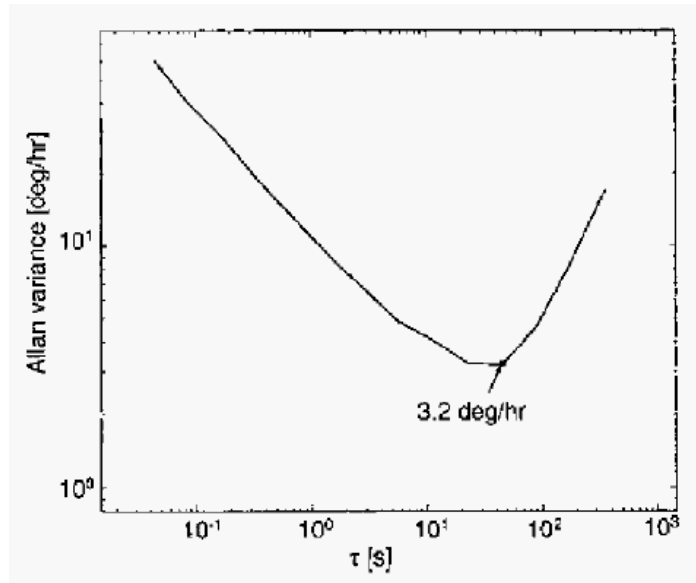


Figure 7.12: Bias drift plot from the SAR-10 gyroscope Imego/ Sensor-Nor.

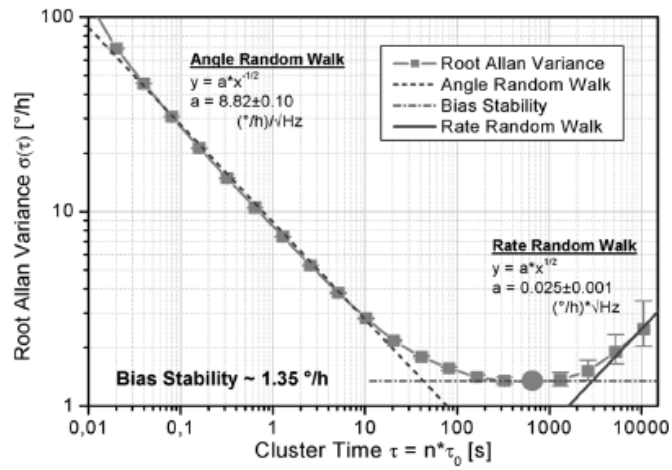


Figure 7.13: Bias drift plot from the DRS-MM3 gyroscope Bosch.

The data presented in [69] clearly shows a section of the time domain waveform recorded from the DRS-MM3 module for use in Allan variance computation. While the rms noise measured from the sensor in the time domain is typically in the order of $100^\circ/hr$, the actual sensor bias drift obtained from the Allan variance analysis is $1.2^\circ/hr$.

Next, the bias drift and settling parameters from 3 different fiber-optic gyroscopes are compared. Fig 7.14 shows the measured fiber-optic gyroscope Allan variance from one of the VG700 series IMU's. The red lines in the graph below give the error bounds, and the blue line is the measured Allan variance. The lowest recorded bias stability is about $10^\circ/hr$, obtained at a settling time of 10 seconds.

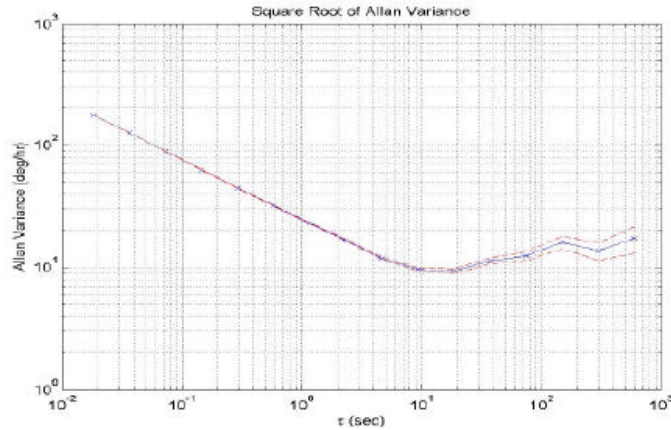


Figure 7.14: Bias drift plot from the VG700 series of gyroscopes Cross-Bow.

Fig 7.15 and Fig 7.15 show the root Allan variance from fiber-optic gyroscopes manufactured by the Andrew Corporation [70] and the Fibersense Technologies [12] respectively. In Fig 7.15, the Allan variance in deg/hr is plotted as a function of sampling time in hours. This gives a settling time in the order of several minutes to attain sub-degree per hour bias drift.

The FOG's manufactured by Fibersense Technologies use a topology where the sense coil is separated from other gyro elements. This improves the bias drift and reduces effects of external vibrations. Again, the bias drift of $0.08^\circ/hr$ has been

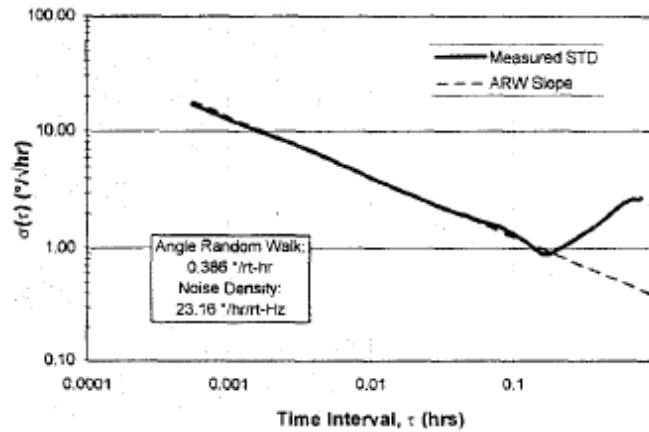


Figure 7.15: Bias drift plot from the FOG's developed by Andrew Corporation.

achieved at a settling time of approximately 500 seconds.

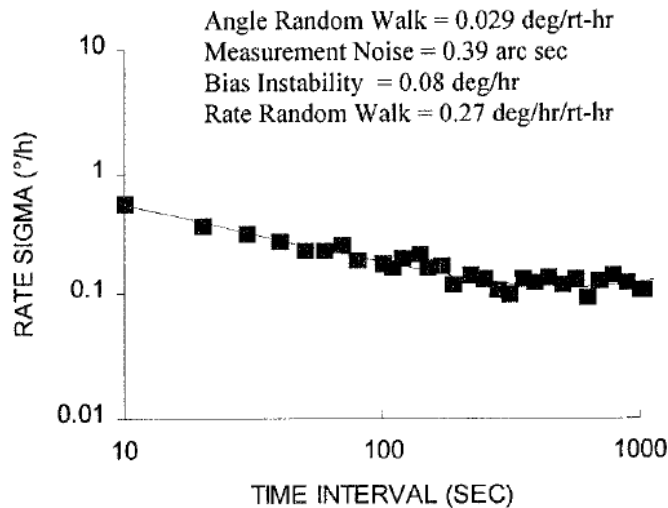


Figure 7.16: Bias drift plot from the FOG developed by Fibersense Technology.

The objective of incorporating the above graphs was to provide a platform to compare gyroscope bias drift and settling behaviour. The key point is that though MEMS gyroscopes operate on a fundamentally different principle as compared to optical gyroscopes, the bias drifts reported during the course of this research prove that MEMS gyroscopes are comparable to their optical counterparts.

CHAPTER VIII

CONCLUSIONS AND FUTURE WORK

8.1 Technical Contributions

In this work, we describe the development of control methodologies, and the design and characterization of CMOS integrated circuits and systems for high performance MEMS gyroscopes. The work has resulted in the following contributions to the body of technical knowledge available in this field:

1. The complete system electronics required for operating of a microgyroscope was implemented and interfaced with a high-Q silicon-on-insulator (SOI) tuning fork gyroscope (TFG). An electromechanical drive loop was implemented to start up and sustain oscillations along the x -axis of the MEMS structure. A synchronous demodulation technique was implemented for rotation rate sensing. Quadrature nulling and automatic mode-matching were also addressed. The circuits and systems developed as part of this research have enabled leveraging the inherently high mechanical gain of resonant systems, and have led to the demonstration of the first sub-degree-per hour MEMS gyroscope. The lowest recorded bias stability obtained from a combination of the sensor plus electronics was $0.1^\circ/hr$ - two orders of magnitude better than commercially available MEMS gyroscopes.
2. An optimized electrode configuration for the MEMS TFG was developed and implemented. A central comb-drive electrode for applying the AC drive excitation was added to ensure that the proof-masses were excited anti-phase to each other, thereby preventing lock-in of the electromechanical oscillator to spurious mechanical modes of the sensor. Further, dedicated quadrature nulling electrodes were implemented, which enabled rotational torques to be applied to

the TFG proof-masses, thereby reducing any misalignments. This electrode scheme reduces the quadrature error in the TFG structure, and allows for near-perfect mode-matching of the drive and sense resonant frequencies of the TFG.

3. The use of transimpedance amplifiers (TIA) for motional current detection from microgyroscopes was investigated. A low-noise CMOS T-network-based TIA was developed and interfaced with the MEMS TFG. The input referred current noise of the T-network TIA was measured to be as low as $100fA/\sqrt{Hz}$, which corresponded to a minimum detectable capacitance of $0.04aF/\sqrt{Hz}$. Using this TIA, transimpedance (TZ) gains of as large as $20M\Omega$ can be implemented on-chip, in an area and power efficient manner. The T-network TIA provided a dynamic range of 104dB in a bandwidth of 10Hz, and consumed $400\mu W$ of power.
4. A CMOS ASIC, consisting of the drive loop and sense channel for the TFG, was developed in a 0.6μ CMOS process. The drive loop uses the T-network TIA in a high gain configuration to provide sufficient loop gain to start up and sustain electromechanical proof-mass oscillations. The sense channel uses the T-network TIA as the front-end for motional current detection, and CMOS Gilbert cells to perform synchronous demodulation. The TFG was interfaced with this CMOS ASIC and the measured rotation rate sensitivity was $2mV/^\circ/s$.
5. In this work, mode-matching was used to improve the performance of MEMS angular rate systems to navigation-grade levels. The importance of operating a microgyroscope in a mode-matched condition (i.e., 0 Hz frequency split between the drive and sense mode frequencies) in order to leverage the inherently high mechanical quality factor of the sense mode has been analyzed. Mode-matching has been shown to improve the noise floor as well as bias drift of a microgyroscope by orders of magnitude. A novel automatic tuning strategy is

developed for the TFG. The tuning scheme utilizes the often ignored residual quadrature error to determine mode separation and sensor sensitivity. The real-time tuning scheme has been proposed and implemented, that allows mode-matching of the drive and sense resonant modes of the TFG in a fraction of the time and power, as compared to other schemes for microgyroscopes. Zero separation between the drive and sense frequencies is detected as a maximum in the residual zero-rate-output (ZRO) of the gyroscope.

6. A CMOS architecture was developed for implementing the automatic tuning algorithm. ZRO amplitude was measured using a CMOS level detector. The ZRO level was converted to a low-resolution pulse width modulated bit-stream using a first order $\Sigma\Delta$ modulator. The bit-stream was read into a PC that does the decimation and runs the automatic mode-matching algorithm. The algorithm determines the direction in which to vary the polarization voltage (V_P) to enable appropriate electrostatic spring softening. Once the maximum in ZRO is detected, the V_P value is held constant. The 0.6μ 2P3M CMOS ASIC consumed 6mW of power, and occupied an area of $2.25mm^2$.
7. The proposed automatic CMOS mode-matching scheme can also be extended to improve the bandwidth and the dynamic range of MEMS gyroscopes. The sensor bandwidth is given by the separation between the drive and sense frequencies. Therefore, based on the ZRO level, a controlled separation between the drive and sense resonant frequencies can be set, and maintained by the proposed CMOS architecture. The bandwidth control strategy has been experimentally verified and the sensor bandwidth can be controlled between 1 to 10Hz. Further, experimental verification of the technique demonstrates the feasibility of using a controlled mode separation to extend the dynamic range of the gyroscope, as compared to conventional force-feedback closed loop systems.

8. Finally, this work studied and analyzed long-term stability of a gyroscope with regards to its scale factor, bandwidth, bias drift and resolution. The impact of different noise sources such as flicker- and white-noise on the drift of a gyroscope were modeled and analyzed. Based on the analyses and measurements made, techniques to mitigate random bias drift of microgyroscopes are proposed.

8.2 *Future Work*

8.2.1 Automatic quadrature trimming

Currently, a manual trimming procedure is performed post-fabrication to determine the voltages necessary to null the quadrature error. In order to be commercially viable, this quadrature nulling must be automated. Automation will significantly be simplified once mature MEMS fabrication processes are in place, since process variations can be statistically modelled. However, there is no definite means of determining *a priori* the amount of misalignment of the proof-masses. Therefore, a calibration routine must be performed to determine which of the electrodes enables maximum quadrature nulling.

If varying the voltage on a particular quadrature nulling electrode allows significant sense frequency shift during V_P ramp-up, it can be inferred that, that electrode is particularly suited for quadrature nulling. This is repeated for all the 4 quadrature nulling electrodes and a sensitivity matrix can be drawn up. Matrix decomposition techniques like principal component analysis (PCA) or singular value decomposition (SVD) can be applied on the sensitivity matrix to determine the most significant contributor. This sensitivity matrix can be combined with an iterative optimization routine to determine the necessary quadrature nulling voltages that will allow mode-matching during subsequent V_P ramp-up.

8.2.2 Closed-loop operation using force-feedback

Currently, the bandwidth of the microgyroscope is set by programming the soft-ware control externally. Operating the sensor open-loop provides the highest-possible gain, and lowest noise floor. However, the dynamic range can be limited to $\pm 50^\circ/s$, which is unsuitable for automotive and consumer applications. To address the dynamic range limitation, the sensor must be operated closed-loop for rotation sensing. The closed-loop operation of a Nickel ring gyroscope implemented using analog techniques has been described [16]. Recently, the closed-loop $\Sigma\Delta$ operation of inertial sensors has been reported, both for accelerometers [71] and for gyroscopes [29].

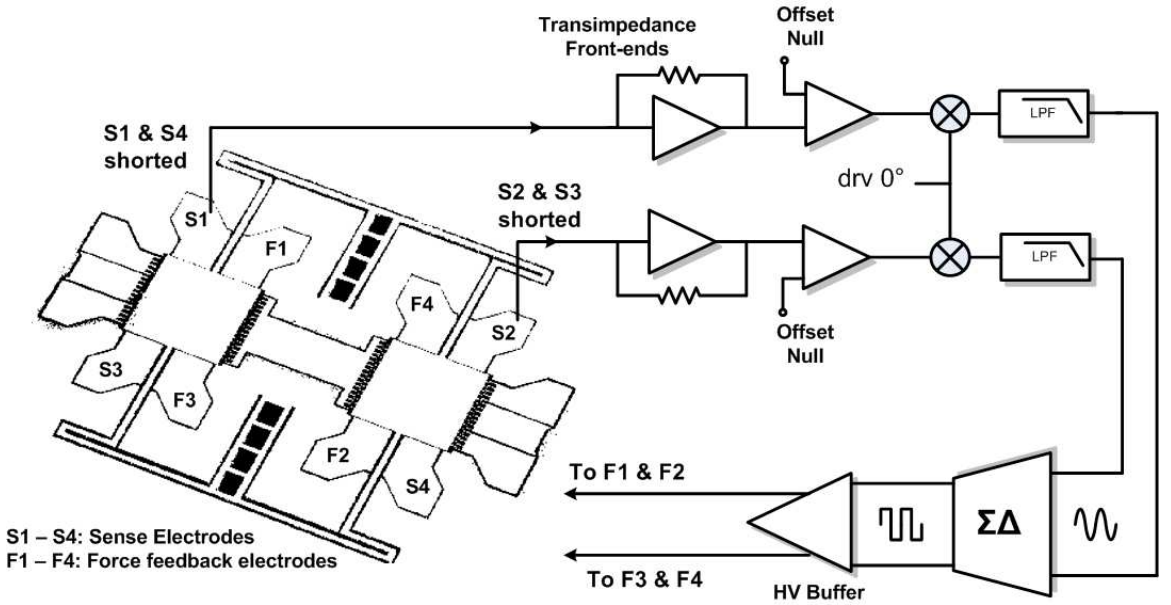


Figure 8.1: Block-diagram of closed-loop operation of the $M^2 - TFG$.

Fig 8.1 shows the block-diagram for closed-loop operation of the $M^2 - TFG$. The closed-loop operation of the gyroscope involves force-balancing the proof-masses along the sense (y)-axis. This is accomplished by placing the proof-mass in a negative feedback loop [27]. The feedback loop first measures deviations of the proof-mass along the sense axis due to rotation-induced Coriolis acceleration, using the analog sense-channel described in Chapter 4. A PID controller then applies the necessary

force in the opposite direction to keep the proof masses vibrating only along the x -axis. This force is applied by means of a pulse-width modulated bit-stream. A $\Sigma\Delta$ modulator converts the analog rate output into a pulse-width modulated bit-stream. The bit-stream is then applied to the 4 inner parallel-plate electrodes, to generate a force that is 180° out of phase with the Coriolis force. This force must be applied at the sensor resonant frequency and the duty-cycle of each of the pulses contains the modulated rotation information, i.e., the force required to null the y -axis proof-mass displacements is generated using a pulse-width modulated bit-stream. Output from the gyroscope is now taken as the force needed to null, or zero, the motion along the y -axis.

By preventing proof-mass deflections along the y -axis, nonlinearities from the capacitive pick-off and mechanical springs are minimized. Keeping the proof-mass stationary translates to a larger dynamic range, since the possibility of electromechanical pull-in is mitigated. An advantage with the proposed closed-loop scheme is that no dedicated feedback phase is necessary for applying the closed-loop scheme.

A single-ended 2^{nd} order $\Sigma\Delta$ modulator has been implemented to perform the A/D conversion of the rotation signal, as shown in Fig 8.2. This is based on the architecture presented in [72].

A 2^{nd} order $\Sigma\Delta$ modulator offers better noise shaping and hence was chosen over the simple 1^{st} order modulator used in the mode-matching system. As can be seen from the SPECTRE simulation results in Fig 8.3, the noise shaping advantage of the 2^{nd} order modulator over that of the 1^{st} order is clearly evident. Both simulations used the same signal and clock frequency.

The core OTA used to implement the 2^{nd} order $\Sigma\Delta$ modulator was the low-noise two-stage Miller-compensated OTA, used for the T-network TIA described in Chapter 3. Fig 8.4 shows the measured time domain and frequency domain measurements of

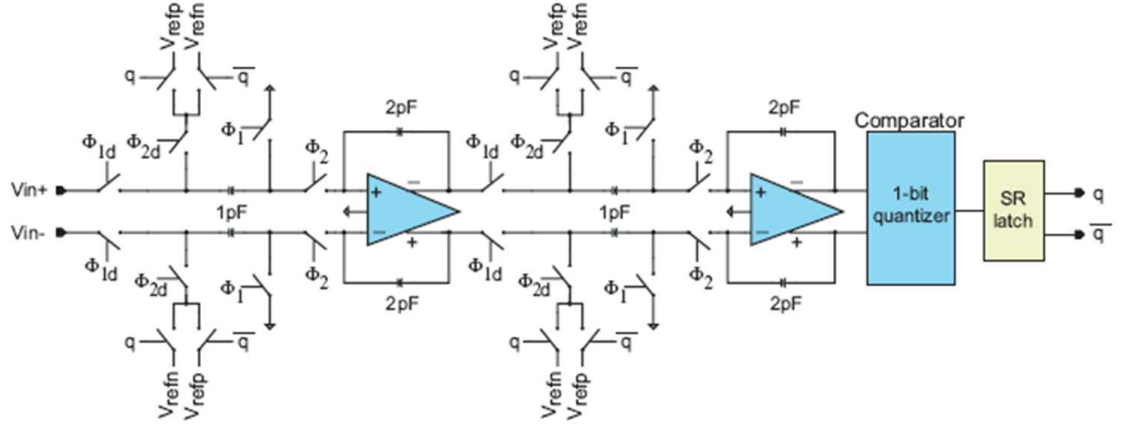


Figure 8.2: Schematic of the 2^{nd} order $\Sigma\Delta$ modulator.

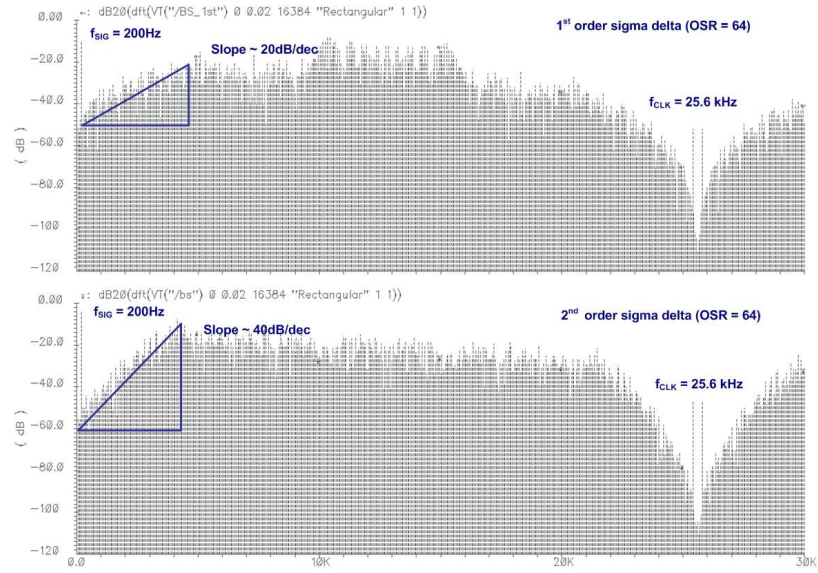


Figure 8.3: Noise shaping advantage of the 2^{nd} order $\Sigma\Delta$ modulator.

the implemented modulator.

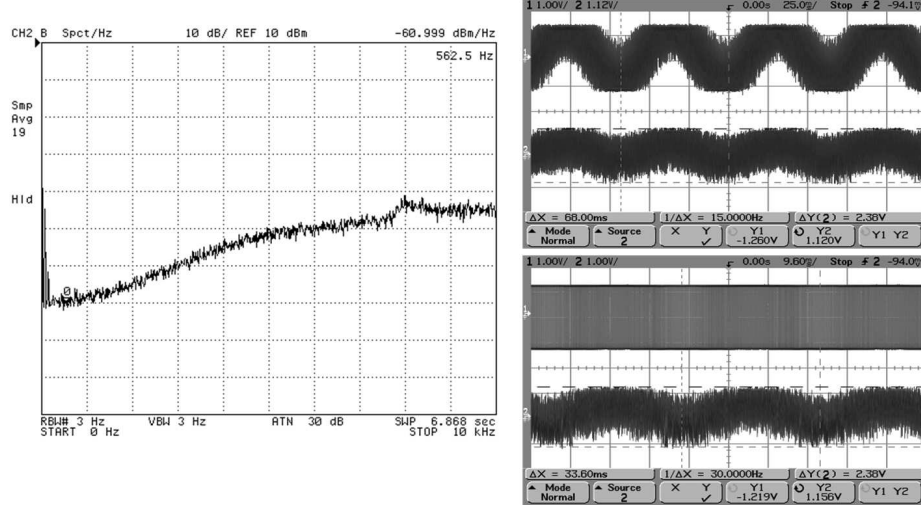


Figure 8.4: Measured waveforms and frequency spectrum of the 2nd order $\Sigma\Delta$ modulator.

There are two main challenges in implementing the closed-loop system for the $M^2 - TFG$. First, the linearity of the feedback forces must be carefully analyzed, since the voltage-to-force transducer is a parallel-plate capacitor. Second, the impact of the force-feedback pulses on sensor quality factor has not been analyzed. Thus far, the only closed-loop rate sensor systems have involved low-Q sensors. Further studies must therefore be undertaken to study the impact of force-feedback on high-Q structures.

8.2.3 Flash ADC for Coarse tuning

A 4-bit flash ADC has been implemented which can be used to measure the ZRO, and switch the V_P in a coarse fashion. This can be used in cases where the ASIC is not pin limited, and where direct digital information is necessary; i.e., decimation cannot be implemented.

Fig 8.5 shows the circuit schematic and the die micrograph of the 4-bit Flash ADC implemented in the $0.5\mu m$ CMOS process.

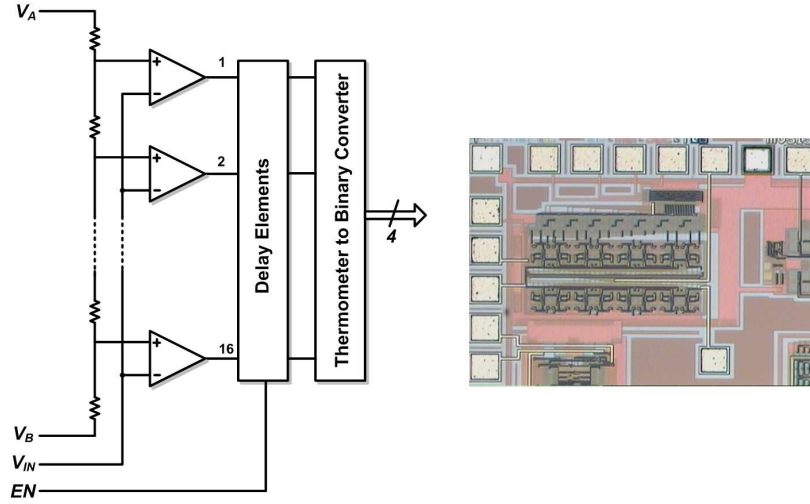


Figure 8.5: Schematic and die micro-graph of the 4-bit flash ADC.

Fig 8.6 shows the measured output of the flash ADC, to a ramp signal as well as a sinusoidal input. From the graphs, it is seen that the flash ADC is monotonic, does not have any missing codes, and exhibits a measured INL of $\pm 0.5LSB$.

8.2.4 Bandwidth increase by Q-loading

The bandwidth of the gyroscope is a function of the mode separation as well as the inherent quality factor of the resonant modes. Controlled mode-splitting has been demonstrated to effectively increase the bandwidth of the sensor. However, there exists an alternate means to increase open-loop bandwidth. This involves electronically loading the quality factor of the gyroscope in mode-matched condition as shown schematically in Fig 8.7. Q-loading decreases the Q_{EFF} while maintained the gyroscope in mode-matched condition. Q_{EFF} is lowered with no change in frequency, and therefore the bandwidth is increased.

Electronic Q-loading can be achieved by varying the input impedance that the micromechanical devices sees, looking into the transimpedance front-end. By providing an alternate feedback path, the normally low input impedance provided by the shunt-shunt feedback can be increased, thereby loading the quality factor, as

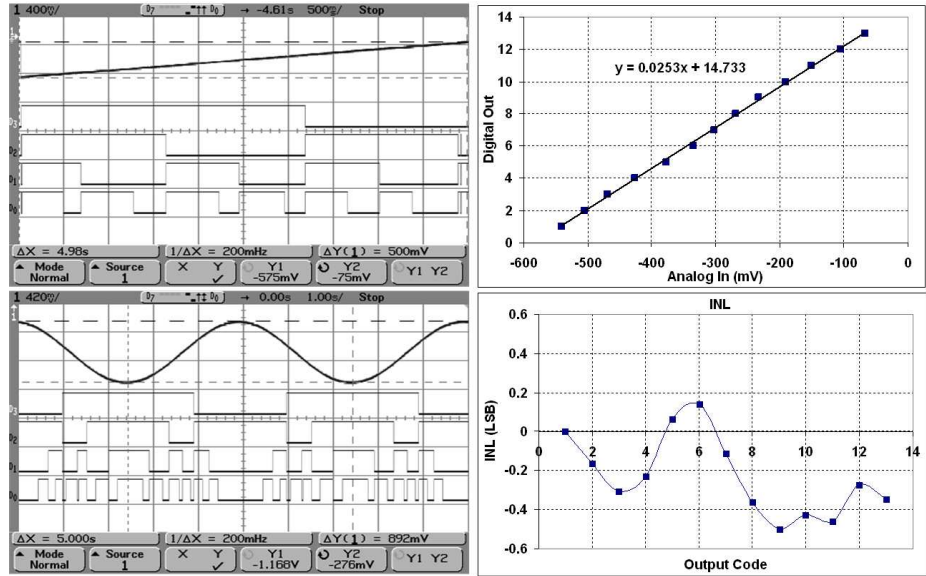


Figure 8.6: Measured waveforms of input and output of 4-bit flash ADC. Measured Input-output characteristics and INL

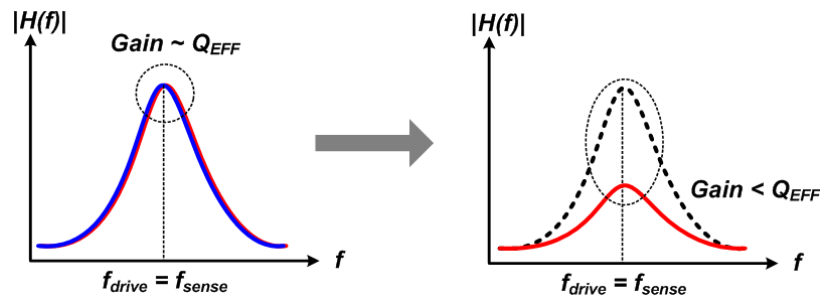


Figure 8.7: Conceptual representation of Q-loading to increase open-loop bandwidth.

given by Eq.(3.4).

The main limitation that must be overcome is that the Q is already significantly loaded when the device is packaged. Most packaging schemes offer no better than 10 - 100mTorr of vacuum. Therefore, a detailed characterization of the Q, and factors that impact it must be undertaken before electronic Q-loading becomes viable.

8.2.5 A 1.8V 0.01°/hr silicon vibratory microgyro

Finally, it is envisioned that microgyroscopes will attain the 0.01°/hr bias drift mark. Achieving such a low bias drift will involve a combination of advances in silicon micromachining, ultra-low noise and low-power CMOS circuit design, and smart interfaces that integrate significant amount of software control and calibration.

High-aspect ratio ($\geq 50:1$) will allow for reduced operating voltages that can be generated on-chip. A charge-pump designed in a 1.8V 0.35 μm standard CMOS process can typically generate DC voltages in the order of 10 - 15V, which will be sufficient for the high-aspect ratio structures. Lateral BJT transistors that are available at no extra cost are being used frequently in numerous designs. A number of commercial foundries provide models and p-cells for lateral BJT's in their conventional CMOS processes. The use of BJT inputs and output stages significantly mitigates the flicker noise problem, and can therefore enable further bias drift reduction.

Currently, the largest impediment to widespread commercialization of MEMS gyroscopes is the requirement for a robust wafer-level vacuum-packaging scheme. Once such a scheme is in place, it will allow the batch fabrication of sub-degree per hour microgyros along with μ -g accelerometers, and provide an integrated, battery-powered 6-DOF motion sensing platform for chip-scale navigation.

APPENDIX A

BIAS DRIFT MEASUREMENT

Below is the code used for Allan Variance computation

```
%Comparison of Allan Variance data for u-Gyros
% modification log:
% created: 9/10/05 - Ajit Sharma
% modified: Sept 07 - M. Zucher - changed binning
% modified: Sept 07 - M. F. Zaman - removed residual zeroes in matrix.

clear all;
close all;
format long e;
sig2 = [];
tau = [];
D = [];
vavg = [];
vavg_mean = [];
zro = [];
bin_size = 0;
% LOAD APPROPRIATE DATA AND SENSITIVITY VALUES
%set 3 - 25 deg data
vavg_all = load('./data/vpp_vec.dat');
vavg_raw = vavg_all(1:100000);
% FILTER THE DATA
% generate filter - i.e. find the filter coefficients
Wn = [0.15];
[B,A] = butter(24,Wn,'high','s');
% now actually filter the data and generate filtered output on which we run the AVAR
vavg_filt = filter(B,A,vavg_raw);
% normalize the data
vavg_mean = vavg_filt(10:end) - mean(vavg_filt(10:end));
sens = 6.67e-6;      % V/deg/hr
zro = vavg_mean./sens;
n = length(zro);      % total number of data points in subset
tau0 = 0.43;
total_time = n * tau0; % this is the total time we have collected data for in subset of data
% we are calculating AVAR for
```



```

ctr = 1; % how many points to take in each bin.
scale = 1;
bin_size = 1;
while bin_size < floor((n/20)*tau0); % divide the data into bins (minimum 8)
    fprintf(' ');
    m = 10*scale; % set minimum bin size = 10
    bin_size = m * tau0; % number of seconds in bin each bin
    tau(ctr) = bin_size;
    for i=0:floor(n/m)-1 % find the average of each bin
        bin_ave(ctr,i+1)= mean(zro((1+m*i):(i+1)*m));
    end;
    ctr = ctr + 1; % counter tells you how many points you are taking for
    % each bin
    scale = scale + 1;
end;
% bin_ave: # of rows on bin_ave is number of different tau's used to sample.
% # in each row of bin_ave, the number of non-zero entries tells you how
% many bins were formed from the entire data set using that particular tau
n_tau = length(tau); % total number of sampling times
for i = 1:n_tau;
    x = bin_ave(i,:);
    %diff_bin = bin_ave(i,:);
    %diff_bin = bin_ave(i,1:(length(x)-sum(x(:)==0))); % courtesy Chaitanya
    diff_bin = bin_ave(i,1:(length(find(x))));
    % find the diff between successive bins and square the values
    diff_bin_sqr = (diff(diff_bin)).^2;
    % now scale the differences after finding the average
    diff_bin_ms = (0.5)*mean(diff_bin_sqr);
    sig2(i) = sqrt(diff_bin_ms);
end;
save new_avar.dat tau sig2 -ascii -double;
%%%%%%%%%%%%%%%%%%%%%%%%%%%%%%%%%%%%%%%%%%%%%%%%%%%%%%%%%%%%%%%%%%%%%%%%
% Create plots
%%%%%%%%%%%%%%%%%%%%%%%%%%%%%%%%%%%%%%%%%%%%%%%%%%%%%%%%%%%%%%%%%%%%%%%%
t_seconds = tau0*(1:n); % total number of samples * sampling period of points in AVAR
figure(1);
subplot(2,1,1);plot(vavg_mean,'b*-');
hold on;
grid on;
xlabel('time points');
ylabel('raw voltage (V)');

```

```

subplot(2,1,2);plot(t_seconds,zro,'k+-');
hold on;
grid on;
xlabel('seconds');
ylabel('rate (deg/hr)');
figure(2);
semilogx(tau,sig2,'r*-','LineWidth',2);
hold on;
grid on;
xlabel('\tau (s)');
ylabel('deg/hr');
semilogx(tau,sig2,'r*-','LineWidth',2);
title('Allan variance of M2-TFG');
bias_drift = min(sig2)

```

Once the Allan Variance analysis has been completed the following curve-fitting routines are run.

```

% ajit sharma
% to curve_fit the data we get from the allan variance plot.
clear all;
close all;
format long e;
set(0,'DefaultLineLineWidth',2)
set(0,'DefaultAxesFontWeight','bold')
set(0,'DefaultAxesFontSize',14)
% load the drift data 25 deg C
%data_25 = load('../new_avar_no_filt.dat ');
data_25 = load('../azdt_avar.dat ');
tau_25 = data_25(1,1:end);
sig2_25 = data_25(2,1:end);
% taking the case of interest
tau = tau_25(1:9);
sig2 = sig2_25(1:9);
n = length(tau);
% initial values if we have ALL
N_o = 0;
B_o = 0;
K_o = 0;
Q_o = 0;
% to curve fit sections
X0 = [N_o B_o K_o Q_o]; % initial values

```

```

N_n = N_o;
B_n = B_o;
K_n = K_o;
Q_n = Q_o;
%%defining global variables.
global B_n N_n K_n Q_n tau0 n tau sig2;
option_file;    %file that sets the options parameters.
blank = [];
lam = lsqcurvefit('my_func',X0,tau,sig2,blank,blank,options);
N_n = lam(1)
B_n = lam(2)
K_n = lam(3)
Q_n = lam(4)
y = Q_n*(tau.^(-1)) + N_n*(tau.^(-0.5)) + B_n + K_n*(tau.^(0.5));
figure(1);
semilogx(tau,y,'r-','LineWidth',3.5);
hold on;
grid on;
semilogx(tau,sig2,'bo','LineWidth',2.5);
xlabel('Sampling Time \tau (s)');
ylabel('deg/hr');
%title('Root Allan Variance of Matched-mode TFG');
legend('fit','measured');
ARW = N_n/60
Bias_Drift = min(sig2_25)

```

The above curve fitting routine calls a separate function *my_func.m*, which is provided below:

```

%ajit sharma
%created:2/11/2003
%modified: 4/21/2003
%function called by optimization routine.
%the files r_epic.dat and z_epic.dat are overwritten every time the
%function enters a new optimization loop. this prevents unnecessary
%accumulation of data
%WHEN USING LSQCURVEFIT
function y1 = my_func(lam,x,sig2);
%%defining global variables.
global B_n;
global N_n;
global K_n;

```

```

global Q_n;
global tau;
global tau0;
global n;
global sig2;
N_n = lam(1);
B_n = lam(2);
K_n = lam(3);
Q_n = lam(4);
y1 = Q_n*(tau.^(-1)) + N_n*(tau.^(-0.5)) + B_n + K_n*(tau.^(0.5));

```

The following file is the file *option_file.m* that contains the optimization parameters:

```

%ajit sharma.
%created: 2/11/2003
%file that sets options for the optimization
%routine.
options = optimset;
options1 = optimset('Display','iter','MaxFunEvals',100,'MaxIter',200);
options2 = optimset(options1,'DiffMinChange',1e-9,'LargeScale','off');
options3 = optimset(options2,'LevenbergMarquardt','on','TolFun',1e-12);
options = optimset(options3,'TolX',1e-12);

```

APPENDIX B

ELECTROMECHANICAL MICROSYSTEM MODELING AND SIMULATION

System level time and frequency domain simulations have been carried out in MATLAB. A SIMULINK model for the gyroscope provides a qualitative understanding of the sensor. The 2nd order ODE's that describe the drive and sense resonant modes (Chapter 2) are expressed in the s-domain, and incorporated into SIMULINK. Fig B.1 shows the implemented SIMULINK model. The model has two inputs: the input drive voltage at the drive resonant frequency, and the input rotation to be sensed. Gyro behaviour in both the time and frequency domains was compared with measured responses, to verify that the model captured the essential system characteristics.

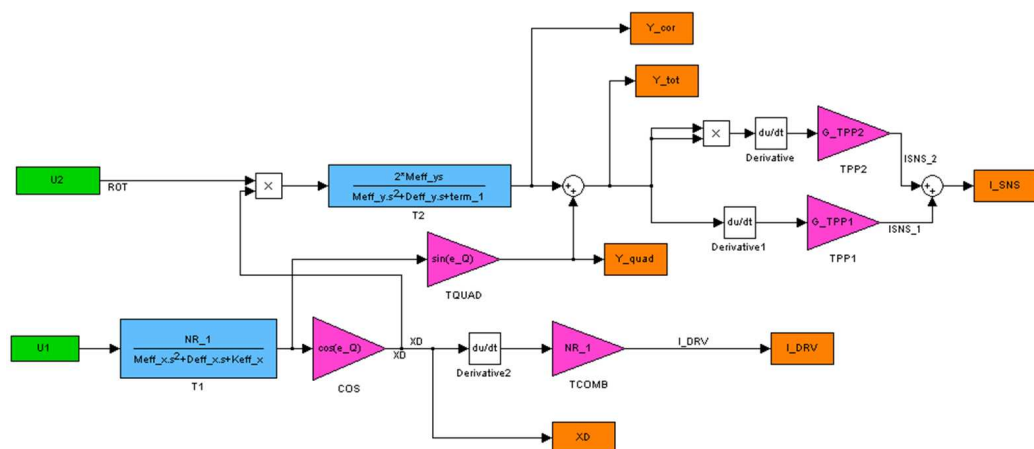


Figure B.1: SIMULINK model of the gyroscope.

The quadrature error in the system has been modeled empirically as an angle e_Q that the drive mode makes with the ideal drive axis [21]. Fig B.2 shows the drive- and sense-transfer function plotted as a function of frequency. The variation of the sense

resonant frequency with V_P has been modeled. As V_P is increased, the sense resonant mode frequency decreases and can be made equal to the drive mode frequency. The drive mode frequency stays relatively constant to first order.

It must be noted that in these simulations the emphasis was on obtaining a qualitative behaviour so as to understand the sensor behaviour. The modeling does not aim to capture exact quantitative behaviours due to the variations inherent to the fabrication process.

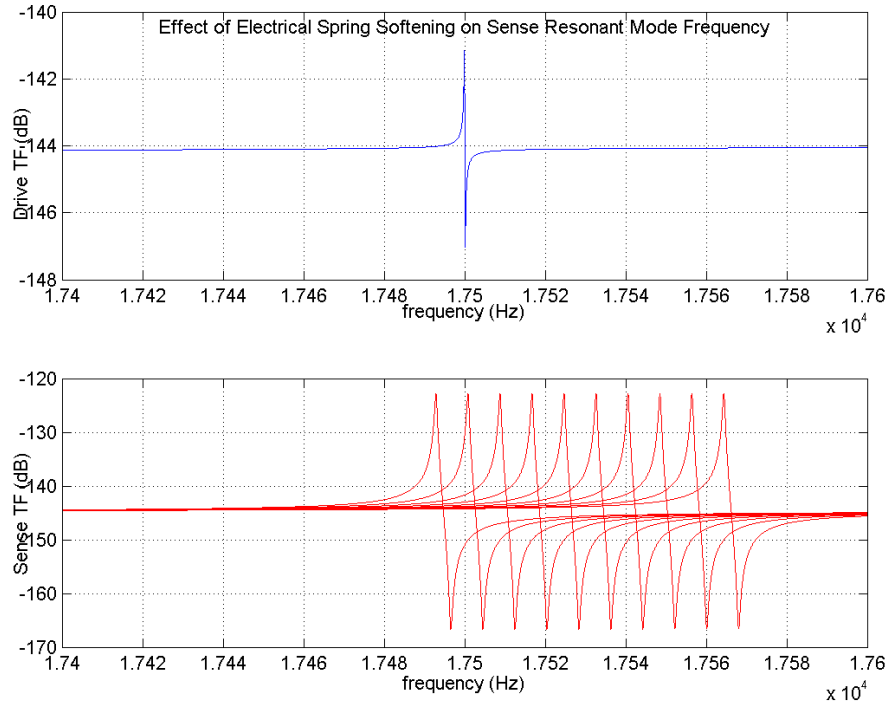


Figure B.2: Frequency domain behaviour showing ω_{SNS} decreasing with increasing V_P , while ω_{DRV} stays relatively constant.

Fig B.3 shows the waveforms seen at one of the sense electrodes of the sensor at mode-matched condition when an input rotation is applied. The 90° phase difference that exists between the quadrature signal and the component of the sensor output containing AM rotation information is clearly visible. The total output signal is also plotted. This signal appears to be in phase with the quadrature error, since the level

of the quadrature signal is typically at least an order of magnitude larger than the Coriolis rotation. This phase difference explains why phase sensitive synchronous demodulation can be used to extract the rotation signal that is buried in the noise.

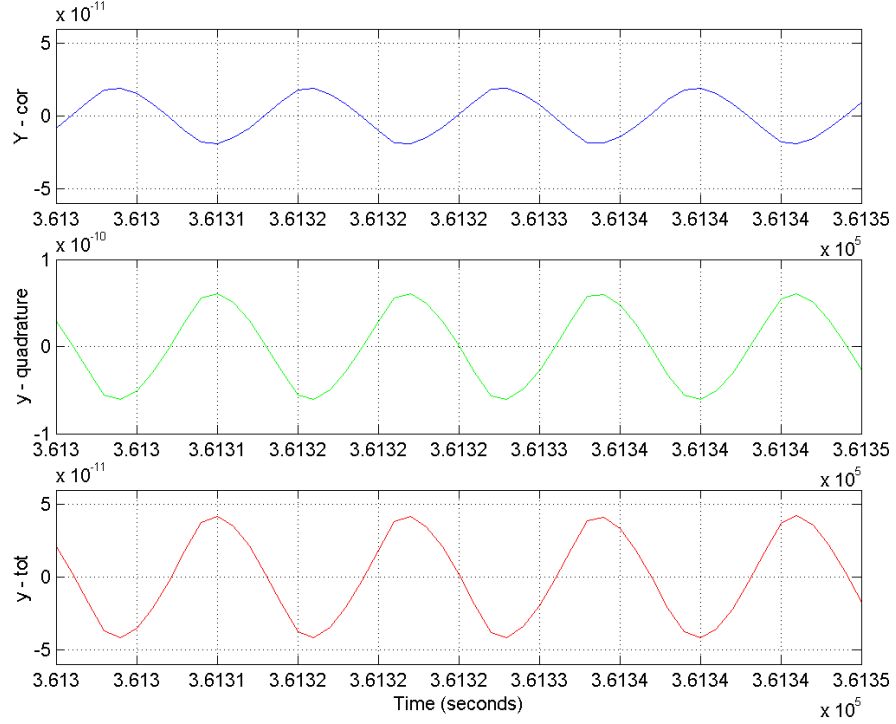


Figure B.3: Time domain behaviour showing phase relationships between signals at mode-matched condition.

One of the key aspects of the SIMULINK model is that it captures the behaviour of the sensor for mode-matching purposes. Capturing the time-domain behaviour of the sensor is essential, since the proposed mode-matching scheme is time-domain based, as explained extensively in Chapters 5 and 6. Fig B.4 shows the time-domain ZRO as a function of the polarization voltage (V_P). The amplitude of the ZRO increases as the value of V_P approaches the value required for mode-matching (here taken to be 12.14V). Closer inspection of the ZRO plots for different V_P 's shows that the model also captures the 90° phase shift in ZRO that characterizes mode-matched operation (i.e., ZRO at mode-matched condition is 90° phase shifted as compared to

the unmatched condition).

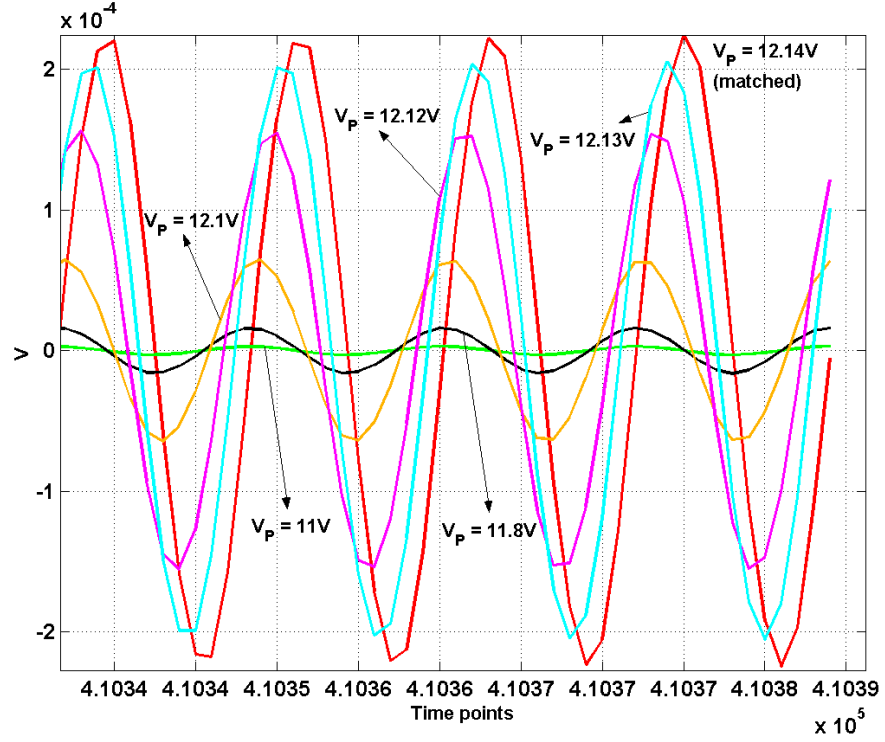


Figure B.4: Time domain behaviour showing ZRO amplitude increasing as V_P nears the value required for mode-matching. The mode also captures the 90° phase shift that occurs at mode-matched condition.

Fig B.5 shows the sensitivity of the sensor as a function of V_P . As expected, at mode-matched condition, the sensitivity of the sensor to both Coriolis as well as residual quadrature is maximized.

The mode-matching algorithm has been tested with the SIMULINK model, and Fig B.6 shows the results. As the V_P is incremented, there is an increase in the ZRO level. Once a maximum in the ZRO level has been detected, the algorithm stops and the V_P value is held constant.

Equivalent RLC circuit representations of the sensor were used for system simulations in a circuit environment (e.g. SPICE or Spectre). However, as mentioned in Chapter 2, the variation of the signal level with increase in V_P is better modeled

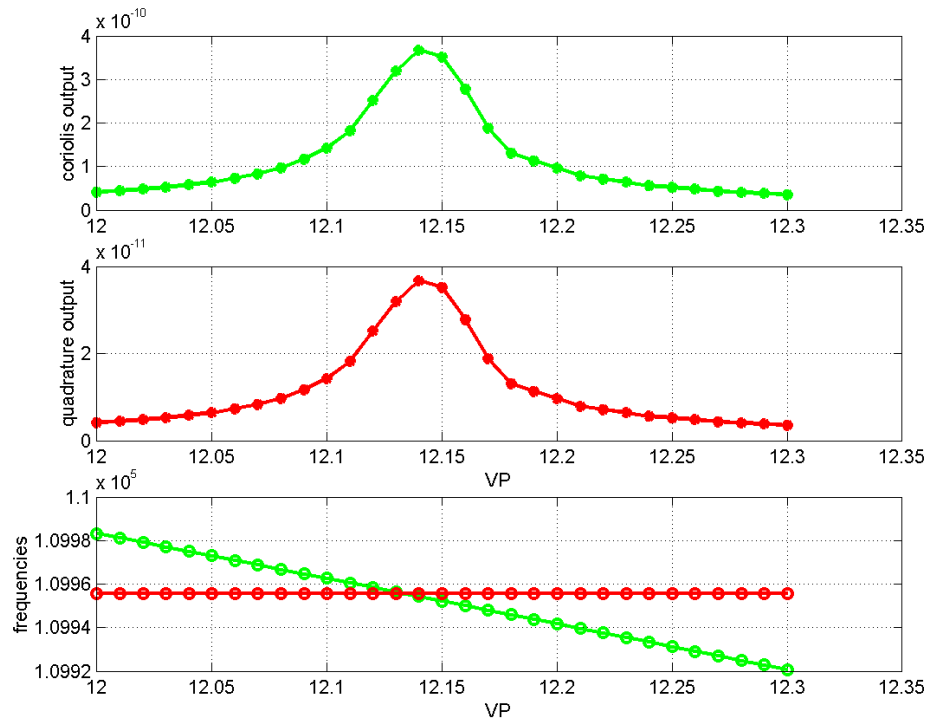


Figure B.5: Frequency domain behaviour showing that sensor sensitivity is maximum when the frequency of sense mode is equal to that of drive mode.

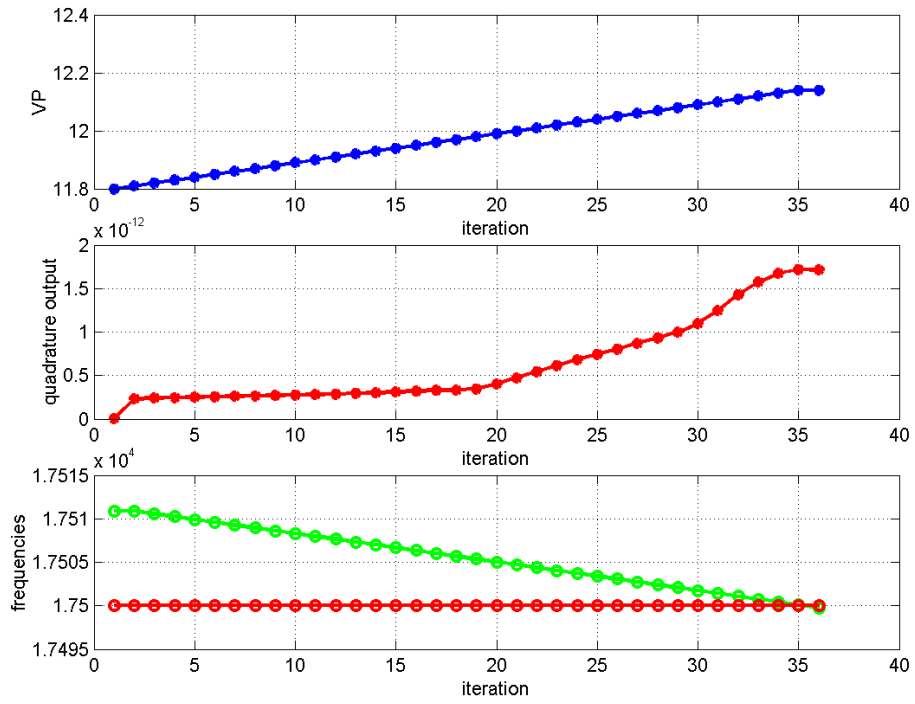


Figure B.6: Modeling of the automatic mode-matching scheme showing how ZRO level increases as the frequency separation between drive and sense modes are decreased. Note that the VP does not increment once the maximum in ZRO level has been reached.

using an HDL for co-simulation with a SPICE-like circuit simulator. The variation of sense signal with V_P was modelled behaviourally using Verilog-A and Spectre was used as a simulator.

The Verilog-A code is provided below:

```
// VerilogA for hdl_lib, vp_gain, veriloga
`include "constants.h"
`include "discipline.h"
module vp_gain_set (vpin, vpout);
input vpin;
output vpout;
voltage vpin, vpout;
parameter real vpm = 78.15 from [0:inf);
parameter real vps = 0.03 from [0:inf);
parameter real vpo = 10 from [0:inf);
analog begin
V(vpout) <+ vpo*exp(-1*(((V(vpin) - vpm)*(V(vpin) - vpm))/(2*vps*vps)));
end
endmodule
```

Fig B.7 shows the variation of the ZRO signal as a function of the V_P -stepper output. Once the V_P -stepper crosses the value required for mode-matching, the level of ZRO falls.

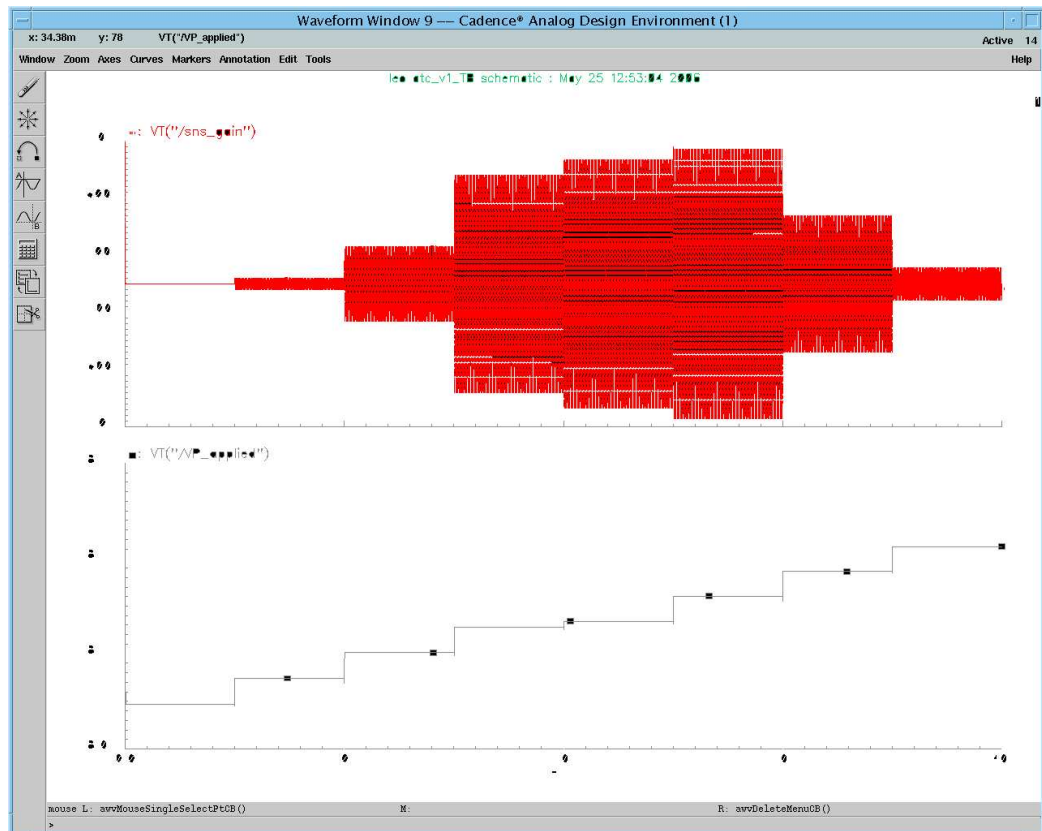


Figure B.7: Simulation waveforms from Cadence showing the increase and then decrease in ZRO amplitude as the DAC is stepped past the optimum value required for mode-matched operation.

APPENDIX C

DISCRETE ELECTRONICS FOR LOW-FREQUENCY GYROSCOPES

This appendix summarizes the schematic block diagrams for the discrete gyroscope control electronics. Fig C.1 shows the drive and sense electronics.

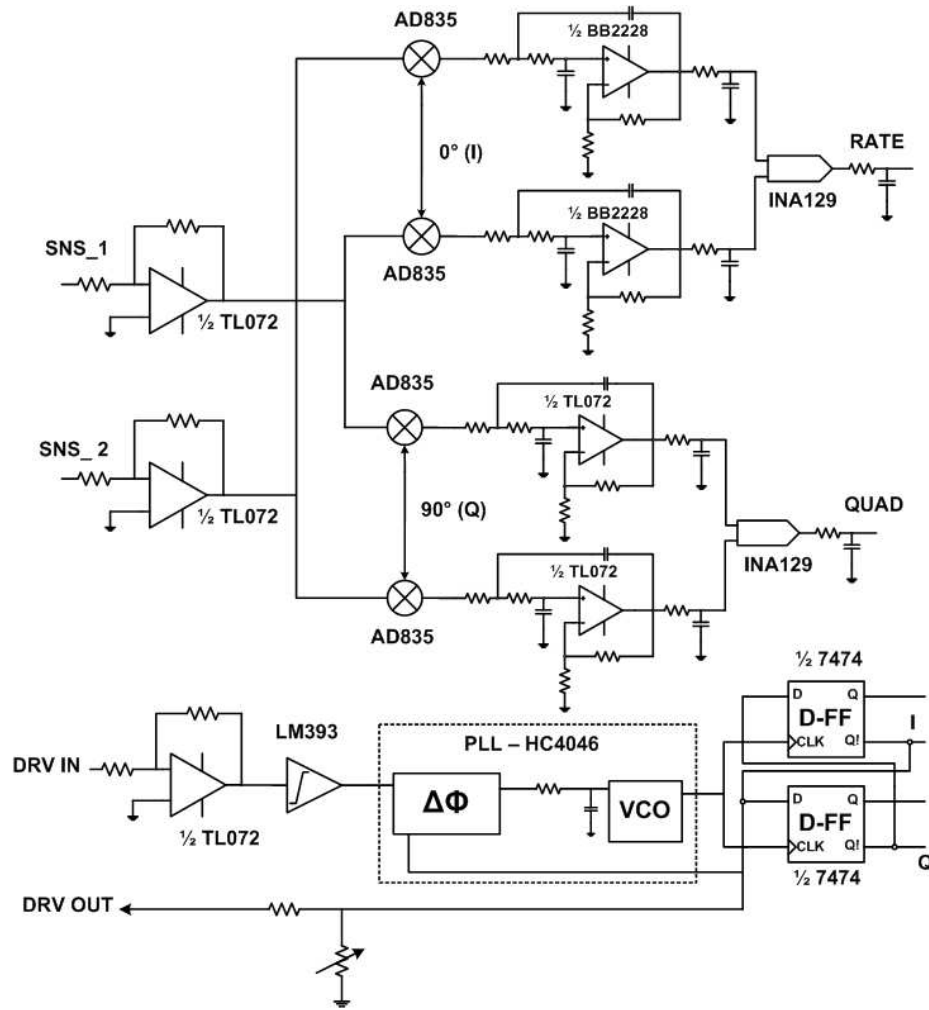


Figure C.1: Schematic of the discrete implementation of the gyro control electronics.

The drive loop is implemented using the PLL-based drive oscillator described in

Chapter 4. Fig C.2 shows the schematic of the PLL circuit that uses a discrete HC4046 digital PLL. The phase detector used is the simple XOR phase detector. A pull-up resistance at the output is necessary for the LM339 comparator, as the collector is open.

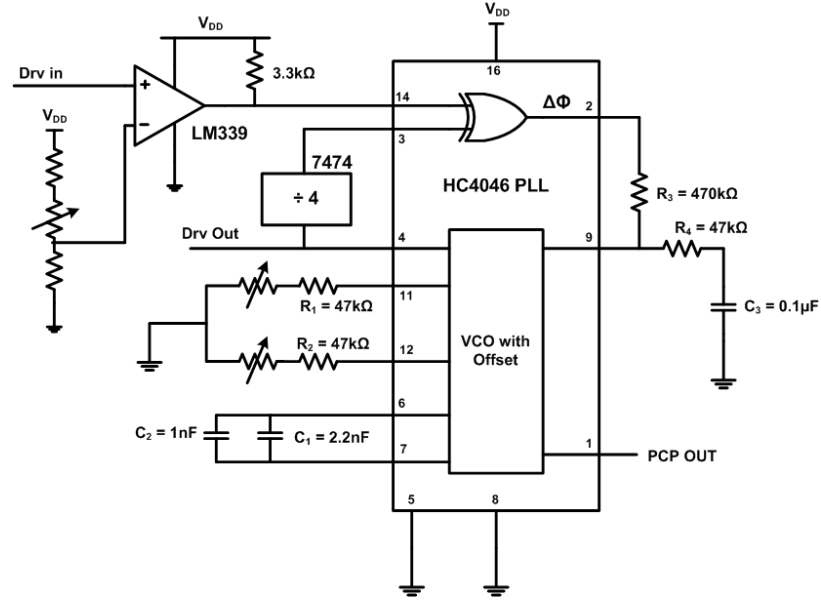


Figure C.2: Schematic diagram of the discrete PLL drive loop electronics.

Synchronous demodulators for obtaining the rate and quadrature signals are implemented using multipliers and low-pass filters. The multiplier used here is the AD835 from Analog Devices, configured as shown in Fig C.3.

The low-pass filter is a Sallen-Key implemented using either a TL072 or BB2228 dual op-amp and the schematic is shown in Fig C.4.

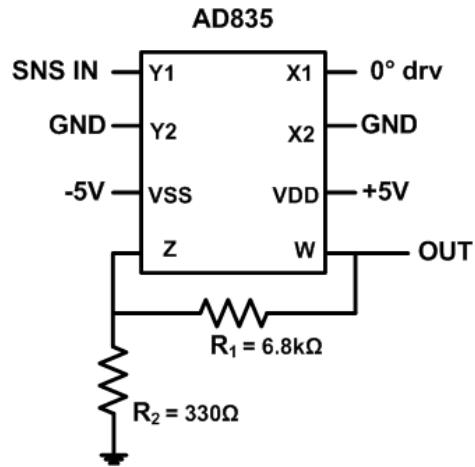


Figure C.3: Schematic diagram of the discrete multiplier (AD835).

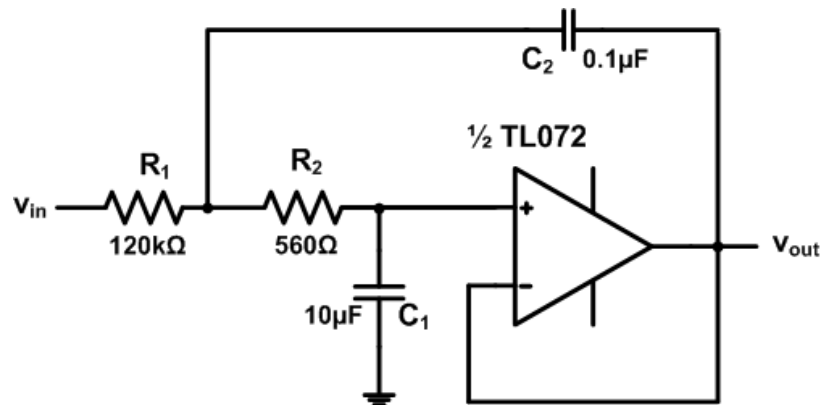


Figure C.4: Schematic of the discrete implementation of the 2nd order Sallen-Key filter.

APPENDIX D

FILTERING BIAS DRIFT DATA AND EFFECTS ON GYRO DRIFT PERFORMANCE

Bias Drift is a measure of the random variation in the gyro output. The model for a gyroscope with analog output is given by [60]:

$$S_0 V_0 = [\Omega_Z + D](1 + 10^{-6} \epsilon_K)^{-1}$$

where, S_0 is the nominal scale factor ($V/^\circ/s$), V_0 is the analog output voltage (V), Ω_Z is the input rotation rate ($^\circ/hr$), D is the sensor drift ($^\circ/hr$), and ϵ_K is the scale factor variation (ppm).

The sensor drift, D , can be expressed as:

$$D = D_F + D_R + E$$

where D_F is the sensor bias, D_R is the random drift which is composed of angle random walk, flicker bias instability, rate random walk and quantization effects, and E is the environmental drift.

Clearly the Allan Variance technique measures and characterizes the random component of gyro bias, and all other factors must be eliminated. Other sensitivities that affect the gyro bias include, but are not limited to, effects due to input power variations including frequency, voltage, ripple, starting and operating current [8].

Effects of external factors

To give an example of external factors that affect long-term stability, two sets of separately run characterization data, one for 42 hours and other other for 75 hours respectively, are shown in Fig D.1. The upper trace (in blue) is the measured V_P from

the power supply and the lower trace (in red) is the measured analog rate output from the gyro, which is at rest. The direct correlation between the V_P variation and the output analog rate is clearly evident from the graph. The variation due to power supply variation is a systematic offset and can be compensated by using stable PVT compensated supplies or a high performance voltage regulator.

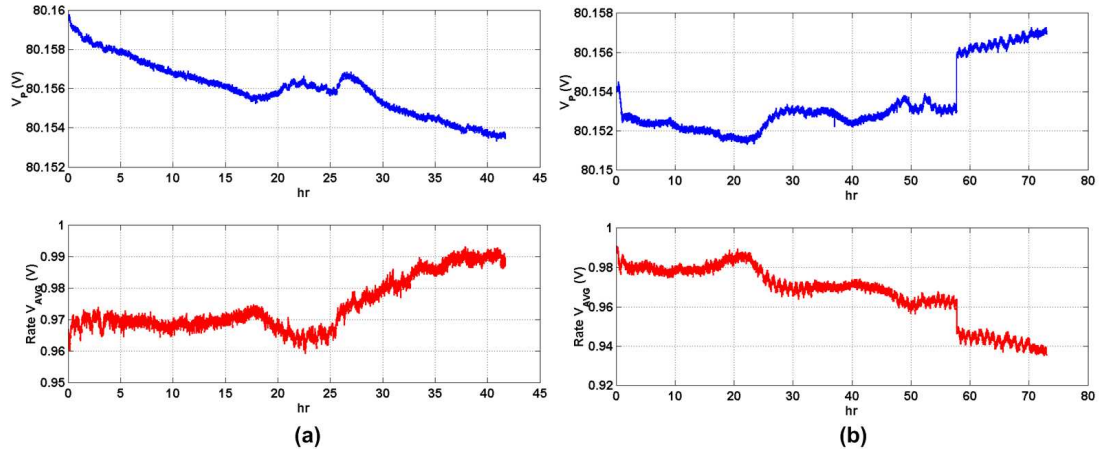


Figure D.1: Effects of V_P variation on long-term stability.

Filtering the data - System's applications.

Computing the Allan variance involves referring the measured output to its mean value. This implicitly eliminates the DC component of the bias. Instead of subtracting the mean value from the time series before obtaining the output, most angular rate measurement systems, use a high pass filter to filter out the DC component of the bias, as shown in Fig D.2, which is taken from [98].

Patent 6486661 from Delphi Corporation [99], utilizes a digital scheme to compensate the bias drift. The method used to estimate the drift consists of *differentiating the output signal by computing a difference in the output signal over a period of time*. Just as a low-pass filter provides integration, so also, a high-pass filter does an inherent differentiation operation.

How to choose the cut-off frequency?

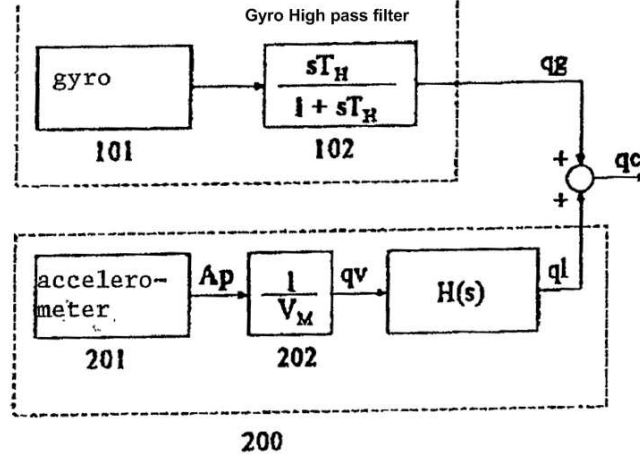


Figure D.2: System incorporating a gyro and accelerometer, where gyro output is high-pass filtered.

Without filtering, the settling time as obtained from the root Allan Variance plot is in the order of 30s, as seen in Fig D.2 below. The filtering must not affect the settling time of the sensor.

The filter cut-off frequency was chosen to be less than half the frequency corresponding to the settling time. This gives:

$$f_{-3dB} = 1/60s \sim 0.0166Hz$$

What is the filter we are using?

The filter used to post-process the gyro analog output in our case, is a 10th order Butterworth filter with a -3dB cut-off frequency at 0.015Hz. The high order of the filter ensures that the -1dB and -3dB cut-off frequencies are close to each other, due to the high roll-off. Fig D.4 plots the filter transfer function in dB.

Bias Drift after filtering

The bias drift plots after applying the filtering are shown in Fig D.5 below. As seen, the settling time remains unchanged - which implies that the filtering has not changed the dynamic characteristics of the sensor - it has only removed the DC

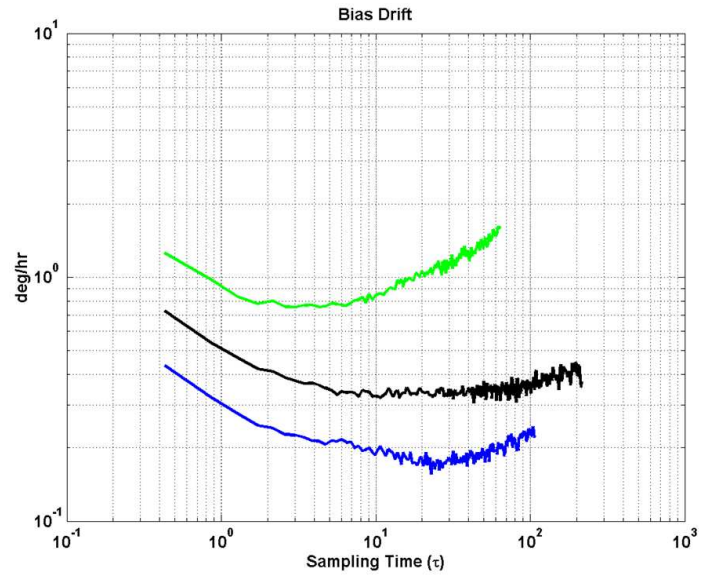


Figure D.3: Root Allan Variance without applying any filtering.

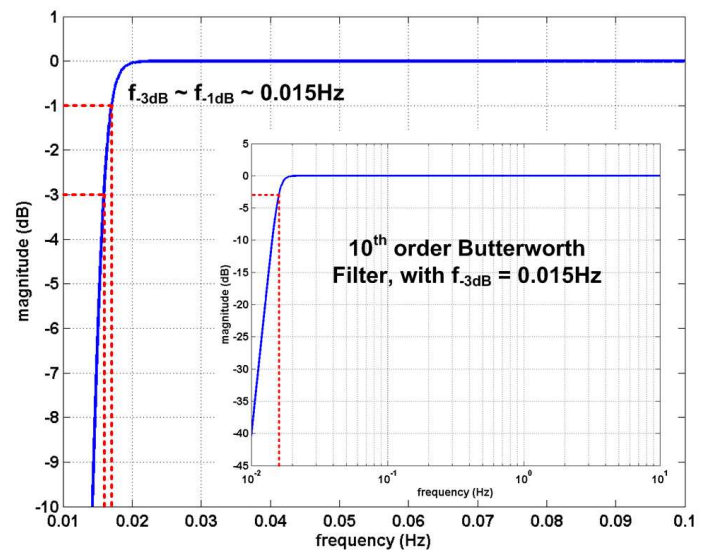


Figure D.4: Filter characteristics of the high-pass filter used for bias drift estimation.

component of the sensor.

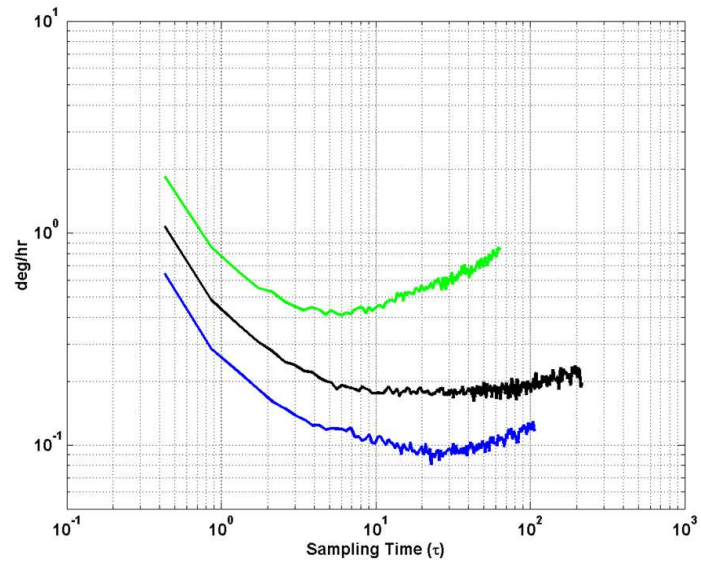


Figure D.5: Root Allan Variance after filtering with the HPF.

REFERENCES

- [1] N. Yazdi, F. Ayazi, and K. Najafi, “Micromachined inertial sensors,” *Proceedings of the IEEE*, vol. 86, no. 8, pp. 1640–1659, Aug. 1998.
- [2] (2007). [Online]. Available: www.chooseesc.eu
- [3] A. Lawrence, *Modern Inertial Technology*. New York, NY: Springer-Verlag, 1993.
- [4] H. Lefevre, *The fiber-optic gyroscope*. Artech House, 1993.
- [5] F. Aronowitz, *The laser gyro*, 1st ed. Monte Ross, 1971.
- [6] R. R. Ragan and D. D. Lynch, “Inertial technology for the future, part x: Hemispherical resonator gyro,” *IEEE Transactions on Aerospace Electronic Systems*, vol. AES-20, p. 432, July 1984.
- [7] “IEEE standard for inertial sensor terminology,” IEEE, Aug. 2001.
- [8] “IEEE standard specification format guide and test procedure for coriolis vibratory gyros,” IEEE, Jan. 2004.
- [9] J. Bernstein, S. Cho, A. T. King, A. Kourepenis, P. Maciel, and M. Weinberg, “A micromachined comb-drive tuning fork rate gyroscope,” in *Proc. of IEEE International Conference on Micro Electro Mechanical Systems, (MEMS’93)*, Fort Lauderdale, FL, USA, Feb. 7–10, 1993, pp. 143–148.
- [10] M. Zaman, A. Sharma, B. V. Amini, and F. Ayazi, “The resonating star gyroscope,” in *Proc. of IEEE International Conference on Micro Electro Mechanical Systems, (MEMS’05)*., Miami, FL, USA, Jan.25–29 2005, pp. 355–358.
- [11] W. S. Watson and T. J. Henke, “Coriolis gyro configuration effects on noise and drift performance,” in *Gyro Symposium*, Stuttgart, Germany, Sept. 2002, pp. 927–935.
- [12] M. Bowser, J. Hammond, M. Perlmutter, and C. Reynolds, “Remote fiber optic gyroscopes for a broad range of applications,” in *IEEE Position Location and Navigation Symposium, (PLANS’96)*, 1996, pp. 553–558.
- [13] “QRS14 angular rate sensor,” in *Systron Donner Data Sheet*, 1998.
- [14] J. A. Geen, S. J. Sherman, J. F. Chang, and S. R. Lewis, “Single-chip surface micromachined integrated gyroscope with 50 deg/hr allan deviation,” *IEEE Journal of Solid-State Circuits*, vol. 37, no. 12, pp. 1860–1866, Dec. 2002.

- [15] “GG1178 MEMS angular rate gyroscope,” in *Honeywell Data Sheet*, 2005.
- [16] M. W. Putty, “A micromachined vibrating ring gyroscope,” Ph.D. dissertation, University of Michigan, Mar. 1995.
- [17] D. Keymeulen, W. Fink, M. I. Ferguson, C. Peay, B. Oks, R. Terrile, and K. Yee, “Tuning of MEMS devices using evolutionary computation and open-loop frequency response,” in *IEEE Aerospace Conference 2005*, Mar. 2005, pp. 1–8.
- [18] B. V. Amini and F. Ayazi, “A 2.5-v 14-bit CMOS SOI capacitive accelerometer,” *IEEE Journal of Solid-State Circuits*, vol. 39, no. 12, pp. 2467–2476, Dec. 2004.
- [19] Z. Hao, M. F. Zaman, A. Sharma, and F. Ayazi, “Energy loss mechanisms in a bulk-micromachined tuning fork gyroscope,” in *Proc. of 5th IEEE Conference on Sensors, Sensors’06.*, Daegu, Korea, Oct. 2007, pp. 1333–1336.
- [20] S. D. Senturia, *Microsystem Design*. Kluwer Academic Publishers, 2001.
- [21] W. A. Clark, “Micromachined vibratory rate gyroscopes,” Ph.D. dissertation, University of California, Berkeley, May 1997.
- [22] M. W. Putty, “A high aspect-ratio high-performance polysilicon vibrating ring gyroscope,” Ph.D. dissertation, University of Michigan, Dec. 2000.
- [23] C. T. C. Nguyen and R. T. Howe, “An integrated CMOS micromechanical resonator high-q oscillator,” *IEEE Journal of Solid-State Circuits*, vol. 34, no. 4, pp. 440–455, Apr. 1999.
- [24] F. Ayazi and K. Najafi, “High aspect-ratio combined poly and single-crystal silicon (HARPSS)MEMS technology,” *Journal of Microelectromechanical Systems*, vol. 9, no. 3, pp. 288–294, Sept. 2000.
- [25] K. Sundaresan, G. K. Ho, S. Pourkamali, and F. Ayazi, “Electronically temperature compensated silicon bulk acoustic resonator reference oscillators,” in *IEEE Journal of Solid-State Circuits*, vol. 42, no. 6, Lille, France, June 2007, pp. 1425–1434.
- [26] C. T. Nguyen, “Micromechanical signal processors,” Ph.D. dissertation, University of California, Berkeley, May 1994.
- [27] M. A. Lemkin, M. A. Ortiz, N. Wongkomet, B. E. Boser, and J. H. Smith, “A 3-axis surface micromachined sigma-delta accelerometer,” in *Digest of Technical Papers IEEE International Solid-State Circuits Conference, (ISSCC’97)*, San Francisco, CA, USA, Feb. 6–8, 1997, pp. 202–203.

- [28] X. Jiang, J. I. Seeger, M. Kraft, and B. E. Boser, "A monolithic surface micromachined z-axis gyroscope with digital output," in *Digest of Technical Papers Symposium on VLSI Circuits, 2000.*, Honolulu, HI, June 15–17, 2000, pp. 16–19.
- [29] V. P. Petkov and B. E. Boser, "A fourth-order $\sigma\delta$ interface for micromachined inertial sensors," *IEEE Journal of Solid-State Circuits*, vol. 40, no. 8, pp. 1602–1609, Aug. 2005.
- [30] J. Wu, G. K. Fedder, and L. R. Carley, "A low-noise low-offset capacitive sensing amplifier for a $50\mu\text{g}/\sqrt{\text{Hz}}$ monolithic CMOS MEMS accelerometer," *IEEE Journal of Solid-State Circuits*, vol. 39, no. 5, pp. 722–730, May 2004.
- [31] F. Ayazi and K. Najafi, "A HARPSS polysilicon vibrating ring gyroscope," *Journal of Microelectromechanical Systems*, vol. 10, no. 2, pp. 169–179, June 2001.
- [32] P. Gray, R. Meyer, P. Hurst, and S. Lewis, *Analysis and Design of Analog Integrated Circuits*. Wiley, 2001.
- [33] T. B. Gabrielson, "Mechanical-thermal noise in micromachined acoustic and vibrationsensors," *IEEE Transactions on Electron Devices*, vol. 40, no. 5, pp. 903–909, May 1993.
- [34] M. Saukoski, L. Aaltonen, K. Halonen, and T. Salo, "Fully integrated charge sensitive amplifier for readout of micromechanical capacitive sensors," in *Proc. of IEEE International Symposium on Circuits and Systems, (ISCAS'05).*, May 2005, pp. 5377–5380.
- [35] R. R. Harrison and C. Charles, "A low-power low-noise CMOS amplifier for neural recording applications," *IEEE Journal of Solid-State Circuits*, vol. 38, no. 6, pp. 958–965, June 2003.
- [36] J. Graeme, *Photodiode Amplifiers: Op Amp Solutions*. McGraw Hill, 1996.
- [37] R. Pease, "What's all this noise gain stuff anyhow?" in *EDN design article*, Feb. 2004.
- [38] "How to solve five tough signal path challenges by selecting the right op amp," in *National Semiconductor Application Note*, Aug. 2006.
- [39] "HC4046 phase locked loop," in *Phillips Semiconductors Data Sheet*, 2001.
- [40] S. Lee and C. T. C. Nguyen, "Influence of automatic level control on micromechanical resonator oscillator phase noise," *Proceedings of the 2003 IEEE International Frequency Control Symposium and PDA Exhibition Jointly with the 17th European Frequency and Time Forum*, pp. 341–349, May 4–8, 2003.

- [41] W. Geiger, W. U. Butt, A. Gaisser, J. Frech, M. Braxmaier, T. Link, A. Kohne, P. Nommensen, H. Sandmaier, and W. Lang, “Decoupled microgyros and the design principle DAVED,” in *Proc. of IEEE International Conference on Micro Electro Mechanical Systems, (MEMS’01)*., Interlaken, Jan. 2001, pp. 170–173.
- [42] R. Barnaby and A. Reinhardt, “Angular velocity measuring instrument,” U.S. Patent 2 544 646, Mar., 1951.
- [43] R. Barnaby and C. Morrow, “Turn rate measuring instrument,” U.S. Patent 2 753 173, July, 1951.
- [44] A. Sharma, F. M. Zaman, B. V. Amini, and F. Ayazi, “A high-q in-plane SOI tuning fork gyroscope,” in *Sensors, 2004. Proceedings of IEEE*, Oct. 24–27, 2004, pp. 467–470.
- [45] W. C. Tang, M. G. Lim, and R. T. Howe, “Electrostatically balanced comb drive for controlled levitation,” in *Tech. Digest of Solid-State Sensors, Actuators and Microsystems Workshop, 1990.*, Hilton Head Island, SC, USA, June 4–7, 1990, pp. 23–27.
- [46] M. Zaman, A. Sharma, B. V. Amini, and F. Ayazi, “Towards inertial grade vibratory microgyros: A high-q in-plane silicon-on-insulator tuning fork device,” in *Tech. Digest of Solid-State Sensors, Actuators and Microsystems Workshop, 2004.*, Hilton Head Island, SC, USA, June 4–7 2004, pp. 384–385.
- [47] D. J. Kim and R. T. M’Closkey, “A systematic method for tuning the dynamics of electrostatically actuated vibratory gyros,” *IEEE Transactions on Control Systems Technology*, vol. 14, no. 1, pp. 69–81, Jan. 2006.
- [48] W. T. Sung, J. Y. Lee, J. G. Lee, and T. Kang, “Design and fabrication of an automatic mode controlled vibratory gyroscope,” in *Proc. of IEEE International Conference on Micro Electro Mechanical Systems, (MEMS’06)*, Istanbul, Turkey, 2006, pp. 674–677.
- [49] M. F. Zaman, A. Sharma, and F. Ayazi, “High performance matched-mode tuning fork gyroscope,” in *Proc. of IEEE International Conference on Micro Electro Mechanical Systems, (MEMS’06)*., Istanbul, Turkey, 2006, pp. 66–69.
- [50] Thomae and Lutz, “Method and device of tuning a second oscillator with the first oscillator and rotation rate sensor,” U.S. Patent 6 654 424, Nov., 2003.
- [51] T. K. Tang, R. C. Gutierrez, C. B. Stell, V. Vorperian, G. A. Arakaki, J. T. Rice, W. J. Li, I. Chakraborty, K. Shcheglov, J. Z. Wilcox, and W. J. Kaiser, “A packaged silicon MEMS vibratory gyroscope for microspacecraft,” in *Proc. of IEEE International Conference on Micro Electro Mechanical Systems, (MEMS’97)*., Nagoya, Japan, Jan. 26–30, 1997, pp. 500–505.

- [52] K. Sundaresan, G. K. Ho, S. Pourkamali, and F. Ayazi, "A two-chip, 4-MHz, microelectromechanical reference oscillator," in *proc. of IEEE International Symposium on Circuits and Systems (ISCAS'05)*, May 23–26, 2005, pp. 5461–5464.
- [53] A. Sharma, M. F. Zaman, and F. Ayazi, "A 104db SNDR transimpedance-based CMOS ASIC for tuning fork microgyroscopes," in *Proc. of IEEE Custom Integrated Circuits Conference (CICC'06)*, San Jose, CA, Sept.10–13 2006, pp. 655–658.
- [54] P. K. D. Pai and A. A. Abidi, "A 40-mw 55 mb/s CMOS equalizer for use in magnetic storage read channels," *IEEE Journal of Solid-State Circuits*, vol. 29, no. 4, pp. 489–499, Apr. 1994.
- [55] M. S. J. Steyaert, W. Dehaene, J. Craninckx, M. Walsh, and P. Real, "A CMOS rectifier-integrator for amplitude detection in hard disk servo loops," in *IEEE Journal of Solid-State Circuits*, vol. 30, no. 7, July 1995, pp. 743–751.
- [56] S. M. Zhak, M. W. Baker, and R. Sarpeshkar, "A low-power wide dynamic range envelope detector," *IEEE Journal of Solid-State Circuits*, vol. 38, no. 10, pp. 1750–1753, Oct. 2003.
- [57] M. Mano, *Digital Design*. Prentice Hall, 1998.
- [58] J. Bastos, A. M. Marques, M. S. J. Steyaert, and W. Sansen, "A 12-bit intrinsic accuracy high-speed CMOS DAC," *IEEE Journal of Solid-State Circuits*, vol. 33, no. 12, pp. 1959–1969, Dec. 1998.
- [59] T. Miki, Y. Nakamura, M. Nakaya, S. Asai, Y. Akasaka, and Y. Horiba, "An 80-MHz 8-bit CMOS d/a converter," *IEEE Journal of Solid-State Circuits*, vol. 21, no. 6, pp. 983–988, Dec. 1986.
- [60] R. Curey, M. Ash, L. Thielman, and C. Barker, "Proposed IEEE inertial systems terminology standard and other inertial sensor standards," in *IEEE Position Location and Navigation Symposium, (PLANS'04)*, 2004, pp. 83–90.
- [61] "IEEE standard specification format guide and test procedure for single-axis laser gyros," IEEE, Sept. 1995.
- [62] S. Kay, *Handbook of Virtual Environment Technology*. Lawrence Erlbaum Associates, 2002.
- [63] A. Sharma, "Predictive methodologies for substrate parasitic extraction and modeling in heavily doped CMOS substrates," Master's thesis, Oregon State University, Corvallis, Aug. 2003.
- [64] S. A, Z. M. F, and A. F, "A 104db dynamic range transimpedance-based CMOS ASIC for tuning fork microgyroscopes," *IEEE Journal of Solid-State Circuits*, vol. 42, no. 8, pp. 1790–1802, Aug. 2007.

- [65] A. Sharma, M. Faisal Zaman, and F. Ayazi, "A 0.2deg/hr micro-gyroscope with automatic CMOS mode matching," in *Digest of Technical Papers IEEE International Solid-State Circuits Conference, (ISSCC'07)*, San Francisco, CA, Feb. 11–15, 2007, pp. 386–610.
- [66] "OPA656 JFET amp data sheet," in *Texas Instruments Data Sheet*, 2000.
- [67] (1998). [Online]. Available: <http://www.siliconsensing.com/gyros>
- [68] H. Rodjegard, D. Sandstrom, P. Pelin, N. Hedenstierna, D. Eckerbert, and G. I. Andersson, "A digitally controlled MEMS gyroscope with 3.2deg/hr stability," in *Tech. Digest of International Conference on Solid State Sensors and Actuators, (TRANSDUCERS'05)*, vol. 2, Seoul, Korea, June5–9, 2005, pp. 535–538.
- [69] R. Neul, U.-M. Gmez, K. Kehr, W. Bauer, J. Classen, C. Dring, E. Esch, S. Gtz, J. Hauer, B. Kuhlmann, C. Lang, M. Veith, and R. Willig, "Micromachined angular rate sensors for automotive applications," *IEEE Sensors Journal*, vol. 7, no. 2, pp. 302–309, Feb. 2007.
- [70] E. S., B. S., D. R., B. J., and D. Allen, "Reduced minimum configuration fiber optic gyro for land navigation applications," in *IEEE Position Location and Navigation Symposium, (PLANS'96)*, 1996, pp. 38–41.
- [71] B. V. Amini, R. Abdolvand, and F. Ayazi, "A 4.5-mw closed-loop sigma-delta micro-gravity CMOS SOI accelerometer," *IEEE Journal of Solid-State Circuits*, vol. 41, no. 12, pp. 2983–2991, Dec. 2006.
- [72] B. Brandt and B. Wooley, "A 50-mhz multibit sigmadelta modulator for 12-b 2-mhz a/d conversion," *IEEE Journal of Solid-State Circuits*, vol. 26, no. 12, pp. 1746–1756, Dec. 1991.
- [73] B. E. Boser and R. T. Howe, "Surface micromachined accelerometers," in *IEEE Journal of Solid-State Circuits*, vol. 31, no. 3, Mar. 1996, pp. 366–375.
- [74] T. Smith, O. Nys, M. Chevroulet, Y. DeCoulon, and M. Degrauwe, "A 15 b electromechanical sigma-delta converter for acceleration measurements," in *Digest of Technical Papers IEEE International Solid-State Circuits Conference, (ISSCC 1994)*, San Francisco, CA, USA, Feb. 16–18, 1994, pp. 160–161.
- [75] C. Lu, M. Lemkin, and B. E. Boser, "A monolithic surface micromachined accelerometer with digital output," *IEEE Journal of Solid-State Circuits*, vol. 30, no. 12, pp. 1367–1373, Dec. 1995.
- [76] C. T. C. Nguyen, "Micromechanical resonators for oscillators and filters," in *Proc. of IEEE Ultrasonics Symposium, 1995.*, vol. 1, Seattle, WA, USA, Nov. 7–10, 1995, pp. 489–499.

- [77] J. T. Kung, H. S. Lee, and R. T. Howe, "A digital readout technique for capacitive sensor applications," *IEEE Journal of Solid-State Circuits*, vol. 23, no. 4, pp. 972–977, Aug. 1988.
- [78] M. Lutz, W. Golderer, J. Gerstenmeier, J. Marek, B. Maihofer, S. Mahler, H. Munzel, and U. Bischof, "A precision yaw rate sensor in silicon micromachining," in *Tech. Digest of International Conference on Solid State Sensors and Actuators, (TRANSDUCERS'97)*, vol. 2, Chicago, IL, USA, June 16–19, 1997, pp. 847–850.
- [79] R. Voss, K. Bauer, W. Ficker, T. Gleissner, W. Kupke, M. Rose, S. Sassen, J. Schalk, H. Seidel, and E. Stenzel, "Silicon angular rate sensor for automotive applications with piezoelectric drive and piezoresistive read-out," in *Tech. Digest of International Conference on Solid State Sensors and Actuators, (TRANSDUCERS'97)*, vol. 2, Chicago, IL, USA, June 16–19, 1997, pp. 879–882.
- [80] P. Greiff, B. Boxenhorn, T. King, and L. Niles, "Silicon monolithic micromechanical gyroscope," in *Tech. Digest of International Conference on Solid State Sensors and Actuators, (TRANSDUCERS'91)*, San Francisco, CA, USA, June 24–27, 1991, pp. 966–968.
- [81] Y. B. Gianchandani and K. Najafi, "A bulk silicon dissolved wafer process for microelectromechanical devices," *Journal of Microelectromechanical Systems*, vol. 1, no. 2, pp. 77–85, June 1992.
- [82] F. Paoletti, M. A. Gretillat, and N. F. de Rooij, "A silicon micromachined vibrating gyroscope with piezoresistive detection and electromagnetic excitation," in *Proc. of IEEE International Conference on Micro Electro Mechanical Systems, (MEMS'96)*, San Diego, CA, USA, Feb. 11–15, 1996, pp. 162–167.
- [83] H. Kuisma, T. Ryhanen, J. Lahdenpera, E. Punkka, S. Ruotsalainen, T. Sillanpaa, and H. Seppa, "A bulk micromachined silicon angular rate sensor," in *Tech. Digest of International Conference on Solid State Sensors and Actuators, (TRANSDUCERS'97)*, vol. 2, Chicago, IL, USA, June 16–19, 1997, pp. 875–878.
- [84] Y. Oh, B. Lee, S. Baek, H. Kim, J. Kim, S. Kang, and C. Song, "A surface-micromachined tunable vibratory gyroscope," in *Proc. of IEEE International Conference on Micro Electro Mechanical Systems, (MEMS'97)*, Nagoya, Japan, Jan. 26–30, 1997, pp. 272–277.
- [85] K. Y. Park, C. W. Lee, Y. S. Oh, and Y. H. Cho, "Laterally oscillated and force-balanced micro vibratory rate gyroscope supported by fish hook shape springs," in *Proc. of IEEE International Conference on Micro Electro Mechanical Systems, (MEMS'97)*, Nagoya, Japan, Jan. 26–30, 1997, pp. 494–499.

- [86] S. An, Y. S. Oh, B. L. Lee, K. Y. Park, S. J. Kang, S. O. Choi, Y. I. Go, and C. M. Song, "Dual-axis microgyroscope with closed-loop detection," in *Proc. of IEEE International Conference on Micro Electro Mechanical Systems, (MEMS'98)*., Heidelberg, Germany, Jan. 25–29, 1998, pp. 328–333.
- [87] T. Juneau, A. P. Pisano, and J. H. Smith, "Dual axis operation of a micromachined rate gyroscope," in *Tech. Digest of International Conference on Solid State Sensors and Actuators, (TRANSDUCERS'97)*, vol. 2, Chicago, IL, USA, June 16–19, 1997, pp. 883–886.
- [88] T. Fujita, T. Mizuno, R. Kenny, K. Maenaka, and M. Maeda, "Two-dimensional micromachined gyroscope," in *Tech. Digest of International Conference on Solid State Sensors and Actuators, (TRANSDUCERS'97)*, vol. 2, Chicago, IL, USA, June 16–19, 1997, pp. 887–890.
- [89] W. Geiger, B. Folkmer, J. Merz, H. Sandmaier, and W. Lang, "A new silicon rate gyroscope," in *Proc. of IEEE International Conference on Micro Electro Mechanical Systems, (MEMS'98)*., Heidelberg, Germany, Jan. 25–29, 1998, pp. 615–620.
- [90] D. R. Sparks, S. R. Zarabadi, J. D. Johnson, Q. Jiang, M. Chia, O. Larsen, W. Higdon, and P. Castillo-Borelley, "A CMOS integrated surface micromachined angular rate sensor: its automotive applications," in *Tech. Digest of International Conference on Solid State Sensors and Actuators, (TRANSDUCERS'97)*, vol. 2, Chicago, IL, USA, June 16–19, 1997, pp. 851–854.
- [91] C. Shearwood, C. B. Williams, P. H. Mellor, R. B. Yates, M. R. J. Gibbs, and A. D. Mattingley, "Levitation of a micromachined rotor for application in a rotating gyroscope," *Electronics Letters*, vol. 31, no. 21, pp. 1845–1846, Oct. 1995.
- [92] J. Soderkvist, "Piezoelectric beams and vibrating angular rate sensors," *IEEE Transactions on Ultrasonics, Ferroelectrics and Frequency Control*, vol. 38, no. 3, pp. 271–280, May 1991.
- [93] B. E. Boser, "Electronics for micromachined inertial sensors," in *Tech. Digest of International Conference on Solid State Sensors and Actuators, (TRANSDUCERS'97)*, vol. 2, Chicago, IL, USA, June 1997, pp. 1169–1172.
- [94] S. R. Zarabadi, P. E. Castillo-Borelley, and J. D. Johnson, "An angular rate sensor interface IC," in *Proc. of the IEEE Custom Integrated Circuits Conference (CICC'96)*, San Diego, CA, USA, May 1996, pp. 311–314.
- [95] C. Song, "Commercial vision of silicon based inertial sensors," in *Tech. Digest of International Conference on Solid State Sensors and Actuators, (TRANSDUCERS'97)*, vol. 2, Chicago, IL, USA, June 1997, pp. 839–842.

- [96] S. R. Norsworthy, R. Schreier, and G. C. Temes, *Delta-Sigma Data Converters: Theory, Design, and Simulation*. Piscataway, NJ: IEEE Press, 1992.
- [97] C. C. Enz and G. C. Temes, "Circuit techniques for reducing the effects of op-amp imperfections: autozeroing, correlated double sampling, and chopper stabilization," *Proceedings of the IEEE*, vol. 84, no. 11, pp. 1584–1614, Nov. 1996.
- [98] L. Bjorset, "Apparatus and method for estimating angular rate," U.S. Patent 2002/0 123 857, Nov., 2003.
- [99] Chia and Zarabadi, "Sensor bias drift compensation," U.S. Patent 6 486 661, Nov., 2002.
- [100] F. Ayazi and K. Najafi, "Design and fabrication of high-performance polysilicon vibrating ring gyroscope," in *Proc. of IEEE International Conference on Micro Electro Mechanical Systems, (MEMS'98)*., Heidelberg, Germany, Jan. 25–29, 1998, pp. 621–626.